THE UNIVERSITY OF CHICAGO

REACTIVE MOLECULAR DYNAMICS STUDY OF PROTON TRANSPORT IN AQUEOUS SYSTEMS

A DISSERTATION SUBMITTED TO
THE FACULTY OF THE DIVISION OF THE PHYSICAL SCIENCES
IN CANDIDACY FOR THE DEGREE OF
DOCTOR OF PHILOSOPHY

DEPARTMENT OF CHEMISTRY

BY
PAUL BRADLEY CALIO

CHICAGO, ILLINOIS
DECMBER 2020

For those who have been by my side.

Table of Contents

List of Figures

List of Tables

Acknowledgements

I first want to thank Prof. Greg Voth for being my Ph.D. advisor. His mentorship, patience, understanding of research and the scientific field, and his scientific knowledge has proven invaluable and beneficial during my Ph.D. This work would not be what it is without his advising, and I am very grateful for that. I would also like to thank Prof. Suri Vaikuntanathan and Prof. Andrei Tokmakoff for serving on my thesis committee. Additionally, I want to thank my undergraduate advisor Prof. Edward Remsen for exposing me to my first research project and Prof. Ward Thompson for first exposing me to computational and theoretical chemistry via an REU experience.

I next want to thank those I have worked with and/or had engaging research conversations. Chris Arntsen and Chen Chen were very influential in the early years of my Ph.D. and taught me about MD simulations and coding. I am pleased to work with them on the proton hopping analysis project. Glen Hocky and Thomas Dannenhoffer-Lafage exposed me to the experiment directed simulations (EDS) method and were very helpful on getting the project off the ground. Chenghan Li greatly assisted on the spectroscopy work and further applied my EDS bias to the hydrated excess proton. Scientific discussions with him were very beneficial for me in my Ph.D. I also need to thank Memo Carpenter for directing me to his and the Tokmakoff group's work on the hydrated proton, and for the discussions regarding the hydrated excess proton.

I also want to thank members of the Voth group who have made coming into work especially great and who became friends outside of lab. Specifically, Laura Watkins, Zack Jarin, Rui Sun, Alek Durumeric, and Yining Han. Your friendship has made graduate school more enjoyable. I'd also like to specially recognize Laura Watkins. You have been a loyal friend inside and outside of lab, which I am extremely grateful.

My life in graduate school has been enriched from the numerous relationships outside of my lab, and with people who have also helped me during the difficulties of graduate school and personal life. I would like to thank Whitney Fowler; Luci and Alex Parrish; Vaughn Spurrier; Laura Watkins; Robert, Diane, Jude, Isaac, and Ellie Marineau; Drew Donaldson; Jeremy White; Andrew and Rebekah Todd; and Munia Mustafa. Additionally, I would like to thank my roommates who have been patient with me during graduate school: Andrew Zulker, Chris Schneider, Jeff Gustafson, LJ Shelven, Alex Parrish, Viktor Rozsa, Zack Jarin, and Grant Hill.

Lastly, I want to thank my family for encouraging me during my studies and being with me on the long road of education: John, Julie, Joe, Zoë, Matthew, and Brenda Calio. Additionally, I want to thank my cousins who have checked in with me, visited me, and let me come and visit them: Jessey, Jeff, Oren Bradley (Obi), and Guinevere Eagan, and Nikki and Kent Wagenschutz.

Abstract

Reactive molecular dynamics simulations are performed to study proton transport in various aqueous systems. Methods such as ab initio molecular dynamics (AIMD) simulations, experiment directed simulations of AIMD (EDS-AIMD), and the multistate empirical valence bond (MS-EVB) methods are used to capture both normal diffusion and the bond rearrangement of the Grotthus mechanism. Work is presented that focuses on correlating information from MD simulation to recent nonlinear spectroscopy experiments, investigates the influence of external electric fields on proton transport in the Nafion proton exchange membrane, improves AIMD water simulations by using EDS, and investigates the proton hopping mechanism is AIMD simulations. EDS-AIMD and MS-EVB simulations provide reorientation time constants that correspond to the special-pair dance – a process where the special-pair changes in the distorted Eigen cation – in addition to irreversible proton transport. The time constant of irreversible proton transport are further analyzed as a function of concentration and temperature to provide molecular support to recent experiments which showed that counter ions create entropic barriers to proton transport. The self-consistent iterative MS-EVB method show that external electric fields enhance the dynamical properties of proton in the Nafion membrane, while showing that protons transport via the potential energy well around sulfonate groups – as shown by previous reactive simulations. The EDS method was used to bias the hydrogen bond in AIMD water simulations that produced structural and dynamical properties close to the accurate MB-pol. Lastly, the proton hopping mechanism in AIMD simulations were reanalyzed that showed single hops are the dominate hopping mechanism, which is in contrast to recent AIMD studies that showed that double hops dominate. Taken together, these studies show how various reactive molecular dynamics simulation methods can investigate proton transport in aqueous systems.

Chapter 1: Introduction

I. Motivation

Many general chemistry textbooks will have a chapter or two dedicated to acid-base chemistry, and therein the authors help the reader learn topics and solve problems of strong and weak acid-base compounds. A very well-known strong acid used is hydrochloric acid (HCl). When gaseous HCl is dissolved in water, it will produce a solvated proton, H_3O^+, and chloride ion (Eq. 1.1).

$$\mathrm{HCl}_{(g)} \xrightarrow{H_2O} \mathrm{H^+}_{(aq)} + \mathrm{Cl^-}_{(aq)} \tag{1.1}$$

When introducing this dissociation equation, it is commonly stated that $\mathrm{H^+}_{(aq)}$ and $\mathrm{H_3O^+}_{(aq)}$ are equivalent notations for the solvated proton, which is also called the hydrated excess proton.[1-2] Contrary to this understanding, the hydrated excess proton has structural and dynamical properties unlike other alkali metal cations, which makes considering the hydrated excess proton as a hydronium cation very difficult. For example, the diffusion coefficient of the hydrated excess proton is 0.94 Å^2/ps, which is 4-5 times larger than other monovalent cations.[3-4] Detailing his curious behavior is further complicated when trying to understand it in light of its solvation structure, as will be discussed in the following paragraphs.

A key motivator to understanding the essential nature of the hydrated proton is due to the various applications of the hydrated proton in systems such as alternative energy materials,[5-7] enzymatic reactions,[8] and transmembrane proteins.[3, 9-11] For example, a relevant system for understanding proton transport is proton exchange membrane fuel cells, as it has been a proven source of alternative energy. In these fuel cells, hydrogen gas is oxidized to produce protons that transport through a porous membrane to reach the cathode to be reduced into water. The polymer membrane Nafion[12] has been the benchmark membrane in these fuels cells for many years due to its high proton conductivity and stability. In hydrated Nafion, the hydrophobic carbon backbone and hydrophilic pore creates a phase segregation and a tortuous water channel for the proton to transport through.[12-13] Further understanding proton transport in these membranes can be very influential in the design of membranes for future applications in these fuel cells.

II. Hydrated Excess Proton Background

Understanding the structure and dynamics of the hydrated excess proton has been an area of active research for the past 200 years. In 1806, von Grotthus proposed that the proton's comparably large diffusion coefficient arose from the proton hopping to water molecules.[14-15] In this Grotthus mechanism, one of the O-H covalent bonds of the central hydronium species switches with the hydrogen bond of a neighboring water molecule forming a new hydronium center. Once the proton hops to the accepting water molecule, the identity of the excess proton could change with other hydrogen atoms in the hydronium core as a different hydrogen might be the proton that hops to the next water molecule in the hopping chain. Therefore, in this mechanism, the coupling of both nuclear and electronic degrees of freedom enables Grotthuss hopping and normal vehicular transport to contribute to the overall diffusion process. This mechanism becomes further complicated when the hydrated excess proton is no longer considered a single particle that hops from one water molecule to another, but rather as a charge defect in water that delocalizes across multiple water molecules.[16]

This degree of delocalization across water molecules has led to understanding the Grotthuss mechanism in terms of solvation structures proposed by Eigen[17] and Zundel.[18] In the Eigen picture, the excess proton prefers to associate with one water molecule forming a hydronium core, and whose charge delocalizes across the three neighboring water molecules creating three, equivalently strong hydrogen bonds in the 1st solvation shell. In the Zundel picture, the excess proton is equally delocalized among two flanking waters forming a $H_5O_2^+$ structure with the proton equidistance from the two waters. In liquid phase, fluctuations of the solvent introduce distortions to these symmetric solvation structure that makes it difficult to characterize the hydrated excess proton as purely Eigen or Zundel, making these two solvation structures only limiting structures of the hydrated excess proton. Instead terms like "distorted Eigen"[19-20] and "distorted (or asymmetric) Zundel"[21-23] are used to describe the hydrated excess proton, and are most likely different terms that mean the same thing.

Molecular dynamics simulations are well posed to provide molecular details of proton transport and solvation. For molecular simulations to provide theoretical support and predictions regarding the structure and dynamics of the hydrated excess proton, the simulation method must inherently account for the charge delocalization that enables the Grotthus mechanism. A natural method to understand proton transport is *ab initio* molecular dynamics simulations (AIMD),[24] which uses electronic structure methods to explicitly account for the electronic degrees of freedom by typically using density functional theory (DFT) with generalized gradient approximations (GGA)[25-27] for the exchange-correlation functional. By directly incorporating the electronic degrees of freedom, AIMD simulations are limited in the length and timescales of their simulations, and that is without considering the accuracy of GGA functionals to model the electron density. For example, the intimate role of water molecules in the proton transport and solvation necessitates an accurate model for water, but GGA functionals suffer from over-polarization[28-29] and partial covalency (also known as charge transfer) between water molecules.[30-32] These inaccuracies of GGA functionals results in overstructuring of water molecules at room temperature and diffusion coefficients that can be an order of magnitude smaller than experiments.[33-35] The

AIMD community use methods to remedy these failures either by increasing the simulation temperature or implementing a higher DFT level of theory.[36-39] The former remedy no longer simulates the proper thermodynamic ensemble of ambient conditions, while the latter remedy increases the computational cost of already expensive DFT simulations.

As AIMD simulation are a resourceful tool to model the hydrated excess proton, it's imperative to have an AIMD method that accurately describes the physics of the hydrated excess proton at the proper thermodynamic ensemble. One method that has been used to improve AIMD simulations is the Experiment Directed Simulation (EDS) method.[40-43] Work from Pitera and Chodera showed that a linear bias exists on observables that minimizes the relative entropy between the biased molecular simulation and a target experimental ensemble.[44] EDS is a method developed by White and Voth that parameterizes these linear terms in the system's Hamiltonian,[41] and has been used to bias the solvation structure of BLYP and BLYP-D3 water to match the experimental O-O radial distribution function.[43] This EDS-AIMD method was able to improve the solvation structure of AIMD simulations and other unbiased structural and dynamical properties without increasing the simulation temperature or computational cost. This EDS-AIMD method was further used to study the excess proton, and it improved the ratio of the hydrated excess proton to water diffusion coefficient, while not disrupting other physical properties.

An alternative method to simulate the hydrated excess proton is the multistate empirical valence bond method (MS-EVB).[45-49] The MS-EVB method has actively been developed in the Voth group for the past 20+ years, and has been known to be both accurate and efficient at modeling the hydrated excess proton. In the MS-EVB formalism, the system is described by creating a linear combination of different bonding topologies that have different water molecules being covalently bonded to the hydrated excess proton. A quantum-like Hamiltonian is then constructed using classical force-field equations for the diagonal elements and off-diagonal elements to enable proton transport. After diagonalization, the ground-state energy is then used to prorogate the system in time. The MS-EVB method has also been extended to model concentrated acid solutions by solving for the total ground state energy self-constantly in the self-consistent iterative MS-EVB (SCI-MS-EVB) method.[50]

These reactive molecular dynamics simulation methods have been used to understand the hydrated excess proton's structure and dynamics and have emphasized the role of water molecules in proton transport. Earlier simulation studies by Tuckerman et al.[51-52] used AIMD simulations of a proton in 32 waters to confirm (1) the proton prefers to reside on one water molecule 60% of the time, and (2) that one water molecule is observed closer to the hydronium core than the other 2 water molecules in the 3-coordinated solvation shell. This close water molecule was termed the special pair and is very characteristic of the two-water picture of a Zundel cation. Further molecular dynamics (MD) studies[20] have supported this idea of a single water molecule residing closer to the hydronium, and additionally found that this special-pair oscillates with the other water molecules in the 1st solvation shell. This rotation of special-pairs was called the special-pair dance and occurs on the femtosecond timescale. Additionally, it has been shown that irreversible proton transport requires the breaking of water hydrogen bonds in the second solvation shell and is on the order of 1-2 ps.[15, 19, 51-52] In this mechanism, it was further proposed that a distorted Eigen best characterizes the solvation structre of the hydrated excess proton as it incapsulates both the Zundel-like configurations of the special-pair in addition to the special-pair dance. Describing the solvation shell primarily as an Eigen cation has caused the dominant proton transports mechanism to be described as an Eigen-Zundel-Eigen mechanism, where the distorted Eigen cation is the most stable structure and the Zundel cation is only an intermediate complex.[15, 19-20, 53-55]

Experiments have also supported that proton transport occurs on the picosecond timescale. The standard experimental benchmark is a 1961 nuclear magnetic resonance study of O^{17} that showed the timescale of proton transport is about 1.5 ps.[56] This can also be interpreted as the lifetime of the most stable structure. In recent years, two dimensional infrared (2D IR) spectroscopy has proposed from anisotropy decays of flanking water bends in a Zundel-like complex that the timescale for irreversible proton transport is about 2.5 ps,[57] which is comparable to the 1-2 ps timescales in simulations and experiments.

In addition to the 2.5 ps timescale of irreversible proton transport, 2D IR experiments have also provided information about the solvation structure and thermodynamics of the hydrated excess proton.[21, 57-61] 2D IR studies acetonitrile-acid mixtures observed the proton transfer mode (PTM) of the excess proton between two waters had a $|1\rangle \rightarrow |2\rangle$ transition that was greater than the $|0\rangle \rightarrow |1\rangle$ transition.[60-61] This was used to suggest that the proton resides in a symmetric double-welled, potential energy surface (PES), and that the solvation structure of the hydrated excess proton is best described as a symmetric Zundel cation.[60-61] In acid solutions,[58] the water O-H stretching vibrations were excited and correlations with flanking water bends in the Zundel-like complex were observed. This finding was used to propose that Zundel-like configurations play a larger role in describing the hydrated excess proton.[58] Further studies using 2D IR[21] in acid solutions also observed the PTM $|1\rangle \rightarrow |2\rangle$ transition was greater than the $|0\rangle \rightarrow |1\rangle$ transition, while also proposing a distortion in the underlying PES. This suggests that an asymmetric (or distorted) Zundel-like cation characterizes the solvation structure of the hydrated excess proton.

Further anisotropy studies of the flanking water bend were conducted to investigate the effects of temperature and concentration.[59] It was found that the reorientation time constants increased with counterion concentration and were independent of the proton concentration. Arrhenius plots of the reorientation time constants showed that the activation energy decreased with increasing counterion concentration, which appeared contrary to the increased trend in reorientation time constants. These findings were then explained via an Eyring-like equation from transition state theory to propose that counter ions create entropic barriers to proton transport.

The complex nature of proton transport has led AIMD simulations of the hydrated excess proton to propose other hopping mechanisms for the hydrated excess proton than the mechanisms already discussed. AIMD simulations of Hassanali *et. al.*[62] showed the abundance of water wires that facilitate proton transport. In this mechanism, it was observed that the proton transport experiences periods of rest and burst behavior. In the rest period, the proton is found to have minimal displacement, while the burst behavior is shown to have large displacement in short periods of time by hopping along multiple water molecules. Proton transport in these burst behaviors lead to the conclusion that concerted hopping via compressed water wires was a dominate hopping mechanism for the excess proton. The rest and burst behavior were further verified by Tse *et. al.*,[33] while also showing that concerted hopping could occur during rest behaviors, mitigating its role in the large proton diffusion. This work by Tse *et. al.* also proposed that proton transport is further facilitated by the hydrogen atom of a fourth water molecule being located in the lone-pair region of the hydronium oxygen atom. This fourth water was termed a pre-solvating water molecule and it was shown to enhance proton transport by increasing the compression of the solvating waters. In recent years, the dominance of concerting hopping was revisited by Wu and co-workers, which showed that double hopping events are four times more probably than single hopping events.[63] The prominence of double hops where then used to explain large proton diffusion in acidic solutions.

In addition to proton transport in water, molecular simulations have also investigated the proton transport mechanism in PFSA membranes. Hydrated PFSA membranes have a tortuous water channel that contains the sulfonate groups from the side chains, and it's been shown from reactive MS-EVB simulations that these sulfonate groups play an intimate role in shuttling protons through the hydrophilic pore.[6-7] These simulations found that excess protons are within two solvation shells of a sulfonate group. Even when a repulsive interaction was used to weaken the sulfur-proton association, the excess proton's dynamics were negligibly affected as the proton was never in bulk-like water. It was concluded from this finding that protons transport along the sulfonate groups due to the overlap of each group's potential energy well.

II. Thesis Summary

The work presented in this thesis continues to use reactive MD methods to understand proton transport in aqueous systems. The progression of the following chapters will be based on the simulation methods, where the early chapters will include work that used existing simulation methods to understand proton transport, and the later chapters used simulations methods that were developed during my Ph.D. The study in Chapter 2 uses EDS-AIMD and MS-EVB methods to understand proton transport in light of recent 2D IR experiments. Specifically, this chapter focus on the 2.5 ps anisotropy decay in experiments and work to correlate anisotropy timescales to molecular reorientations, while examining time-evolution of normal modes. It is argued in Chapter 2 that the dynamics of the hydrated excess proton are important in characterizing the proton solvation. Additionally, in Chapter 3, the SCI-MS-EVB method is used to understand the effects of temperature and concentration on these reorientation timescales to provide molecular origins to experimental findings. These results provide agreement with 2D IR experiments which show that the 2.5 ps anisotropy decay corresponds to irreversible proton transport and that chloride ions create entropic barriers to proton transport. The SCI-MS-EVB method is further applied in Chapter 4 to understand proton transport in hydrated Nafion membranes under external voltages. It has been shown that electrolytes in ultrathin electrochemical cells can have enhanced dynamical properties known as coulomb transport that results from electric fields to the system. By applying various electric fields to hydrated Nafion, we show that the proton transport mechanism previously found in PFSA membranes is still present while enhancing the dynamical effects of the excess proton.

Following this, Chapter 5 provides work that used EDS to bias the hydrogen bond in AIMD water to reproduce the O-H RDF of the highly accurate MB-pol water model. This method, which will be known as EDS-AIMD(OH) to distinguish it from the previous EDS-AIMD(OO) method, is shown to improve BLYP and BLYP-D3 AIMD water while showing improved structural and dynamical properties that were unbiased, and is found to have better properties than our previous EDS-AIMD(OO) method. This will be followed by further examining the proton hopping behavior in AIMD simulations to understand if multiple hops do occur in Chapter 6. This study will examine the effect of various simulation methods, including the EDS-AIMD(OH) method for the hydrated excess proton, in addition to effects resulting from higher simulation temperatures. The findings from this study will show that single hops are the dominate proton hopping mechanism, which agrees with the Eigen-Zundel-Eigen mechanism. Concluding remarks will then be present in Chapter 7.

Chapter 2: On the Essential Nature of the Hydrated Excess Proton and Interpretation of Recent Spectroscopic Experiments

Abstract

Recent two-dimensional infrared spectroscopy experiments have presented results regarding the dynamics of the hydrated excess proton (aka “hydronium” cation solvated in water). It has been suggested by these experiments that the hydrated excess proton has an anisotropy reorientation timescale of 2.5 ps, which might be viewed as being somewhat long lived in comparison to some previous theoretical and computational predictions. However, through the use of both the reactive molecular dynamics Multistate-Empirical Valence Bond and Experiment Directed Simulation *Ab Initio* Molecular Dynamics methods we show that timescales of the same magnitude are obtained that correspond to proton transport, while also capturing structural reorientations of the hydrated proton structure that correspond to the “special pair dance” – a process predicted by prior computational studies in which the central hydrated hydronium in a distorted Eigen cation ($H_9O_4^+$) structure continually switches special pair partners with strongly hydrogen-bonded neighboring water molecules. We further examine these dynamics through the time-evolution of instantaneous normal modes. We show that the excess proton has a spectral signature unique from the other protons in the hydrated proton complex, but that the species is dynamical and switches its identity. We conclude, therefore, that the δ parameter can characterize the excess proton, while at the same time emphasizing that selecting static structures from MD simulations and determining spectroscopic information should be considered in reference to its dynamics.

I. Introduction

The hydrated excess proton (aka "hydronium cation" plus nearby solvating water molecules) is pervasive in systems relevant to complex problems, e.g., proteins[3, 9-11] and renewable energy materials.[5-7] Characterizing its essential solvation and transport behavior has been an active research area for two centuries. In bulk water, the hydrated excess proton has an anomalously high diffusion coefficient in comparison to other +1 cations,[64] which is typically described via the Grotthuss mechanism,[15, 65] where the proton translocates over large distances through the breaking and forming of covalent bonding. In contrast, the solvation structure of hydrated excess proton is usually described by either a Zundel[18] cation (an excess proton equally solvated by two flanking water molecules) or an Eigen[17] cation (a hydronium ion (H_3O^+) core with strong hydrogen bonds to its three surrounding water molecules). However, the exact nature of the hydrated excess proton hopping mechanism and most stable solvation structure represent areas of ongoing research interest.

The solvation and transport properties of hydrated excess proton are well represented in theoretical studies.[15, 46, 52, 54, 66-68] The dominant proton transports mechanism is an Eigen-Zundel-Eigen mechanism, where the Eigen cation is the most stable structure and the Zundel cation is only an intermediate complex.[15, 19-20, 53-55] In this vein, proton transport occurs through the cleavage of a hydrogen bond in the second solvation shell, confirming that Grotthuss hopping occurs via a step-wise process.[15, 19, 51-52] Although the EZE proton hopping mechanism represents the predominant mechanism, the literature does include reports of Zundel-Zundel conversions.[52, 69-71]

In actuality, however, the solvation structure of the hydrated excess proton is more complex than either symmetric Eigen or Zundel cations. In fact, the hydrated excess proton is seen in a broad range of configurations, making Eigen or Zundel cations only limiting structures and very difficult to deconvolute. Tuckerman et al.[51-52] utilized *ab initio* molecular dynamics (AIMD) simulations of a proton in 32 waters to confirm the presence of a special pair between the hydronium and nearby water molecules, which is very characteristic of a Zundel cation. Later molecular dynamics (MD) studies characterized the structure of the solvated proton as a distorted Eigen cation, where the three-fold symmetry is broken due to the distortion of the special pair.[20] In particular, classical multistate empirical valence bond (MS-EVB) and AIMD simulations were used to confirm that the identity of the special pair is not static, but instead switches with the other water molecules in the Eigen cation about once every 40 fs.

Elucidating the solvation structure of the hydrated excess proton is further complicated by the difficulty of correlating experimental infrared frequencies with structural information obtained from MD simulations. Although gas-phase results have been very informative in correlating the two,[72-75] the condensed phase introduces further complications due to thermal and quantum fluctuations.[46, 76] When compared to the pure water absorption spectrum, four notable features can be seen in the acidic IR spectrum: (1) a red shift in the O-H peak of bulk water correlating to stronger hydrogen bonding environments due to the excess proton; (2) an acid continuum from 2000-3200 cm^{-1}, which is commonly ascribed to more Eigen-like configurations; (3) a peak at 1200 cm^{-1} corresponding the proton transfer mode (PTM) between two flanking waters; and (4) a peak at 1750 cm^{-1} corresponding to flanking water bend.

More recently, non-linear spectroscopy experiments have been pioneering experimental efforts to understand the hydrated excess proton.[21, 57-61] Experimental studies of acid clusters in acetonitrile mixtures observed the PTM $|1\rangle \rightarrow |2\rangle$ transition was greater than the $|0\rangle \rightarrow |1\rangle$ transition. This was used to propose a 1-dimensional potential energy surface (PES) for the PTM that had a symmetric double-energy well, a characteristic of a Zundel cation.[60-61] Two-dimensional infrared spectroscopy was also used to excite the O-H stretching vibrations in acid solutions around 3150 cm^{-1} and detected spectral responses within a spectrum ranging from 1500 – 4000 cm^{-1}.[58] By assigning 1750 cm^{-1} to the bending vibration of the flanking waters of the Zundel complex, they reported that the population of the Zundel-like cation is larger than previously proposed in theoretical studies, leading them to conclude that it serves as more than a simple intermediate. Their subsequent studies using 2D IR[21] further suggest that the potential energy surface (PES) is not a symmetric double-energy well characteristic of a symmetric Zundel cation, but rather incorporates a distortion into the underlying PES of the hydrated excess proton. Additionally, by examining data obtained from parallel and perpendicular 2D IR spectra at 1750 cm^{-1}, an anisotropy timescale of ~2.5 ps was observed for 2M HCl solutions,[57] correlating with irreversible proton transport. In defining the excess proton as *Zundel-like* in these studies, researchers emphasize the excess proton shared between two flanking waters, synonymously known as a special pair.

Experimental IR spectra of acidic solutions have revealed time-averaged structures. However, it is not uncommon for theoretical studies to use static configurations to correlate vibrational motion with infrared frequency.[77-78] When using static configurations, theoretical studies commonly implement the local δ parameter to characterize the solvation structure of the hydrated proton. This δ parameter conveys information on how the excess proton is shared between its flanking water molecules in the special pair and is defined by Eq. 2.1:

$$\delta = \left|\boldsymbol{r}_{O^{*}H} - \boldsymbol{r}_{O^{SP}H}\right| \tag{2.1}$$

A δ parameter of 0 represents a proton shared equally between two water molecules and is described as Zundel-like; in contrast, an increasing δ parameter represents a proton that is associated more with a single water molecule, which then forms a more Eigen-like complex. However, Dor et al.[78] and others[16, 61] have questioned the validity of the δ parameter to clearly distinguish the solvation structure of the hydrated excess proton. For example, Dor et al.[78] stressed, since the distribution is non-bimodal it is difficult to clearly distinguish the hydrated excess proton as being either distinctly Zundel or Eigen.

Swanson et. al.[16] also discussed the degree of information gained from the δ parameter. Specifically, by applying an ab initio energy decomposition analysis (EDA), they reported that the sum of the δ values within a distorted Eigen complex and Zundel complex can qualitatively track the degree of charge transfer within the first solvation shell of the hydrated excess proton (see Figures 6 and 7 in Ref[16]). By tracking the δ value of the excess proton as a function of time during which the proton does not hop (i.e., special pair dance), they quantified the δ value to be less than 0.1, which limits the ability to apply δ parameter values toward characterizing the solvation structure of the hydrated excess proton from a single snapshot. The authors concluded that studying the dynamics of the excess proton is more revealing for determining the solvation structure of the hydrated excess proton. Within this definition, therefore, Eigen-like dynamics can be characterized by periods during which the identity of the special pair changes; conversely, Zundel-like dynamics can be characterized by proton hopping back-and-forth between two water molecules over an extended period of time. This definition is also supported elsewhere in the literature.[79]

By using equilibrium trajectories of the hydrated excess proton and instantaneous normal mode analysis, this investigation was designed to elucidate the dynamics of the hydrated excess proton in support of recent spectroscopic results. Based on these equilibrium trajectories, we are able to capture specific processes that give rise to anisotropy decay. As detailed herein, we document the 2.5 ps timescale corresponding to proton transport observed by recent nonlinear spectroscopy, while confirming the structure of the hydrated excess proton to be distorted-Eigen. Additionally, we explicate the dynamics of normal modes for the hydrated excess proton that validate distorted-Eigen configurations at the 1750 cm^{-1}, while also detailing the limitations of the δ parameter to characterize vibrational modes.

This paper is outlined as follows: In Section II we outline the MS-EVB and EDS-AIMD methods used to determine anisotropic data, while also providing simulation details. In Section III, we use radial distribution functions (RDF) to show the solvation structure of the hydrated excess proton as being best characterized by a distorted Eigen cation. We then provide our anisotropic data for the distorted-Eigen cation, as well as time-evolution of normal modes of special pair dance. In Section IV, we offer our conclusions.

II. Methods

A. Simulation Methods

Two simulation methods were used to conduct this investigation: the Multistate-Empirical Valence Bond (MS-EVB) Method,[11, 45-48, 80-81] and Experiment Directed Simulations[41] of *ab initio* molecular dynamics (EDS-AIMD).[43] We briefly explain the theory behind these methods, but we direct the reader to the literature for further detail.

In the MS-EVB formalism, the hydrated excess charge is delocalized amongst multiple water molecules by creating a wavefunction that is a linear combination of bonding states. In each diabatic state, a different water molecule is covalently bonded to the excess proton.

$$\lfloor\Psi\rangle = \sum_{i=1}^{\text{nstates}} c_i^2 \lfloor i\rangle \tag{2.2}$$

Once the wavefunction is constructed, the coefficients of the ground state wavefunction are determined through an eigenvalue problem using a quantum-like Hamiltonian, as follows:

$$\boldsymbol{Hc} = E_0\boldsymbol{c} \tag{2.3}$$

In the Hamiltonian, the diagonal elements are defined using molecular mechanics force field terms, augmented by a repulsive term to correct for the over-sticking of water molecules to the hydronium molecule; meanwhile, off-diagonal elements are used to couple the different diabatic states.

For this investigation we used MS-EVB 3.2 and anharmonic MS-EVB 3.2.[81] In comparison to previous models, a Lennard-Jones term was incorporated to account for the fourth water pre-solvation around the hydronium.[33] An anharmonic model incorporates non-harmonic vibrations in solvating the water molecules. As previously described, MS-EVB 3.2 was used to explain infrared spectroscopy data and to calculate normal modes using B3LYP.[77, 82]

To compare our results with another simulation method, we also utilized EDS-AIMD simulations. Such an approach corrects for the over-structuring of water in BLYP/BLYP-D3 AIMD simulations by including an additional potential energy term (Eq. 2.4) to the system's Hamiltonian that corrects the system's Ow-Ow observable to match experiments.

$$\mathrm{V}(\mathrm{r_i}) = \sum_{\mathrm{k}=0}^{3} \frac{\alpha_\mathrm{k}}{\hat{f}_k} \sum_{\mathrm{j}\neq\mathrm{i}}^{\mathrm{n_O}} \mathrm{r_{ij}^k}\left[1 - \mathrm{u}\left(\mathrm{r_{ij}} - \mathrm{r_0}\right)\right] \tag{2.4}$$

In EDS, the potential energy includes the coupling constant (α_k), the experimental target value ($\hat{f}_k$), and the coordination number; it utilizes a mollified smoothing function to make the coordination number and its statistical moment continuous. The coupling constant in eq. 2.4 was parameterized so that the oxygen-oxygen coordination number and its first-through-third moments could accurately reproduce experimental results. By directly biasing the oxygen-oxygen coordination number and its moments, other structural and dynamical properties were improved without increased computational costs.

B. Simulation Details

In total, ten independent MS-EVB 3.2 and aMS-EVB 3.2 simulations of 1 HCl in 256 H_2O with a box length of 19.73 Å were first equilibrated in the NVT ensemble using a Nose-Hoover thermostat with a temperature set to 298 K and a time-constant of 50 fs using an in-house version of the LAMMPS simulation package.[83] Water molecules were modelled using SPC/Fw[84] and aSPC/Fw[80] for MS-EVB 3.2 and aMS-EVB 3.2,[49] respectively. After a 1 ns non-reactive equilibration period, each simulation was equilibrated using our reactive molecular dynamics simulation code for 500 ps in the NVT ensemble, and all production runs were carried out in the NVE ensemble for 1 ns. Each reactive simulation was conducted with a timestep of 0.5 fs using a long-range cutoff of 9.0 Å and an Ewald summation with an error of 10^{-5}.

In total, three EDS-AIMD simulations of 1 HCl in 128 water molecules with a box length of 15.64 Å were equilibrated in the NVT using a Nose-Hoover thermostat with a time-constant of 11.12 fs, followed by 80 ps in the NVE ensemble. EDS parameters were identified from our previous work[43] for the BLYP exchange-correlation functional[26-27] with the D3 Grimme dispersion interactions.[85-86] All EDS-AIMD simulations were carried out with Quickstep module in CP2K[87] and PLUMED[88] package using Goedecker-Teter-Hutter (GTH) pseudopotentials[89] with a TZV2P basis set using a plane-wave cutoff of 400.

C. Instantaneous Normal Mode Analysis

Instantaneous normal mode (INM) calculations[90-91] were determined to further compare structural vibrations and infrared frequency, with the goal of clarifying the solvation structure of the hydrated excess proton. Instantaneous normal mode analysis (NMA) calculations were derived from a prior report,[77] but were augmented by using both MS-EVB 3.2 and EDS-AIMD trajectories. The hydrated excess proton was identified as the proton in the hydronium cation with the lowest δ value; all water molecules within a 5 Å radius were included in the NMA calculation. Further NMA calculations restricted the number of water molecules to include only those in the second solvation shell, since this approach was shown to capture the extent of charge-delocalization in the excess proton complex.[16] All NMA calculations were calculated using the B3LYP exchange-correlation functional[92] with a 6-31 G(p,d) basis set in the Gaussian 09 software package.[93] It should also be noted that each NMA was carried out in the absence of energy minimization, and all imaginary frequencies were discarded prior to analysis.

III. Results and Discussion

A. Solvation Structure of Hydrated Excess Proton

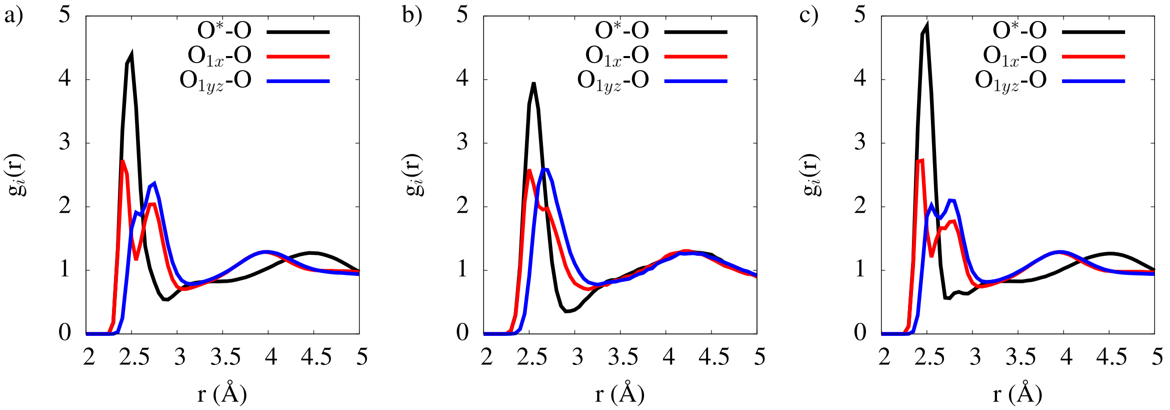

Figure 2-1: O-O radial distribution functions of the O*-Ow (black), O1x-Ow (Red), and O1yz-Ow (Blue) for (a) MS-EVB 3.2, (b) EDS-AIMD, and (c) aMS-EVB 3.2.

Figure 2-1 illustrates the O-O radial distribution functions (RDF) for the various simulation methods. The O-O RDFs include all oxygen atoms in the system, those centered on the most probable hydronium (O*, black), the special pair oxygen ($O_{1x,}$ red), and the remaining water molecules in the protonated complex (O_{1yz}, blue). In these calculations, O_{1x}, O_{1y} and O_{1z} are defined as the neighboring water molecules with increasing δ value around the most probable hydronium, respectively.

In all simulation methods, the O^*-O_w RDFs evidence a unimodal peak centered at ~ 2.5 Å, which is attributed to three water molecules fluctuating around the hydronium, as determined by integrating the first peak. However, the O_{1x} RDFs show a prominent peak at a shorter distance, representing the interaction of the O_{1x} with the hydronium oxygen atom, while succeeding peaks correspond to the O_{1x} interaction with second solvation shell of the O^*. This trend was also identified in the O_{1yz} RDF, with the exception that the EDS-AIMD method was unimodal. As determined via EDS-AIMD, the O^*-O_{1yz} and O_{1yz}-O_w interactions were noted to be quite similar, which explains the unimodal peak in the O_{1yz}; this finding is further supported by the O_{1yz} RDF having an integration value close to 4.

Note that the solvation structures of the hydronium and the special pair oxygen are not identical, as indicated by different O^* and O_{1x} RDFs. In a symmetric Zundel cation, the proton would remain in the center of the two flanking water molecules, which would then make the flanking waters nearly identical. Even when proton rattling is factored into this Zundel picture, the ensemble average of this rattling would still account for identical flanking water molecules and nearly identical solvation structures for the O^* and O_{1x}, which is not observed in these methods. Recent simulation studies that proposed symmetric Zundel cations is the dominate species in solution have additionally distinguished Zundel and Eigen cation based on the O_{1x} distance being less than or greater than 2.7 Å, respectively. [61] This classification method can be misleading since we note that in the simulation methods reported here, all O_{1x} distances were found to be less than 2.7 Å while herein a symmetric Zundel picture conflicts with the discrepancy in O* and O_{1x} RDFs.

On the other hand, the obtained RDFs indicate a clear distinction between the water molecule with the excess proton (O^*) and the special pair (O_{1x}), which is characteristic of a distorted Eigen. The Eigen cation has also been suggested as the thermodynamic stable structure in recent theoretical studies which used activate rate theory to characterize proton transport in water.[94] In a two-water configuration,[78] we see clear evidence of a single water molecule positioned closer to the hydronium molecule, which is in agreement with the RDFs found in Figure 2-1. However, these snapshots ignore the dynamics of the protonated complex. If the two-water model represented the actual dynamics of the system, the O^*-O_w RDF would match the O_{1x} RDF, corresponding to a dominant first peak for the special pair and integrating to a coordination of a single water molecule. In contrast, the ensemble and time-averaged structure shows a single peak in the O*-Ow RDF and an integration of three water molecules. Given these findings—coupled with the preference for the excess proton to associate with one water molecule—we believe that a distorted Eigen best characterizes the hydrated excess proton. By using a distorted Eigen picture, we encapsulate the special-pair (or the two-water picture), while additionally accounting for the dynamics of the excess proton.

B. O*-Ow Anisotropy Decay

Recent nonlinear infrared spectroscopy data indicate that the reorientation timescale of the hydrated excess proton is about 2.5 ps,[57] which was confirmed by calculating the anisotropy decay via the parallel and perpendicular pulses at 1740 - 1790 cm^{-1}. In this seminal work, the vibrational bending of the flanking water molecules in the special pair was assigned to 1750 cm^{-1}. Specifically, this work eliminated specific phenomena—notably, the complete reorientation of the hydrated excess proton complex without proton transfer, rapid structural fluctuations, and energy and thermal transfer from the hydrated complex to surrounding aqueous environment—as possible structural reorientations that explain the 2.5 ps. Instead, it was suggested that the 2.5 ps reorientation timescale corresponded to irreversible proton transfer. Additionally, it was claimed that special pair dance could not explain the 2.5ps, as it would have caused the transition dipole moment to decorrelate faster than 2.5 ps.

Here, we seek to understand structural reorientations in the hydrated excess proton complex that correspond to these experimental anisotropy timescales, with special interest in elucidating the nature of the special pair dance and irreversible proton transport. It is very common in MD simulations of water to calculate the anisotropy of the O-H stretch by using the unit vector along the O-H bond.[95] Given recent findings using a two-water or special pair approach, we decided to define the unit vector along the O*-Ow axis of the special pair. Anisotropy calculations were determined using the second Legendre polynomial (Eq. 2.5) of the unit vector defining the special pair.

$$C_2(t) = \frac{\langle P_2(\hat{u}(t)\hat{u}(0))\rangle}{\langle P_2(\hat{u}(0)\hat{u}(0))\rangle} \tag{2.5}$$

Here, the $\langle \dots \rangle$ denotes both an ensemble average and a time average of the unit-vector. In our molecular simulations, the special pair is defined as the O*-Ow that has the lowest δ parameter.

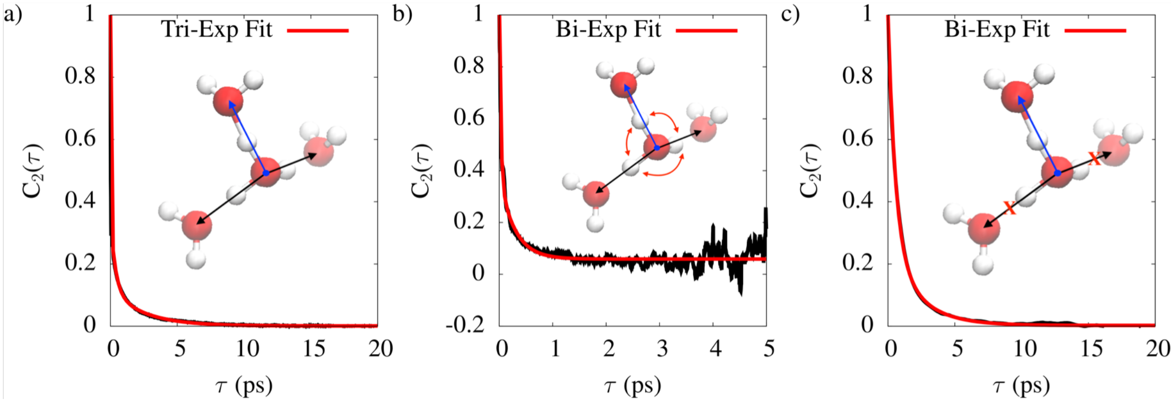

Figure 2-2: Anisotropy plots using Eq. 2.5 for the O*-Ow unit vector. The anisotropy plots are broken down based on (a) total anisotropy, (b) special pair dance, and (c) long-lived special pair.

Figure 2-2a illustrates the anisotropy decay of the O*-Ow special pair from MS-EVB 3.2 simulations (corresponding O*-Ow anisotropy plots for aMS-EVB and EDS-AIMD can be found in Appendix A). By fitting a triple exponential fit to total anisotropy decay (see Discussion in Appendix A), we obtained time constants of 12 fs, 0.37 ps, and 2.49 ps, with corresponding amplitudes of 0.65, 0.23, and 0.12. Comparable values have been obtained from other simulation methods, as indicated in Table 2-1. Of particular importance is that these time constants and amplitude data can be replicated across various simulation methods, confirming that our findings are not unique to our MS-EVB simulations. Also note that one of the three processes within the tri-exponential fit is very close to the 2.5 ps time constant determined experimentally.[57] To identify the precise structural phenomena corresponding to these time constants, we removed specific structural dynamics from our anisotropy calculations and refit that data to a bi-exponential function. Since we observed strong agreement between MS-EVB and EDS-AIMD simulations, we conducted subsequent calculations only using the MS-EVB method, as it can be run much longer and provide better statistics in comparison to the EDS-AIMD approach.

Table 2-1:Tri-exponential fits to the Total Anisotropy Calculations

System	A_1	τ_1 **(fs)**	A_2	τ_2 **(ps)**	A_3	τ_3 **(ps)**	C
MS-EVB	0.65	12	0.23	0.37	0.12	2.49	0.00
aMS-EVB	0.66	10	0.23	0.32	0.11	2.25	0.00
EDS-AIMD	0.72	17	0.16	0.35	0.12	2.47	-0.01

First, we removed any contribution associated with proton transfer from the anisotropy measurements, and then decomposed the total anisotropy based on the special pair dance. This is a process wherein the identity of the excess proton changes in a distorted Eigen cation, but in the absence of any change in the identity of the central hydronium core. We then parsed the trajectory into segments where the proton remained on a single water molecule, and then calculated the unit vector for the special pair. The anisotropy was then calculated for each segment and then averaged over all segments. The special pair dance anisotropy calculation is shown in Figure 2-2b for MS-EVB 3.2; as indicated therein, we obtained time constants of 28 fs and 0.29 ps from a bi-exponential fit. Note that these bi-exponential constants are quite comparable to those obtained using other simulation methods (Table 2-2). Previous MS-EVB simulations have shown that the identity of the special pair changes on average 1 every 40 fs, which is very close to the 28 fs identified in this anisotropy calculation. This rapid timescale is too fast to be resolved by experimental techniques; in fact, it is faster than the shortest pulse obtained experimentally.

Table 2-2: Bi-exponential fits to the Special pair Dance Anisotropy Calculations

System	A_1	τ_1 **(fs)**	A_2	τ_2 **(ps)**	C
MS-EVB	0.68	28	0.32	0.29	0.06
aMS-EVB	0.70	28	0.30	0.30	0.05
EDS-AIMD	-	-	-	-	-

In a similar manner, we addressed the slow time constant by removing the special pair dance from total anisotropy calculations. Using this approach, we no longer define the special pair as the O*-Ow pair with the lowest δ value, but rather as the O-O vector between the hydronium oxygen and the water oxygen to which the excess proton hops. For example, if at timestep 0 the hydronium oxygen is molecule A, and then at timestep t the hydronium oxygen is molecule B, then the special pair unit vector from timestep 0 to timestep t is defined as the O-O unit-vector between molecule A and B. The anisotropy calculation for MS-EVB 3.2 is found in Figure 2-2c. Table 2-3 provides amplitude and time constant data for the various methods. Note that for MS-EVB 3.2, we identified time constants of 0.56 ps and 2.17 ps, which are comparable and in close agreement with the intermediate and longer time constants listed in Table 2-1. The 2.17 ps result is also in excellent agreement with the 2.5 ps reported from non-linear spectroscopy.

Table 2-3: Bi-exponential fits to the Long-Lived Anisotropy Calculations

System	A_1	τ_1 **(ps)**	A_2	τ_2 **(ps)**	C
MS-EVB	0.74	0.56	0.26	2.17	0.00
aMS-EVB	0.67	0.53	0.33	1.79	0.00
EDS-AIMD	-	-	-	-	-

It should be noted that we were able to analyze these anisotropy plots while holding a distorted-Eigen picture of the hydrated excess proton. By removing the special pair dance from the distorted-Eigen cation we were able to retain the long-lived time constant; analogously, by removing proton transport we were able to retain the special pair dance. In addition to confirming strong agreement between the time constants and amplitudes between the bi-exponential fits to the total tri-exponential fits, these findings indicate that (a) the fast time constant correlates to special pair dance, and (b) the slow time constant corresponds to irreversible proton transfer. These hypotheses are supported by the good agreement of timescales and physical processes obtained from recent 2D IR experiments.

C. Instantaneous Normal Mode Analysis using 5 Å Radial Cutoff

Our simulation methods show excellent agreement with anisotropy timescales determined experimentally. In contrast, a deficiency of experimental verification of the special pair dance prompted this investigation of the correspondence between the special pair dance and specific vibrational frequencies. With the special pair dance depicted as a series of dynamic switches between the hydrated excess proton, we utilized configurations within a 100 fs timespan from MS-EVB and EDS-AIMD results that correspond to the special pair dance. Instantaneous Normal Mode (INM) analysis was then applied to configurations separated by 1 fs, which differs from prior gas phase NMA calculations that pull randomly selected configurations; accordingly, our method enables us to observe the time-evolution of normal modes.

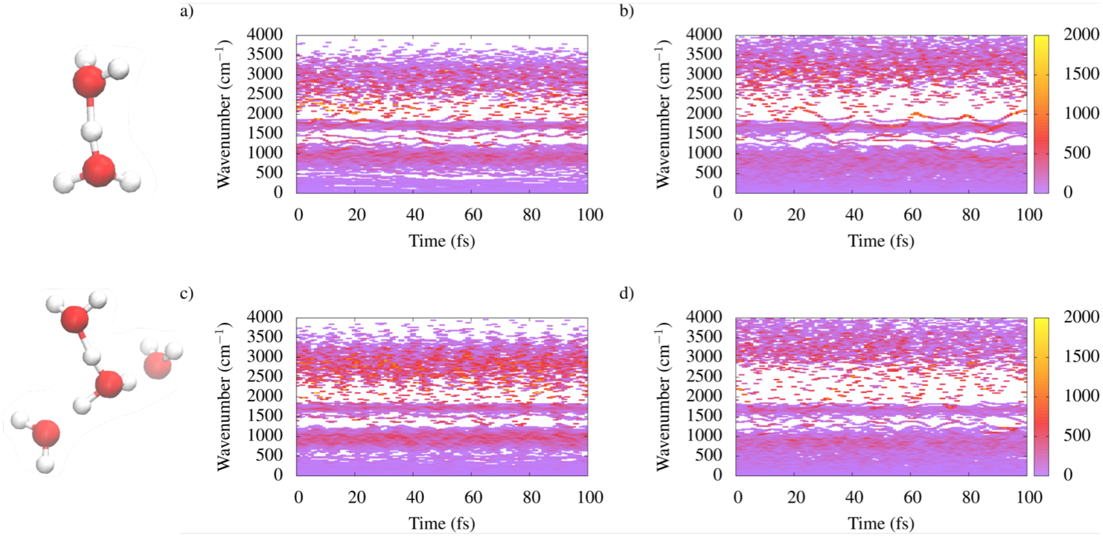

Figure 2-3: Spectral density as a function of time for Zundel (a & b) and Eigen (c & d) configurations using configurations taken from MS-EVB 3.2 (a & c) and EDS-AIMD (b & d). Zundel and Eigen are defined based on have 1 (Zundel) or 3 (Eigen) unique special pair water molecules during the 100 fs segment.

Two 100-fs segments obtained from MS-EVB 3.2 and EDS-AIMD simulations were selected where the hydronium molecular index remained unchanged. In the first segment, the identity of the special pair changed between the three water molecules; in contrast, the identity of the special pair remained unchanged in the second segment. We defined the first 100-fs segment as “Eigen”, and the second as “Zundel”. All waters and hydronium molecules whose oxygen atoms were found to reside within a 5 Å radial cutoff of the excess proton were included in the INM calculations. It should be noted that during the Eigen segment, the identity of the excess proton changed and was subsequently identified as the proton between the special pair. With the change in identity of the excess proton, the center of the 5 Å cutoff would also change; as such, some water molecules would be removed from the INM calculation and included in the configurations.

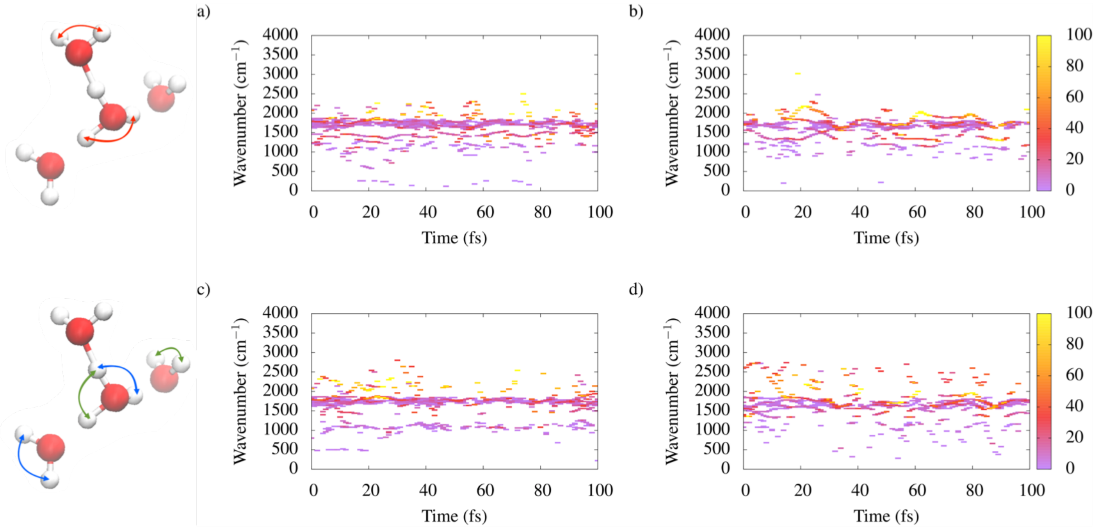

Figure 2-4: Spectral density as a function of time for H-O-H bends in a Zundel configuration using data obtained from MS-EVB 3.2 (a & c) and EDS-AIMD (b & d) simulations. Figures a and b show the spectral density for H-O-H bends >5° in the special pair, while Figures c and d show the spectral density of H-O-H bends >5° in other O*-Ow pairs.

Figure 2-3 shows the spectral density of the normal modes as a function of time, with configurations pulled from MS-EVB 3.2 and EDS-AIMD trajectories. Upon first inspection we see many similarities in the spectral density plots, independent of the simulation method and whether the 100 fs segments were defined as Eigen or Zundel. The most striking difference is the mean distribution of the OH stretches obtained from MS-EVB and EDS-AIMD simulations. Of special interest is the frequency range around 1750 cm^{-1}, since this data corresponds to the special pair flanking water bend. As indicated in Figure 2-3, there is a persistent spectroscopic signature at this frequency for both Zundel and Eigen configurations, which is not found only within a Zundel complex.

We next selected normal modes from these calculations that evidenced flanking water bending within the Zundel trajectory (Figure 2-4) and Eigen trajectory (Figure 2-5). If both flanking H-O-H angles in the special pair (Figure 2-4a,b and Figure 2-5a,b) or other O*-Ow pairs in the first solvation shell (Fig, 2-4c,d and Figure 2-5c,d) changed by more than 5 degrees, normal modes were then pulled and their spectral densities were plotted. For each timestep, the spectral density was then divided by the number of selected normal modes within that timestep to help compare the time-evolution of the spectral density. In both the Zundel and Eigen trajectories, H-O-H bending could be found at 1750 cm^{-1} that did not result from the special pair, but rather from other O*-Ow pairs in the distorted-Eigen cation. This finding confirms that the 1750 cm^{-1} frequency is independent of the structure classification, which is in good agreement with our prior work indicating that vibrations at 1750 cm^{-1} can delocalize across 5-20 atoms.[77] This outcome may also explain why experimentally obtained data could not substantiate the special pair dance, in that many H-O-H bending vibrations could be excited instead of the special pair itself.

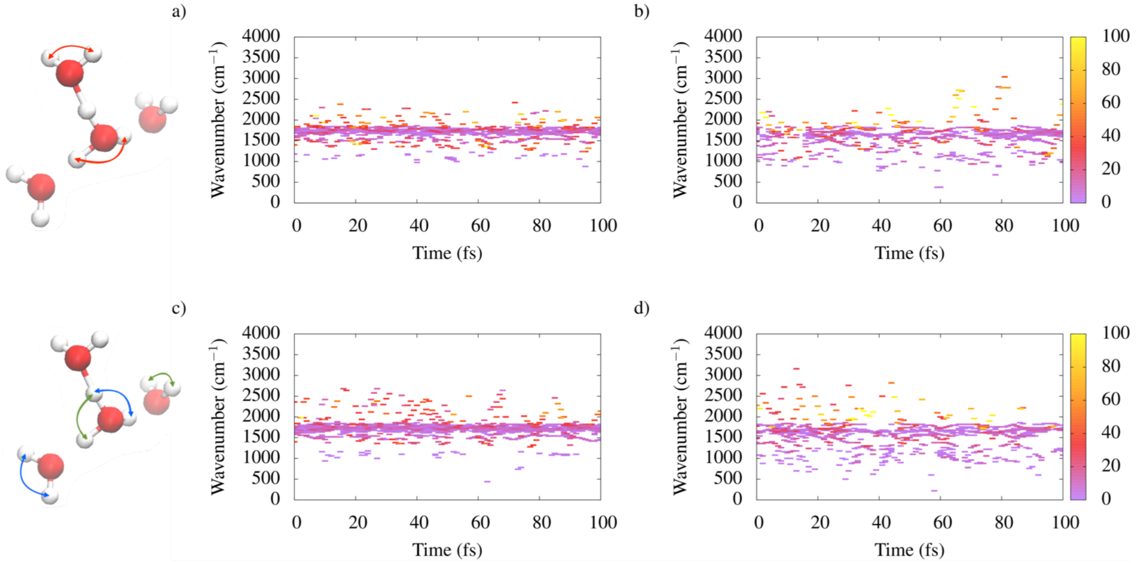

Figure 2-5: Spectral Density as a function of time for H-O-H bends in an Eigen configuration using configurations taken from MS-EVB 3.2 (a & c) and EDS-AIMD (b & d). Figures a and b show the spectral density for H-O-H bends >5° in the special pair, while Figures c and d show the spectral density of H-O-H bends >5° in other O*-Ow pairs.

D. Normal Mode Analysis Using Second Solvation Shell

Wave-like oscillations observed in some of the normal modes (specifically in Figure 2-4a,b and Figure 2-5a,b) could arise from an inconsistency in the number of water molecules in the normal mode calculations due to the identity change of the hydrated excess proton. Accordingly, we restricted the number of water molecules to include only those within the second solvation shell of hydronium as this was found to contain most of the charge transfer within the hydrated excess proton complex.[16] Figure 2-11 in Appendix B illustrates the density of states and spectral density from these two INM calculations for the Eigen cation. Note the excellent agreement between the 5 Å cutoff and the second solvation method, as well as nearly identical spectral densities as Figures

2-4 and 2-5 from when we restrict the calculation to only the second solvation shell (Appendix B, Figure 2-12). Additionally, we obtained nearly identical wave patterns as these previous instantaneous normal modes, which indicates that the oscillations in these normal modes are not due to water molecules moving in and out of the NMA calculation.

Oscillatory patterns were also identified by Swanson and Simons in the charge transfer energy of the hydrated excess proton; moreover, they observed that the δ parameter qualitatively agreed with the trend in charge transfer (see Figure 4 in Ref. [16]). They also proposed defining Eigen and Zundel cations based on the dynamics of the excess proton rather than the δ parameter. In time segments characteristic of a distorted Eigen cation, they observed instances during which the δ parameter became less than 0.1 Å. Such findings would typically describe a Zundel cation; however, when placed in the context of the complex's dynamics, it would show a distorted Eigen since the special pair is rotating among the three waters. They further proposed that Zundel cations could be characterized by an excess proton rattling between two water molecules. In this next session, we therefore address how the δ value can track the charge transfer in distorted Eigen cation with and without a δ value less than 0.1 Å, and a Zundel cation described by a proton rattling between two waters.

We begin by examining the INM of the Eigen configurations of Fig. 2-3 and 2-5 which had the identity of the excess proton change within the Eigen complex without any change in the central hydronium core. In Figure 2-6a we show the δ value for the three protons in the complex. We assigned yellow squares to indicate the proton with the lowest δ value, which is used to distinguish the excess proton. In this segment, we find that the δ values of all three protons are very comparable with very similar mean values. We specifically point out that this is characteristic of the special pair dance, where the identity of the excess proton alternates with the other protons in the distorted Eigen complex. Figure 6 b-d illustrates the spectral density for each hydrogen in cases when the O_H-H_H distance of the hydronium molecule changes by more than 0.2 Å, and we superimposed the δ value for each proton over its spectral density features and scaled them to fit the plot. In this particular distorted Eigen segment, the δ value of the excess proton never goes below 0.1 Å, but nevertheless switches with the other protons in the complex. However, we find noticeable agreement between the shape of the normal mode oscillations and the δ parameter eluding to the charge transfer nature of each proton in the normal modes, and these specific normal modes are close to the bulk-like water stretches around 2500 cm^{-1}.

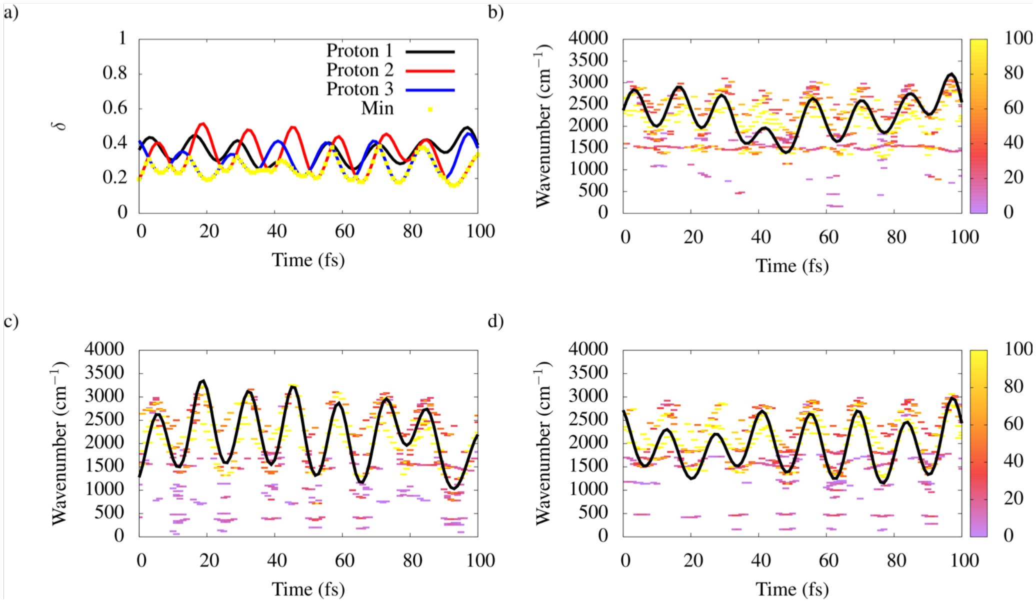

Figure 2-6: Spectral density and δ value for the hydronium's protons in an Eigen configuration of MS-EVB 3.2. Figure a shows the δ values for the three protons. The proton with the lowest δ value (i.e. the excess proton) is highlighted in yellow. Figure b-d shows the spectral density for protons 1, 2, and 3, respectively. Normal modes are selected if each proton's O*-H_H stretches more than 0.2 Å. In black we overlay each proton's δ value multiplied by 6,500 to fit the figure.

We do the same analysis on another Eigen configuration, but this time we examine a 100 fs which incorporates the special-pair dance that has a proton with a δ value less than 0.1 Å (Figure 2-7a). In this configuration, proton 1 begins as the excess proton and is the excess proton for the majority of the 100 fs, with proton 2 competing as the excess proton at the beginning of the segment, and proton 3 competing as the excess proton at the end of the segment. Additionally, the δ value of proton 1 is found in the region typically identified as Zundel, although, in light of the special-pair dance, it is best described as a distorted Eigen cation. We show the corresponding normal modes for this configuration in Fig. 7 b-d. For proton 1 (Fig. 2-7b) we see spectroscopic signatures that are much more red-shifted in comparison to the other two protons in the distorted Eigen cation. Comparably, when proton 2 competes with Proton 1 as the excess proton, we find some normal modes around 1750 cm^{-1}, yet as the simulation continues, its δ value increases and its corresponding normal modes are blue shift to larger frequencies around 2750 cm^{-1}, which are much closer to bulk-like water stretches. This trend is found in the reverse order for Proton 3, where at the beginning of the 100 fs segment, it has the largest δ value and therefore has the smallest charge transfer to its adjacent water molecule. However, at around 60 fs, Proton 3 competes with Proton 1 as the excess proton and normal modes are slightly red shifted.

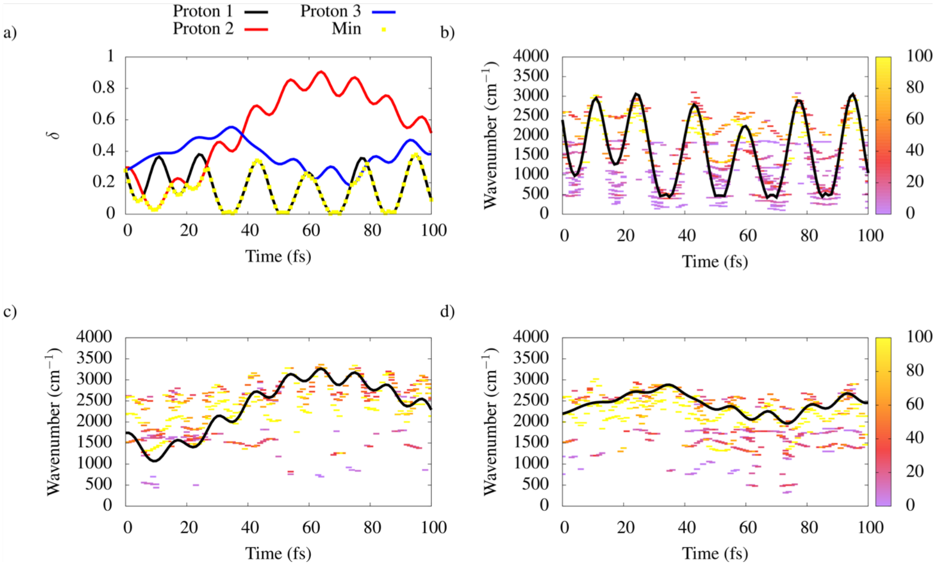

Figure 2-7: Spectral density and δ value for the hydronium's protons in a distorted Eigen configuration of MS-EVB 3.2. Figure a shows the δ values for the three protons. The proton with the lowest δ value (i.e. the excess proton) is highlighted in yellow. Figure b-d shows the spectral density for protons 1, 2, and 3, respectively, with each proton's δ value scaled to fit the figure in black. Proton 1's δ value was scaled by δ*7,000 + 400, Proton 2's δ value was scaled by δ*2,500 + 1000, and Proton 3's δ value was scaled by δ*2,500 + 1500. Normal modes are selected if each proton's O*-H$_H$ stretches more than 0.2 Å.

Figure 2-8 depicts the instantaneous normal modes for protons in a Zundel complex from 100 fs time segment using the definition of Swanson and Simons. Water molecules found within first two solvation shells of each oxygen in the Zundel cation were selected and used for normal mode analysis. Proton 1 is the excess proton, while Protons 2-5 represent the protons in the flanking waters. In all cases, each proton's δ value follows the shift in their corresponding normal mode. As indicated in Figure 2-7c, Proton 1 has spectroscopic signatures in the 1000 – 2000 cm^{-1} range that contains the PTM (1200 cm^{-1}) and the flanking water bend (1750 cm^{-1}) when the O-H bond in the normal mode changes by 0.2 Å. Conversely, Proton 2 within the Zundel complex evidences a larger frequency signature than the excess proton (~ 2900 cm^{-1}), and additionally, it displays a red shift in its normal mode frequency when its δ value closely approximates the δ value of Proton 1 (~80-100 fs in Figure 2-7d), showing a greater degree of charge transfer and characteristics similar to those of excess proton.

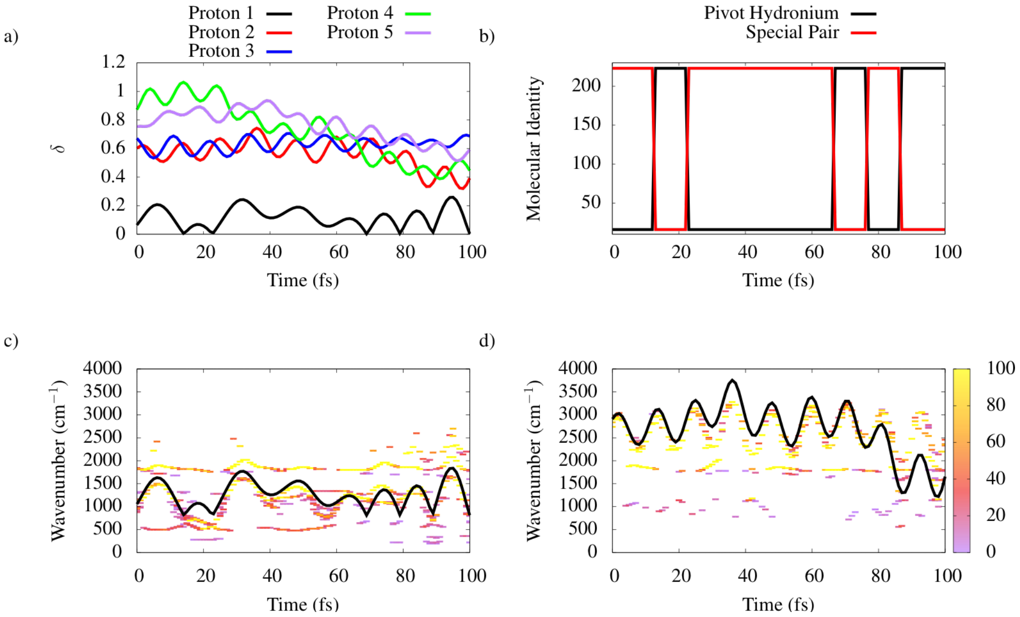

Figure 2-8: Spectral density and δ value for the protons in a Zundel configuration of MS-EVB 3.2. Figure a shows the δ values for the excess proton (Proton 1) and the 4 flanking protons (Protons 2-5). Figure b show the dynamics of the hydronium molecular identity. Figure c and d shows the spectral density for the excess proton (Protons 1) and proton 2 overlaid with their δ value scaled by δ*4,000 + 800 and δ*6,000-700, respectively. Normal modes are selected if each proton's O*-H$_H$ stretches more than 0.2 Å.

While the quantitative results described herein do not imply a direct correlation between structural geometries and instantaneous normal modes, they do further validate the work of Swanson and Simons. Specifically, due to the strong connection between the δ parameter and charge transfer within the hydrated excess proton, we propose that the oscillations in the instantaneous normal modes are driven by the charge transfer between each proton and its neighboring water molecule. Moreover, our findings indicate that the instantaneous normal modes correspond to the identity of the excess proton; specifically, each proton's normal modes red-shift as their δ parameter (and respective charge transfer) decreases as shown in the two Eigen configurations and Zundel configurations. Thus, it appears that the δ parameter can assist in determining the single proton that is the excess proton; however, determining the excess proton without the context of the hydrated complex's dynamics can be misleading as is clearly seen in the Eigen configuration with δ values less than 0.1 Å.

IV. Conclusion

We used MS-EVB, aMS-EVB, and EDS-AIMD simulations to confirm the structure of the hydrated excess proton as a distorted Eigen cation, while obtaining anisotropy decay data that closely match those obtained via nonlinear spectroscopy. By decomposing the anisotropy based on structural phenomenon, we were able to identify anisotropy timescales that give rise to the special pair dance and the long-time decay of irreversible proton transfer. These timescale processes agree with previous theoretical studies of the hydrated excess proton,[19-20] as well as replicate the 2.5 ps anisotropy timescales achieved experimentally.[57]

By examining the spectroscopic signatures of the protons within Eigen and Zundel cations, we observed that the δ parameter tracks the shift in the normal mode of each proton, which has been shown to characterize the charge transfer within the hydrated excess proton complex. Additionally, we noted that the excess proton defined by the lowest δ value around the hydronium molecule has a distinct spectroscopic signature in comparison to other protons in the complex. However, it must be noted that the identity of the excess proton is constantly changing prior to the occurrence of an irreversible proton transfer event (i.e.. special pair dance). We conclude, therefore, that the δ parameter can characterize the excess proton, while at the same time emphasizing that selecting static structures from MD simulations and determining spectroscopic information can be problematic without examining the dynamics.

Experimental anisotropy decay data for the flanking water bend show that increasing the chloride concentration decreases the proton transfer rate, while Arrhenius plots of the anisotropy timescales indicate that increasing the chloride concentration lowers the activation energy of irreversible proton transport.[59] Transition state theory was used to confirm that additional chloride ions, rather than excess protons, create entropic barriers to irreversible proton transport. Similarly, very recent theoretical work[94] has also shown a concentration dependence on the O*-Cl ion pairing and proton transfer rate using transition state theory and Marcus theory, while finding the Eigen cation as the thermodynamic stable state and the Zundel cation as a reaction intermediate. Our future works will provide atomistic support to these phenomena by examining the influence of temperature and concentration in HCl solutions.

Additional theoretical work need to be undertaken to clarify the strong parallel preference found in recent experiments addressing PTM and flanking water bend, as this is a strong argument for a distorted Zundel cation. We argue, however, that the laser pulses in these experiments are longer than the shortest special pair lifetimes. Moreover, any experimental approach that focuses on averaged structures will make the goal of determining precise structure-to-frequency correlations more challenging. Nonetheless, thorough theoretical studies are needed to address these issues.

Appendix A: Anisotropy Plots, Fits and Justification for Anisotropy Fitting Method

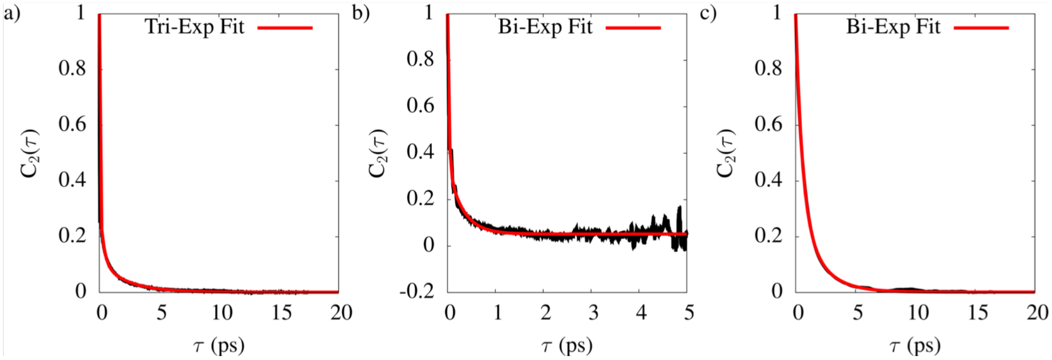

Figure 2-9: Anisotropy plots for the O*-Ow unit vector in aMS-EVB 3.2. The anisotropy plots are broken down based on (a) total anisotropy, (b) special-pair dance, and (c) long-lived special-pair.

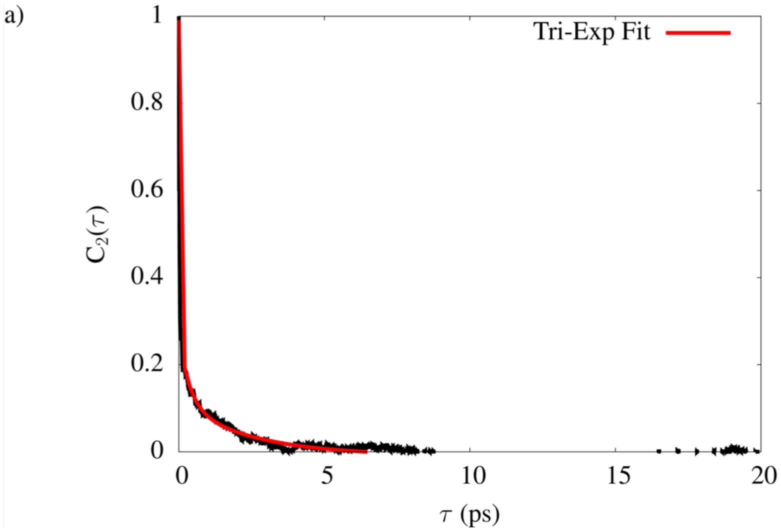

Figure 2-10: Total anisotropy plots for the O*-Ow unit vector in EDS-AIMD. Limited statistics prevent us from calculating the EDS-AIMD anisotropy of special-pair dance and long-lived special-pair.

A. Total Anisotropy

Experimental anisotropy curves with fit using a bi-exponential fit. However, we found using tri-exponential fits best fit the curve as going from bi-exponential (Table 2-4) to tri-exponential (Table 2-5) increase the R^2

$$f(x)= a_1 \cdot \exp\left({}^{-x}/_{\tau_1}\right) + a_2 \cdot \exp\left({}^{-x}/_{\tau_2}\right) + a_3 \cdot \exp\left({}^{-x}/_{\tau_3}\right) +C$$

where in the fitting procedure, $a_3 = (1 - a_1 - a_2)$

Table 2-4: Bi-exponential Fit for Total Anisotropy

System	a_1	τ_1	a_2	τ_2	C	R^2
MS-EVB	0.742	0.018	0.258	1.144	0.005	0.872
aMS-EVB	0.751	0.014	0.249	1.018	0.004	0.902
EDS-AIMD	0.798	0.022	0.202	1.470	-0.006	0.977

Table 2-5: Tri-exponential Fit for Total Anisotropy

System	a_1	τ_1	a_2	τ_2	a_3	τ_3	C	R^2
MS-EVB	0.649	0.012	0.243	0.365	0.116	2.492	0.001	0.882
aMS-EVB	0.660	0.010	0.230	0.322	0.111	2.253	0.001	0.913
EDS-AIMD	0.718	0.017	0.162	0.350	0.121	2.472	-0.009	0.984

B. Special-Pair Dance (No Hopping)

We fit the special-pair dance data to a bi-exponential curve as we expect the long-time, proton transfer process to be disregarded. When going from bi-exponential (Table 2-6) to tri-exponential (Table 2-7), the R^2 value on average increases by 0.012. Additionally, MS-EVB can be an approximate bi-exponential fit since the third amplitude is essentially 0.0, and aMS-EVB does not have any time constants longer than 1 ps, meaning the long-time scale is essentially removed from the anisotropy decay.

Table 2-6: Bi-exponential Fit for Special-Pair Dance

System	a_1	τ_1	a_2	τ_2	C	R^2
MS-EVB	0.680	0.028	0.319	0.286	0.059	0.383
aMS-EVB	0.696	0.028	0.304	0.304	0.052	0.362
EDS-AIMD						

Table 2-7: Tri-exponential Fit for Special-Pair Dance

System	a_1	τ_1	a_2	τ_2	a_3	τ_3	C	R^2
MS-EVB	0.641	0.035	0.289	0.311	0.070	0.00	0.059	0.389
aMS-EVB	0.492	0.018	0.357	0.102	0.151	0.503	0.050	0.380
EDS-AIMD								

C. Long-Lived Special Pair, No "Dance"

We fit the long-lived, special-pair data to a bi-exponential curve as we expect the short-time, special-pair dance to be disregarded When going from bi-exponential (Table 2-8) to tri-exponential (Table 2-9, the R^2 value either remained constant or decreased when going from the bi-exponential fit to the tri-exponential fit. This seems to suggest that a bi-exponential fit can capture the proper physics of the system. Additionally, MS-EVB is essential a bi-exponential fit since the first amplitude is close to 0, and the time constants are close to zero.

Table 2-8: Bi-exponential Fit for Long-Lived Special-Pair

System	a_1	τ_1	a_2	τ_2	C	R^2
MS-EVB	0.737	0.557	0.263	2.169	0.003	0.907
aMS-EVB	0.672	0.533	0.328	1.795	0.002	0.902
EDS-AIMD						

Table 2-9: Tri-exponential Fit for Long-Lived Special-Pair

System	a_1	τ_1	a_2	τ_2	a_3	τ_3	C	R^2
MS-EVB	0.052	0.000	0.786	0.682	0.162	2.889	0.001	0.907
aMS-EVB	0.043	0.004	0.885	0.955	0.072	0.001	0.006	0.900
EDS-AIMD								

Appendix B: NMA Comparison Between Different Cutoff Methods

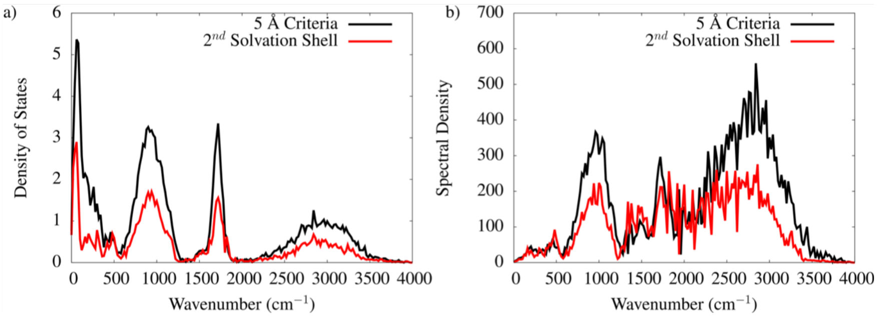

Figure 2-11: Density of States (a) and spectral density (b) from the INM analysis using the 5 Å cutoff and 2nd solvation shell cutoff.

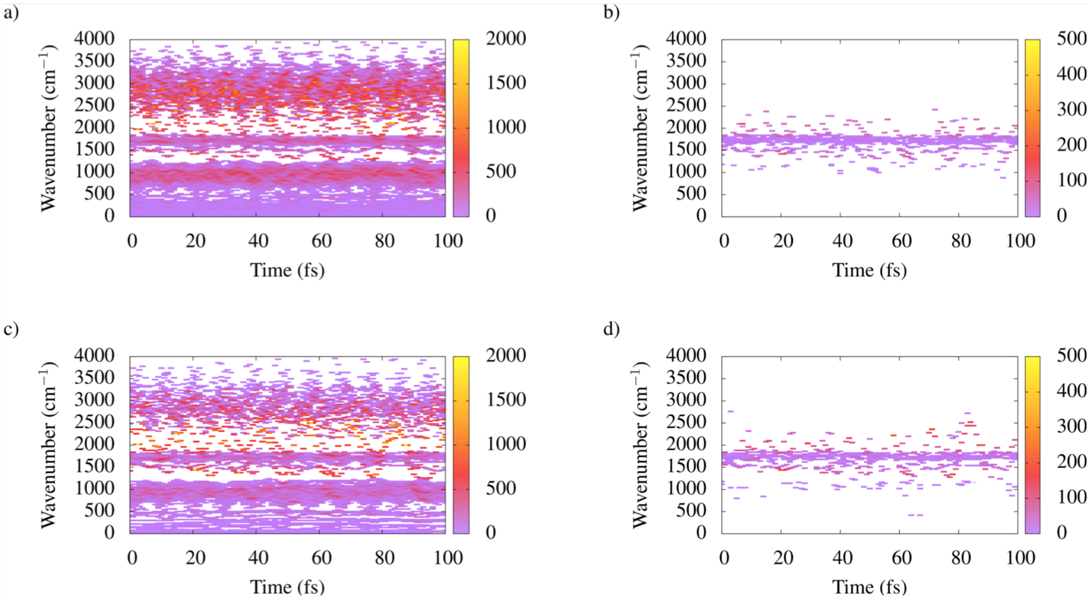

Figure 2-12: Spectral Density as a function of time for Eigen trajectories taken from MS-EVB 3.2 using the 5 Å cutoff (a & b) and 2nd solvation shell (c & d). Eigen trajectory is defined based on have 3 unique special-pair water molecules during the 100 fs segment. In Fig. (a) and (c) we show the total spectral density, while in Fig (b) and (d) we show the spectral density for H-O-H bends >5° in the special-pair.

Chapter 3: Molecular Origins of the Barriers to Proton Transport in Acidic Aqueous Solutions

This chapter is reprinted with permission from *J. Phys. Chem. B* 2020, 124, 40, 8868–8876.

Abstract

The self-consistent iterative multistate empirical valence bond (SCI-MS-EVB) method is used to analyze the structure, thermodynamics, and dynamics of hydrochloric acid solutions. The reorientation timescales of irreversible proton transport are elucidated by simulating 0.43 M, 0.85 M, 1.68 M, and 3.26 M HCl solutions at 270 K, 285 K, 300 K, 315 K, and 330 K. The results indicate increased counter-ion pairing with increasing concentration, which manifests itself via a reduced hydronium oxygen–chloride (O*-Cl) structuring in the radial distribution functions. Increasing ionic concentration also reduces the diffusion of the hydrated excess protons, principally by reducing the contribution of the Grotthuss proton hopping (shuttling) mechanism to the overall diffusion process. In agreement with prior experimental findings, a decrease in the activation energy of reorientation timescales was also observed, which is explicitly explained using activated rate theory and an energy-entropy decomposition of the state-averaged radial distribution functions. These results provide atomistic verification of suggestions from recent two-dimensional infrared spectroscopy experiments that chloride anions (as opposed to hydrated excess protons) create entropic barriers to proton transport.

I. Introduction

The hydrated excess proton (aka "hydronium" cation) has been the focus of research for well over two centuries, in part due to its intrinsically interesting nature,[68, 96] and in part due to it its varied applications for alternative energy,[5-7] enzymatic reactions,[8] and transmembrane proteins.[3, 9-11] Most ions diffuse through solution via vehicular diffusion; however, in bulk water the hydrated excess proton has a diffusion constant that is 4-5 times greater than other singly charged cations.[3-4] This phenomenon is commonly explained though the Grotthuss mechanism,[15, 97] where the identity of the excess proton rapidly changes by a hopping process of excess protons from one water molecule to another, thereby enabling large charge displacements in a shorter amount of time.

Any investigation of the dynamics of the hydrated excess proton necessitates a comprehensive understanding of its thermodynamically stable structures. The most common limiting proton solvation structures are those first defined by Zundel[18] and Eigen.[17] In terms of the former, the excess proton is equally solvated by two flanking waters that form an $H_5O_2^+$ structure. In the Eigen structure, however, the excess proton is strongly bound to one water molecule, resulting in a hydronium H_3O^+ core, which then creates three strong hydrogen bonds with the three neighboring water molecules, forming an $H_9O_4^+$ structure. However, the actual solvation structure of the hydrated excess proton likely exists in a dynamical superposition of configurations within these two limiting structures.

The literature is well represented with theoretical and computational work seeking to characterize the proton solvation structure and understand the mechanism of proton transport in water (see., e.g., refs[15, 46, 52, 54, 66, 68, 98]). Many theoretical studies indicate that the most stable structure has the excess proton most strongly bound to one water molecule. Even in simulation studies involving nuclear quantum effects, the excess proton's most stable structure suggests that it be bound to a single water molecule, indicating a preference for an Eigen cation.[46] Some simulation studies have proposed the Zundel cation to be the most stable structure in water;[51, 69-71] although an Eigen cation also shares aspects of this two-water picture when "distorted" (see below). By contrast, in earlier molecular dynamics studies with different methods, Tuckerman et al.[51-52] and Schmitt and Voth[46] reported that at most times a single water molecule was found to be closer to the central hydronium core, thereby forming an O*-O "special pair" with unique dynamical properties, where O* is the most hydronium-like oxygen atom. In a subsequent work, Markovitch et al.[20] described simulations that showed how the identity of the special-pair (out of three possible O*-H…O hydrogen bonds) can dynamically resonate around the central hydronium in a process they called the "special-pair dance." Additionally, they proposed that the solvation structure of the hydrated excess proton (on average) can be best characterized as a distorted Eigen cation in which one of the three O*-O distances of the three possible hydrogen bonds of the hydronium core with its first shell solvating water molecules is shorter. A number of studies have also detailed how irreversible proton transport occurs via the severing of a hydrogen bond in the 2nd solvation shell, thereby opening up a pathway for proton transport via Grotthuss shuttling.[15, 19, 46, 51-52, 99-100] Therefore, this process implies that proton transport occurs via a Zundel intermediate. thereby constituting an Eigen-Zundel-Eigen mechanism.[19-20]

Two dimensional infrared (2D IR) spectroscopic studies have proposed an increased population of Zundel configurations in solution through the use of vibrational assignments from gas-phase experiments.[21, 57-59] By exciting the O-H vibrations in red-shifted water molecules, strong correlations were observed with the flanking water bend in a Zundel-like configuration. One interpretation of this finding suggests that Zundel complex comprises the larger population of protonated species in solution rather than being an intermediate.[58] Subsequently, ultrafast broadband 2D IR spectroscopy was used to suggest that an intrinsically asymmetric (or distorted) Zundel complex was consistent with their findings.[21] The dynamics of the complex were accessed by calculating the anisotropy decay of the flanking water bend. These researchers suggested that the 2.5 ps timescale associated with the anisotropy decay of the hydrated proton bend is analogous to that for irreversible proton transfer between Zundel-like configurations, wherein the proton is shared by two flanking waters.[57] When considering the prior simulation studies noted earlier, it remains unclear whether the long-lived "distorted Zundel" cation proposed in these experiments is in essence the same as the "distorted Eigen" cation seen in the simulations and any real difference is simply a matter of semantics. This topic will be the focus of a forthcoming paper from our group.

The dynamics of flanking water bend were further investigated vis-à-vis its dependence on concentration and temperature. It was found that reorientation timescales slowed with a rise in chloride ion concentration, while showing no dependence on proton concentration.[59] Additionally, Arrhenius behavior was observed for the flanking water bend reorientation timescales, corresponding to an activation energy of 2.5 kcal/mol, 2.5 kcal/mol, and 1.5 kcal/mol for 1 M, 2 M, and 4 M HCl, respectively, even though the excess proton diffusion rate actually goes down with increasing acid concentration in both experiment and simulation. (It should be noted that at the highest acid dilution this activation energy result is very close to that predicted from the Multistate Empirical Valence Bond (MS-EVB) simulation model of ref. [19] and subsequent versions of that model.) This counterintuitive trend – that the activation energy decreases with an increase in the reorientation time scale – might be explained through the Eyring equation of transition state theory, $k \propto \exp\left(-\Delta F^{\dagger}/k_B T\right)$ where the activation free energy is written in the usual Gibbs form $\Delta F^{\dagger} = \Delta H^{\dagger} - T\Delta S^{\dagger}$, k_B is the Boltzmann constant, and T is the temperature. In the absence of a reliable correlation with transition-state structures, it has been argued that a decrease in transition state enthalpy $\Delta H^{\dagger}$ (here equivalent to the Arrhenius activation energy, E_a) could correlate with the decrease in the rate of proton transport if the transition state entropy of the system also decreased even more (so that $\Delta S^{\dagger}$ is more negative). However, since these reorientation timescales appeared to depend only on the chloride (or other counterion) concentration, it was thus proposed that chloride ions mostly contribute to the entropic barrier to proton transport.[59]

The structure and dynamics of concentrated hydrochloric acid solutions have been studied[101-102] using the Self-Consistent Iterative Multistate Empirical Valence Bond (SCI-MS-EVB) method.[50] In these studies, the hydronium oxygen–hydronium oxygen (O*-O*) radial distribution function (RDF) showed the formation of unusual contact ion pairs through the lone pairs of the hydronium cations due to the nonclassical delocalization of the protonic excess charge defect (the so-called center of excess charge, or CEC). Additionally, the concentration of HCl was shown to have a relatively small impact on the structures of the hydrated excess proton. By increasing the HCl concentration to 1.68 and 3.26 M in these simulation, standard (vehicular) diffusion and proton hopping (Grotthuss mechanism) of the hydrated excess protons decreased, with the hopping component decreasing the most. These studies indicate that, locally, the excess proton prefers to rattle between water molecules at higher acid concentrations, while globally decreasing effective proton hopping diffusion.

We have recently modeled (to be published) dilute hydrochloric acid solutions using both the MS-EVB 3.2 model[49] and experiment directed simulation *ab initio* molecular dynamics (EDS-AIMD).[43] This study was designed to understand the anisotropy of the special-pair unit vector and to correlate anisotropy timescales to physical reorientations found in molecular simulations. Simulation results indicate that the special-pair dance strongly decorrelates the anisotropy decay at a time constant of about 20 fs, which is much faster than earlier experimental data. By removing any effects from the special-pair dance on subsequent anisotropy calculations, we were able to correlate irreversible proton transport to an anisotropy decay of 2.5 ps, which is in excellent agreement with experimental data. The present study expands this work to concentrated acid solutions with the goal of clarifying the impact that chloride ions have on the thermodynamics, structure, and dynamics, of hydrochloric acid solutions.

This paper is structured as follows: In the next Methods section we outline the SCI-MS-EVB method used to carry out the acidic solution simulations and provide simulation details. Following that, in Results and Discussion section we provide results for state-averaged radial distribution functions (RDFs) to show how the solvation structure of the hydrated excess proton changes as a function of concentration. We also show dynamical properties via diffusion coefficients and anisotropy decays of the long-lived special-pair, which corresponds to irreversible proton transport. The energy-entropy decomposition of the O*-O* and O*-Cl state-averaged RDFs is also presented. Conclusions are then presented.

II. Methods

A. Simulation Methods

The MS-EVB method models the charge delocalization of hydrated excess protons by creating a state function, $|\Psi\rangle$, that is a linear combination of different bonding topologies, such that

$$|\Psi\rangle = \sum_i c_i |i\rangle \tag{3.1}$$

For a fixed nuclear configuration, each bonding topology, $|i\rangle$, indicates a different water molecule as having the excess proton covalently bound, and the eigen-vector coefficients, c_i, are determined by diagonalizing a quantum-like Hamiltonian. For its diagonal elements, the Hamiltonian employs classical force-fields to describe the bonded and non-bonded interactions for each bonding topology, plus a repulsive term between the O*-Ow, and off-diagonal elements to couple the different states. After diagonalizing the Hamiltonian, the ground-state eigenvector is used to calculate the forces with the Hellmann-Feynman theorem, which then propagate the system in time in an MD algorithm. Because obtaining a full-system Hamiltonian with multiple excess protons is too expensive to solve computationally, we applied the self-consistent field (SCI-MS-EVB) approach to the Hamiltonian for each hydrated excess proton, thus enabling the ground state energy for the whole system to be solved self-consistently, and water molecules belonging to multiple complexes were placed in the EVB complex with the highest probability after an initial ground state calculation.[50]

As indicated in the following analysis, we included the SCI-MS-EVB description of the delocalization of the excess proton charge defect in the structural, dynamical, and thermodynamic properties through state-average quantities. State-averaged (SA) radial distribution functions centered on the hydronium-like oxygen, $g_{SA}^{O^*-X}(r)$, are calculated using eq 3.2 below, where the c_i^2 is the probability of EVB state $|i\rangle$, and $g_i^{O^*-X}(r)$ is the RDF centered on the hydronium oxygen (O^*) and paired with either oxygen-water (O_W) or chloride (Cl) in state $|i\rangle$.

$$g_{SA}^{O^*-X}(r) = \sum_i c_i^2 g_i^{O^*-X}(r) \tag{3.2}$$

We extended the state-average RDF to O^*– O^* by including the probability of oxygens in other complexes having hydronium-like characteristics (Eq. 3.3).

$$g_{SA}^{O^*-O^*}(r) = \sum_i \sum_j c_i^2 c_j^2 g_{ij}^{O^*-O^*}(r) \tag{3.3}$$

Dynamically, we tracked the position of the center of excess charge ($\mathbf{r}_{\mathrm{CEC}}$) by calculating the state-averaged center of charge ($\mathbf{r}_{\mathrm{COC}}$) for each diabatic state using the ground state eigenvector such that

$$\boldsymbol{r}_{CEC} = \sum_{i} c_i^2 \boldsymbol{r}_{COC} \tag{3.4}$$

We calculated the thermodynamics of the hydrated excess proton complex via an energy-entropy decomposition of the potential of mean force, which we determined by inverting the state-averaged RDFs of eqs. 3.2 and 3.3 above.

B. Simulation Details

Concentrated HCl solutions of 0.43 M, 0.85 M, 1.68 M, and 3.26 M HCl were created by placing 2 HCl, 4 HCl, 8 HCl, and 16 HCl dissociated pairs in the simulation box with 256 water molecules. Each concentration was simulated at 270 K, 285 K, 300 K, 315 K, and 330 K, and 10 independent trajectories at each temperature and concentration were used for data collection. We did not account of covalent HCl molecules in our simulations as its molar concentration determined from its K_a value[103] would range from ~10^{-5} M to ~10^{-9} M depending on the H_3O^+ and Cl^- concentration and simulation temperature. Each trajectory used a timestep of 0.5 fs. All simulations used MS-EVB 3.2[49] to model HCl solutions, which used SPC-Fw[84] to model the water molecules and parameters from Dang[104] to model chloride ions. We note that it could be valuable to include polarization effects into the SCI-MS-EVB method as it has been shown to improve properties of point-charge models.[105-107] However, we point out that MS-EVB 3.2 has been shown to reproduce PMFs of AIMD simulations.[108] which incorporate polarizability. Additionally, the SCI-MS-EVB method already has certain polarization effects in the model due to the dynamic bonding topology and the delocalized proton charge defects inherent in the MS-EVB Hamiltonian.

After a classical potential equilibration period, simulations were equilibrated using SCI-MS-EVB in the constant NVT ensemble for 500 ps using the Nose-Hoover thermostat with a 100 fs time constant. Subsequent production runs were carried out in the constant NVE ensemble for 1 ns. All simulations were conducted using our in-house code of LAMMPS[83] with a radial cutoff of 9 Å; long-range interactions were calculated using the particle-particle, particle-mesh evaluator with a 10^{-5} convergence criteria.

III. Results and Discussion

A. State-Averaged Radial Distribution Functions

As seen in Figure 3-1, the radial distribution function of the Ow, O*, and Cl centered on the O* are shown to describe the structure around the hydronium core. As mentioned earlier, the solvation structure of the hydrated excess proton in simulations is best described by a distorted Eigen cation. In this depiction, a special-pair (or Zundel-like configuration) breaks the three-fold symmetry of an Eigen cation. As indicated in Figure 3-1a, the solvation structure of the hydronium core is minimally perturbed by the HCl concentration. By increasing the HCl concentration, the first peak increases slightly indicating enhanced structuring in the Eigen cation. Additionally, the solvation around the hydronium core remains largely unchanged with increases in HCl concentration, as determined by integrating the first peak of the O*-Ow RDF.

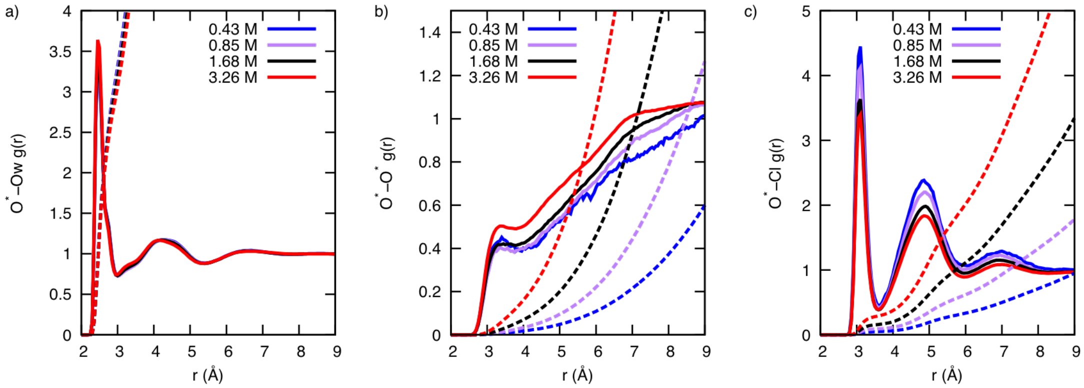

Figure 3-1: State Averaged Radial Distribution functions for (a) O*-Ow, (b) O*-O*, and (c) O*-Cl at 300K. Solid lines correspond to the RDFs, while the dashed lines represent the coordination number via integration of the RDFs.

In Figure 3-1b we show the RDF for O*-O* using SCI-MS-EVB 3.2. Prior SCI-MS-EVB 3.0 simulations of concentrated acids solutions have suggested a weak "amphiphilic" property of the hydrated excess proton.[101-102] Moreover, as the excess charge defect associated with the excess proton is delocalized across the solvating water molecules, a RDF peak was observed in the O*-O* RDF at 3.0 Å. The magnitude of this RDF peak was slightly less than 1, which represented a metastable structure between the cation-cation pairs. These cations interact through the lone-pair side of the hydronium cation with the excess proton CECs of the two complexes being separated by an additional Angstrom beyond the O*-O* distance to mitigate the repulsive interactions.[101-102] The O*-O* peak shown in Figure 3-1b is less structured than in our previous EVB model, with a RDF intensity of ~0.4. The MS-EVB 3.2 model includes an additional attractive interaction between the water-hydrogen and hydronium-oxygen to better model the presolvation effects found in AIMD simulations that help facilitate proton transfer.[33, 49] This additional term helps to transiently place water molecules in the hydronium lone-pair regions, thereby explaining the reduced structuring observed in the O*-O* RDF for the MS-EVB 3.2 model.

Figure 3-1c illustrates the O*-Cl RDF for the concentrations studied here. At 3.0 Å, ion pairing with the chloride counterion could be observed at a somewhat closer distance compared to our previous MS-EVB models,[101-102] which is in agreement with AIMD simulation results.[109] Although the first peak is positioned adjacent to the first solvation shell of water around the hydronium, it does not correspond to a completely solvent-separated ion pair. Rather, a chloride ion found 3.0 Å from the central hydronium disrupts the coordination number of the hydronium core.

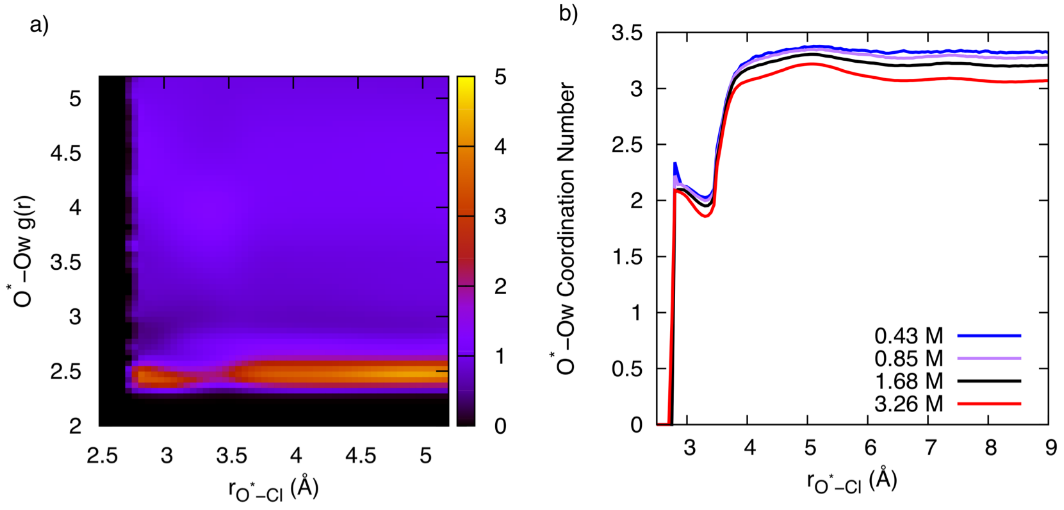

Figure 3-2: (a) Conditional O*-Ow RDF as a function of O*-Cl distance for 3.26 M HCl Solution at 300 K. (b) Integrating the first peak of the O*-Ow RDFs (O*-Ow distance of 2.9 Å for O*-Cl distances less than 3.5 Å and 3.0 Å for O*-Cl distance greater than or equal to 3.5 Å) shows the Ow coordination number around a hydronium corresponding to a given O*-Cl distance.

Figure 3-2a depicts the conditional O*-Ow RDF as a function of O*-Cl distance for the 3.26 M HCl simulation at 300 K. The first peak in the O*-Ow RDF indicates a clear distinction between a chloride ion less than or greater than 3.5 Å. The peaks less than 3.5 Å have a weaker intensity and are found to be closer to the central hydronium than at longer distances. Specifically, the peak intensity observed at less than 3.5 Å indicates that the chloride ion is closer to the central hydronium. Integrating the first peak of these RDFs (Figure 3-2b) results in an Ow coordination number close to 2.0 when the chloride distance is less than 3.5 Å away, but increases to 3.0 in the case of larger chloride distances. This finding indicates that at short distances the chloride disrupts the full solvation of the central hydronium and displaces one of the water molecules of the distorted Eigen cation.

Of particular interest is the reduced intensity of the O*-Cl RDF peaks with increases in HCl concentration, as illustrated in Figure 3-1c. This finding seems counterintuitive to what one might expect with increasing counterion concentrations, especially in light of the fact the intensity of the O*-Ow and O*-O* RDFs showed only a small uptick with increasing concentration. However, although the O*-Cl RDF intensity decreased, the coordination number of the O*-Cl contact ion pairing increased markedly from 0.01 to 0.3 with rising concentration. This 30-fold increase in contact-ion pairing served to further reduce the presence of water molecules around the central hydronium core, thus lowering the possible number of proton transport pathways via Grotthuss shuttling. Therefore, increasing the ionic concentration decreases the availability of water molecules needed for the proton hopping transport, which translates into a decrease in entropy and thus an increasing entropic barrier in the transition state picture. In turn, this increases the activation free energy of the system through the entropy of activation but not the enthalpy of activation (equivalent to the Arrhenius activation energy). This feature will be further examined in the following subsections.

B. Proton Diffusion

We next examined the dynamics of the hydrated excess proton in the various HCl solutions by studying the diffusion coefficient of the center-of-excess charge (CEC) and the most hydronium-like oxygen (Figure 3-3) at 300 K. The diffusion coefficient was calculated from the linear region of the mean squared displacement (MSD) via the usual Einstein relationship.

$$D = \lim_{t\to\infty} \frac{\langle \left(r(t) - r(0)\right)^2 \rangle}{6t} \tag{3.5}$$

In the most dilute concentration (0.43 M), the diffusion coefficients of the CEC (purple) and most hydronium-like oxygen (red) was determined to be 0.35 Å^2/ps, which is within the statistical uncertainty of the value for a single proton in 256 waters in the MS-EVB 3.2 model.[49] As the HCl concentration increased in Fig. 3-3, the diffusion coefficient of the CEC and the most hydronium-like oxygen decreased, which, as noted earlier, can be attributed to the influence of chloride ions and to a lesser degree the other excess protons blocking potential proton hopping transport pathways.

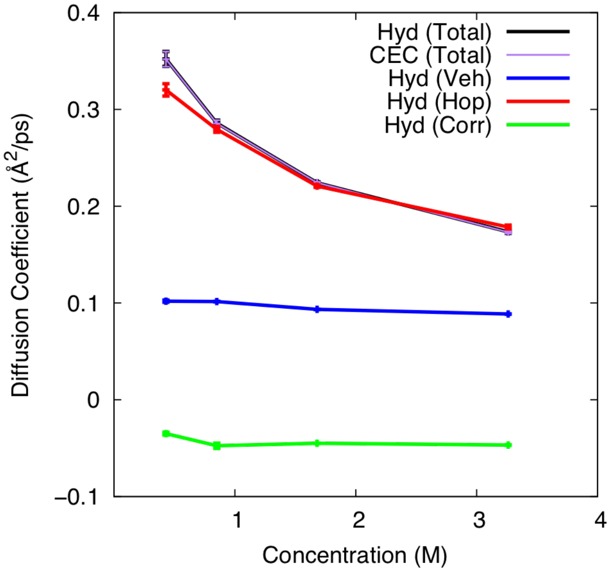

Figure 3-3: Diffusion coefficients for the hydronium (black) and center-of-excess charge (CEC) determined from the linear region of the mean-squared displacement according to eq 3-5. The MSD of the hydronium is further decomposed based on vehicular (blue) and hopping (red) mechanisms, in addition to the correlation (green) between the two diffusion mechanisms.

We further analyzed the MSD of the most hydronium-like oxygen by decomposing it into its vehicular and Grotthuss hopping components to understand how they contribute to overall diffusion. By expanding the total displacement vector, $\boldsymbol{r}_{Tot}$, as the sum of the vehicular displacement vector (standard diffusion without hopping), $\boldsymbol{r}_{Veh}$, and Grotthuss hopping displacement vector, $\boldsymbol{r}_{Hop}$, (eq 3.6 below), the mean squared displacement can be determined according to eq 3.7 as[102]

$$\Delta \boldsymbol{r}_{Tot}(t) = \boldsymbol{r}_{Veh}(t) + \boldsymbol{r}_{Hop}(t) \tag{3.6}$$

$$\langle \Delta \boldsymbol{r}_{Tot}(t)^2 \rangle = \langle \Delta \boldsymbol{r}_{Veh}(t)^2 \rangle + \langle \Delta \boldsymbol{r}_{Hop}(t)^2 \rangle + 2\langle \Delta \boldsymbol{r}_{Veh}(t) \cdot \Delta \boldsymbol{r}_{Hop}(t) \rangle \tag{3.7}$$

In eq. 3.7, the first and second term on the right hand side correspond to the MSD of the vehicular and hopping components, respectively, while the last term indicates the contribution to the MSD that results from correlating the two processes (which may have a negative value if there is some degree of anti-correlation).

In our simulations, the total displacement vector of the most hydronium-like oxygen was broken down into 100 fs time segments. If the identity of the most hydronium-like oxygen changed during those 100 fs, the displacement was added to $\boldsymbol{r}_{Hop}$; otherwise, the displacement was added to $\boldsymbol{r}_{Veh}$. We then calculated the MSD for each process; the MSD for the correlation, $\langle \Delta\boldsymbol{r}_{Veh}(t) \cdot \Delta\boldsymbol{r}_{Hop}(t) \rangle$, was determined by algebraically manipulating eq. 3.7 and using the MSD for the total, vehicular, and hopping processes. The diffusion coefficients can then be calculated using the Einstein relationship (eq 3.5) and expressed as

$$D_{Tot} = D_{Veh} + D_{Hop} + 2D_{Corr} \tag{3.8}$$

In Figure 3-3 we present the diffusion coefficients for vehicular transport (blue) and proton hopping (red), with the correlation between these two diffusion mechanisms (green). As the ionic concentration increases, vehicular diffusion and the correlation between the hopping and vehicular components decreases only slightly. In contrast, the diffusion coefficient for Grotthuss hopping decreases precipitously, similar to the total displacement. In fact, the diffusion coefficient of the Grotthuss hopping mechanism represents the largest component of total diffusion, with values comparable to those for total displacement. Diffusion due to hopping decreases when ionic crowding in the system disrupts the water structure and decreases the number of proton transport pathways. This decreased hopping does not mean that the hydrated excess proton lingers on a single water molecule. The average number of total hopping events per picosecond were found to be 10.8 ± 0.4 for 0.43 M, 10.9 ± 0.4 for 0.85 M, 11.1 ± 0.4 for 1.68 M, and 11.3 ± 0.5 for 3.44 M. The similar number of hopping events as a function of concentration (at least within a standard deviation) points to the fact that protons do not remain on the same water molecule; rather, the hydrated excess proton shuttles back and forth between water molecules but the hopping events that lead to diffusion and proton charge translocation diminish with increasing concentration

C. O*-Ow Long-Lived Anisotropy

Defining the special-pair as the O*-Ow pair that minimizes $\delta = \left|\boldsymbol{r}_{O^{*}H} - \boldsymbol{r}_{O^{SP}H}\right|$ around the central hydronium, the O-O unit vector of the special-pair was constructed and used to calculate the anisotropy decay according to eq 3.9, where $P_2(t)$ is the 2nd Legendre polynomial, such that

$$C_2(t)= \frac{\langle P_2(\hat{u}(t)\hat{u}(0))\rangle}{\langle P_2(\hat{u}(0)\hat{u}(0))\rangle}. \tag{3.9}$$

The anisotropy decay behavior for the total simulation, special-pair dance, and long-lived special-pairs can be determined and used to determine appropriate time constants to physical reorientations in the hydrated proton complex. The long-lived special-pair removes the fast reorientation due to the special-pair dance that is unable to be captured in experiments and is the unit vector centered on the hydronium pointing to the water molecule that would accept the excess proton at the next proton transfer event. Our soon to be published work will show that this quantity is able to correlate experimental time constants to irreversible proton transfer.

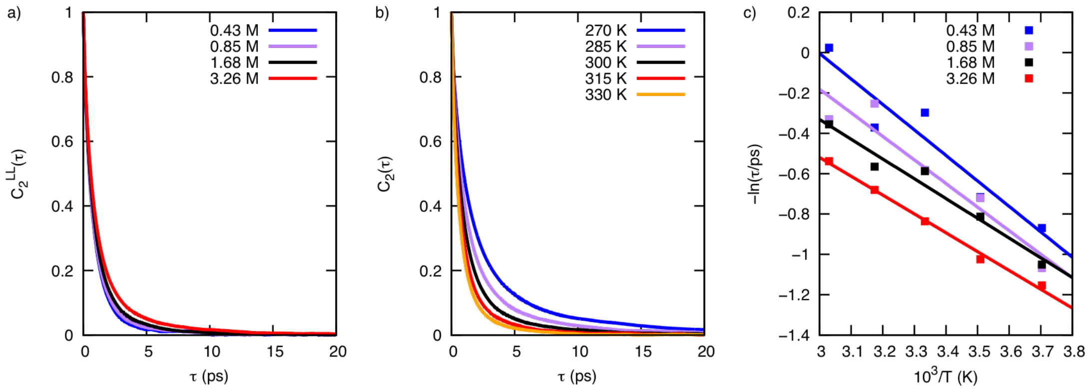

Figure 3-4: Long-lived special-pair anisotropy curves as a function of (a) concentration at 300 K and (b) temperature in 3.26 M HCl solution. The time-constant corresponding to irreversible proton transport was then extracted from a bi-exponential fit and used to create an Arrhenius plot in panel (c).

We applied this analysis to the concentrated acid solutions, focusing on long-lived special-pair anisotropy decay. Figure 3-4a illustrates the long-lived anisotropy decays for 0.42, 0.85, 1.68, and 3.26 M HCl at 300 K. Fitting these anisotropy decays with a biexponential best fit gave an R^2 value of 0.999 for all concentrations. Anisotropy decay data for all concentrations and temperatures can be found in Appendix A, Figure 3-6. By examining the long time constant of these fits, a corresponding increase in time constant was seen with increasing concentration, which was also seen experimentally.[59] Note that these time constants are somewhat smaller than those obtained experimentally; however, they still approximate the 1.5 ps proton transport rate obtained in NMR studies.[15, 56] We attribute the discrepancy from the values at high dilution from the MS-EVB algorithm to differences with the SCI-MS-EVB method implemented here and the possibility that the experiments mix in other motions.

Table 3-1: Pre-exponential Parameter and Activation Energy (kcal/mol) fitted from Arrhenius Plots

Conc (M)	Ln(A)	$\boldsymbol{E_a}$ (kcal/mol)	$\boldsymbol{E_a}$ std. deviation (kcal/mol)
0.43	3.78	2.5	0.5
0.85	3.32	2.3	0.4
1.68	2.60	1.9	0.2
3.26	2.28	1.9	0.1

Figure 3-4c provides Arrhenius plots in accordance with the Arrhenius equation (eq. 3.10) presenting the long-lived time constants of these concentrations between 270-300 K (see Figure 3-4b for the corresponding anisotropy at 3.26 M).

$$\tau^{-1} = A\, e^{-E_a/k_B T} \tag{3.10}$$

The slopes of the Arrhenius plots in Figure 3-4c correspond to activation energies of 2.5 $\pm$ 0.5, 2.3 $\pm$ 0.4, 1.9 $\pm$ 0.2, and 1.9 $\pm$ 0.1 kcal/mol at concentrations of 0.43, 0.85, 1.68, and 3.44 M, respectively (Table 3-1), which indicate a monotonic decrease in both activation energy and pre-exponential parameter with increases in both concentration. Qualitatively, the decrease in activation energy certainly agrees with experimental results. It must be noted, however, that those experimental results suggest a non-monotonic trend in that the anisotropy for 1 M, 2 M, and 4 M that corresponded to activation energies of 2.5 kcal/mol, 2.5 kcal/mol, and 1.5 kcal/mol, respectively. We attribute these qualitative discrepancies to the delocalized vibrational modes at 1750 cm^{-1} frequency,[77-78] which contribute to the reorientation of the transition dipole moment and are less well captured in the long-lived unit vector used in the simulations. Nevertheless, the semi-quantitative agreement between the simulated trends and the experimental findings for these time constant values is encouraging, even when using just the simple long-lived special-pair unit vector.

The increased reorientation timescales, coupled with a corresponding decrease in activation energy, would appear to be counterintuitive. As noted earlier, the experimentalists have attempted to explain this apparent contradiction by connecting the Arrhenius equation (eq 3.10) with an Eyring equation from transition state theory (eq 3.11 below) without having to provide a detailed molecular picture of the transition state.[59] The activation energy in eq 3.10 corresponds to the activation enthalpy in eq 3.11 (a positive number), while the Arrhenius prefactor will encompass both the k_0 and activation entropy contributions (the latter being usually negative), such that

$$\tau^{-1} = k_0 e^{\Delta S^\dagger / k_B} e^{-\Delta H^\dagger / k_B T} \tag{3.11}$$

Using the Eyring equation, a decrease in the activation enthalpy could only correspond to an increase in the time constant with concentration (i.e., a decrease in the left side of eq 3.11) when there is an over-competing decrease in the transition state entropy so that $\Delta S^\dagger$ becomes more negative in value. A linear trend in the ln(A) and E_a, both experimentally and in simulations, further corroborates competing factors between the energy and entropy terms (see Appendix A, Figure 3-7), suggesting that increasing the ionic concentration decreases both the activation energy and entropy of the system.

D. Energy-Entropy Decomposition

Up to this point, we have seen that increasing the HCl concentration lowers the activation energy and entropy of the system in terms of the proton transport. It is important to also understand how additional excess protons and chlorides can contribute to this reduction, which can be quantified by examining the pairwise, reversible work between O*-O* and O*-Cl pairs, i.e, the potential of mean force, or PMF, from the RDFs as determined by the reversible work theorem.[110]

Note that we did not consider the O*-Ow energy-entropy decomposition as this RDF remained largely independent of concentration.

From the state-average RDFs in Figure 3-1, the free energy profile of the system was calculated via the reversible work theorem (eq. 3.12). The additional $4\pi r^2$ was included to accurately account for the configurational entropy and to covert the PMF into a free energy such that

$$F(r,T) = -k_B T \ln 4\pi r^2 g(r) + C \tag{3.12}$$

In eq. 3.12, C is defined so that the free energy minimum was set to 0.0 kcal/mol. These PMF plots can be found in the Appendix B, Figures 3-8 through 3-12. Then, using the radial distances from the five simulation temperatures, both energy and entropy were decomposed according to eq. 3.13,

$$\Delta F(r,T) = \Delta U - T\Delta S = y + xm \tag{3.13}$$

where the energy and entropy were determined from the y-intercept and slope of a linear best fit line, respectively. It should be noted that since the simulations were sampling from the constant NVT canonical ensemble, it is more correct here to use the Helmholtz free energy *F* rather than Gibbs free energy G, and thus the internal energy *U* rather than the enthalpy *H.*

Figure 3-5 provides energy (top figures) and entropy (bottom figures) curves for the O*-O* and O*-Cl pairs. Due to limited sampling in the 0.43 and 0.85 M solutions, the energy and entropy curves have some noise. Note that the energy and entropy curves for the O*-O* pairs (3-5a and 3-5c, respectively) appear to be very similar across all studied concentrations. The O*-O* energy displayed a Lennard-Jones potential-like behavior with a well depth slightly less than k_BT, which explains the unusual O*-O* pairing that occurs via the hydronium lone-pair side interactions observed in previous MS-EVB simulations.[101-102] The near-identical energy and entropy curves for the O*-O* pairs confirm their negligible effects on decreasing the activation entropy of the system, which is in good agreement with recent experimental findings.[59]

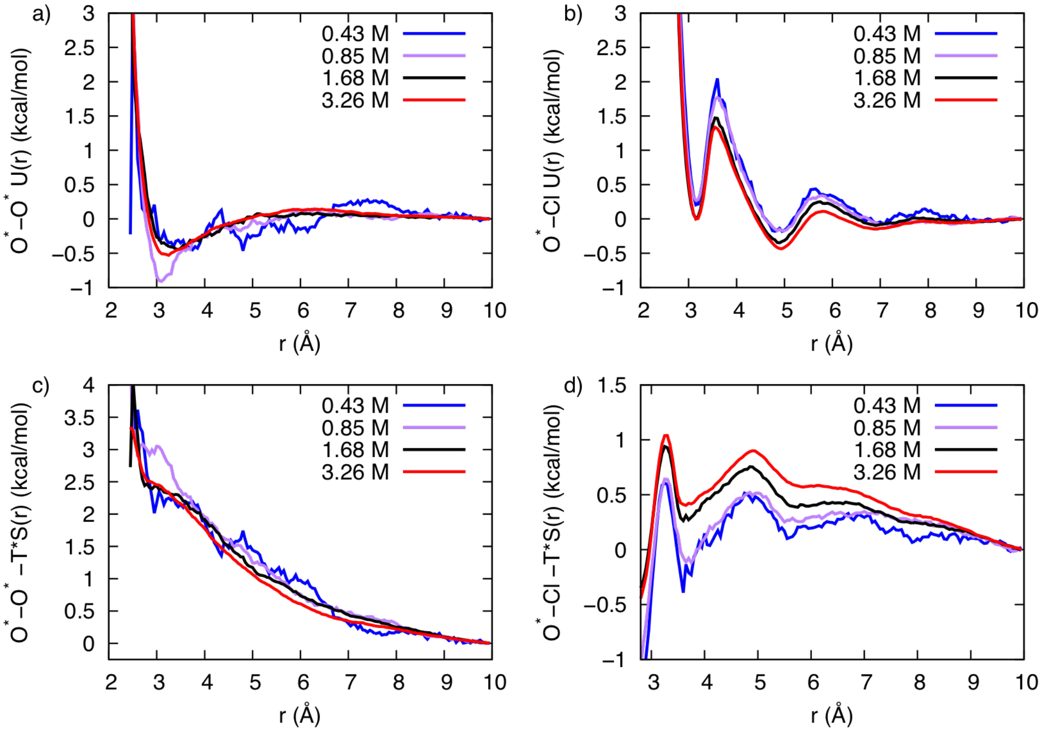

Figure 3-5: Energy-Entropy decomposition using eq 3.13 determined from the free-energy using eq 3.12 with the state-averaged RDFs. In (a) & (b) the energy term is shown for the O*-O* and O*-Cl pair, respectively. In (c) and (d) the entropy term at 300 K is shown for the O*-O* and O*-Cl pairs, respectively. Note that in the latter $-TS(r)$ is plotted so a decreased (more negative) entropy manifests as an increase in the curve.

In contrast, the O*-Cl pairing (Figures 3-5b and 3-5d) are quite dependent on concentration. In Figure 3-5b, we see two energy wells corresponding to the two O*-Cl solvation shells, where the second solvation shell is energetically more favored. Of key importance is the decrease in the O*-Cl energy with an increase in HCl concentration, especially between the 1st well and transition state. This energy is strongly correlated to activation energy, further corroborating the counterintuitive decrease in activation energy with increases in concentration. Additionally, we see a rise in the O*-Cl $-T\Delta S$ plots as the HCl concentration increases, with a corresponding decrease in the O*-Cl entropy. This finding further supports the competing terms in the Eyring equation.

Figure 3-5 also shows that the entropy around the hydrated proton complex does indeed decrease due to the increased chloride concentration, and not as a result of the O*-O* interactions. Note that in the latter $-TS(r)$ is plotted so a decreased (more negative) entropy manifests as an increase in the curve. These observations further support both the computational and experimental findings that an increase in reorientation timescale corresponds to a decrease in activation energy but with a larger decrease in transition state entropy (i.e., increase in the negative activation entropy).

IV. Conclusions

In this work, concentrated HCl acid solutions (0.43 M, 0.85 M, 1.68 M, and 3.26 M) have been simulated using the SCI-MS-EVB 3.2 model to better understand the thermodynamics, structure, and dynamics of hydrated excess protons in these aqueous solutions. The results show some weak amphiphilic-like association between hydrated proton complexes, but more importantly they also confirmed an increase in counter-ion pairs with increasing HCl concentration. These ion pairs further disrupt the hydration around the central hydronium-like structure, decreasing entropic freedom. Increasing the ionic concentration lowers the diffusion of the hydrated excess protons by significantly reducing their Grotthuss hopping. An experimental manifestation of this molecular-scale behavior was confirmed to be an increase in the reorientation timescale associated with irreversible proton transfer. It was also observed that, counterintuitively, the activation energy for irreversible proton transport decreases with the increasing acid concentration and reorientation timescales. However, the activation entropy also decreases to more than compensate for the dropping activation energy. These results can be interpreted using the Eyring transition state theory-like equation and an energy-entropy decomposition of the ion pair PMFs to confirm that the decreased activation energy stems from a decrease in average energy between the O*-Cl pairs but also a decrease in their entropy due to the blocking of Grotthuss shuttling pathways.

The best available data to date still point to the concept that proton transport (including Grotthuss shuttling) is inherently a collective hydrogen-bonding rearrangement process involving 20 or more water molecules surrounding a central hydronium- like core in the form of a distorted Eigen cation (see ref [19] for the first published characterization and discussion of this behavior). In that process, proton transport occurs via solvent rearrangement within the second solvation shell and beyond which is on the order of 1−2 ps, and at the same time, the central hydronium-like core is dynamically switching special- pairs within a distorted Eigen cation until an irreversible proton transport process occurs.[20] We note that the role of solvent fluctuations on the proton transfer away from the inner hydronium-like core has been recently studied by Roy *et. al,*[94] who used two-dimensional transition state theory (TST) and Marcus theory to analyze the proton transfer process between two water molecules in the inner core; their findings also show the distorted Eigen cation as the thermodynamically most stable structure of the hydrated excess proton. Rate constants for this inner core proton transfer event as obtained from TST and Marcus theory were shown to decrease with increasing HCl concentration, in addition to an increased lifetime of the Zundel cation, consistent with an Eigen−Zundel−Eigen proton transfer process.[20] Roy et al., however, did not provide a connection with experimental Arrhenius plots or information about the source of the reduced proton transfer rate via an energy–entropy decomposition of the kinetic barrier, as proposed by recent experiments[59] and further supported and analyzed in the present work. In the present paper, the reduced proton transport rate (and increased experimental anisotropy time constant) is seen to be an effect of chloride ions disrupting the larger water solvation structure around the hydronium-like core, which reduces the number of water molecules available for proton transport from the distorted Eigen cation, thus reducing the number of proton transport pathways and creating an entropic barrier to the overall proton transport.

Appendix A: Biexponential Fits to the Long-Lived Special-Pair Anisotropy Curves

$$f(x)= a_1\cdot \exp\left({}^{-x}/_{\tau_1}\right) + a_2\cdot \exp\left({}^{-x}/_{\tau_2}\right) +C$$

where in the fitting procedure, $a_2 = (1 - a_1)$.

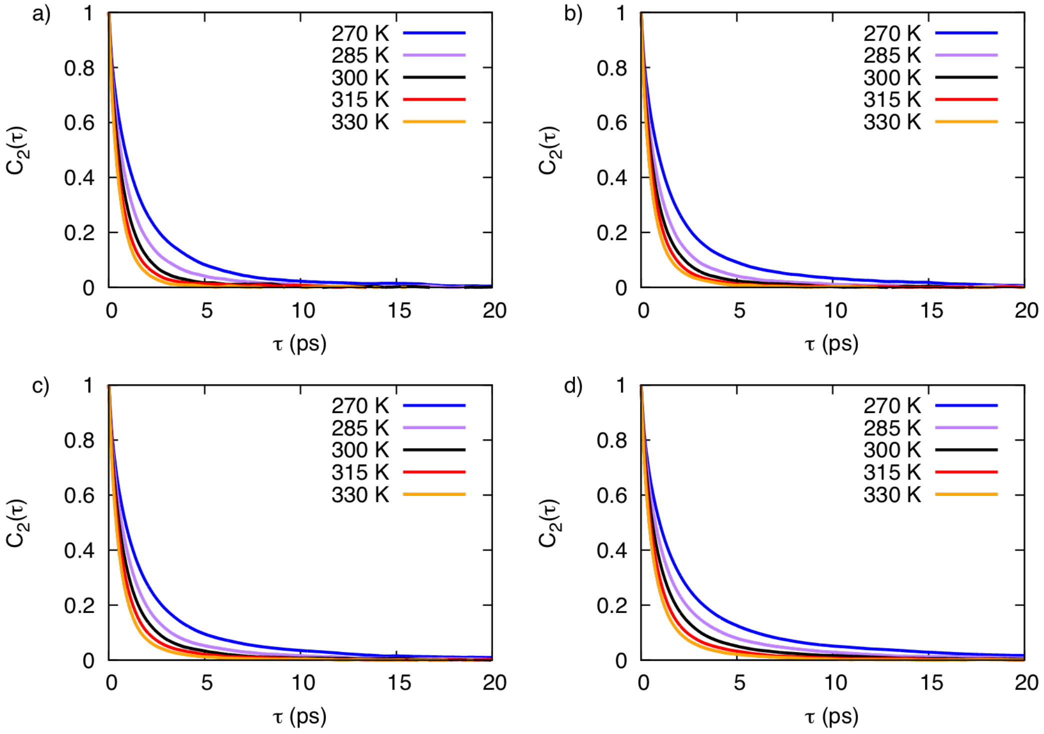

Figure 3-6: Anisotropy plots for the O*-Ow Long-Lived unit vector for (a) 0.43 M HCl, (b) 0.85 M HCl, (c) 1.68 M HCl, and (d) 3.26 M HCl.

Table 3-2: Bi-exponential Fit for 0.43 M Long Lived

Temp (K)	a_1	τ_1 (ps)	a_2	τ_2 (ps)	C	R^2
270	0.414	0.471	0.586	2.385	0.0109	0.9996
285	0.579	0.527	0.421	2.047	0.0039	0.9997
300	0.534	0.427	0.466	1.347	0.0034	0.9996
315	0.731	0.447	0.269	1.451	0.0013	0.9993
330	0.619	0.369	0.381	0.977	0.0001	0.9998

Table 3-3: Bi-exponential Fit for 0.85 M Long Lived

Temp (K)	a_1	τ_1 (ps)	a_2	τ_2 (ps)	C	R^2
270	0.543	0.628	0.457	2.907	0.0131	0.9992
285	0.599	0.533	0.401	2.056	0.0058	0.9996
300	0.662	0.495	0.338	1.789	0.0016	0.9996
315	0.604	0.415	0.396	1.288	0.0027	0.9998
330	0.742	0.413	0.258	1.393	0.0006	0.9999

Table 3-4: Bi-exponential Fit for 1.68 M Long Lived

Temp (K)	a_1	τ_1 (ps)	a_2	τ_2 (ps)	C	R^2
270	0.506	0.572	0.494	2.860	0.0136	0.9993
285	0.585	0.560	0.415	2.256	0.0072	0.9995
300	0.597	0.476	0.403	1.800	0.0046	0.9997
315	0.710	0.475	0.290	1.761	0.0025	0.9997
330	0.714	0.414	0.286	1.427	0.0017	0.9998

Table 3-5: Bi-exponential Fit for 3.26 M Long Lived

Temp (K)	a_1	τ_1 (ps)	a_2	τ_2 (ps)	C	R^2
270	0.485	0.552	0.515	3.171	0.0232	0.9991
285	0.573	0.563	0.427	2.785	0.0121	0.9994
300	0.619	0.517	0.381	2.307	0.0072	0.9995
315	0.675	0.477	0.325	1.976	0.0042	0.9997
330	0.693	0.430	0.307	1.713	0.0023	0.9997

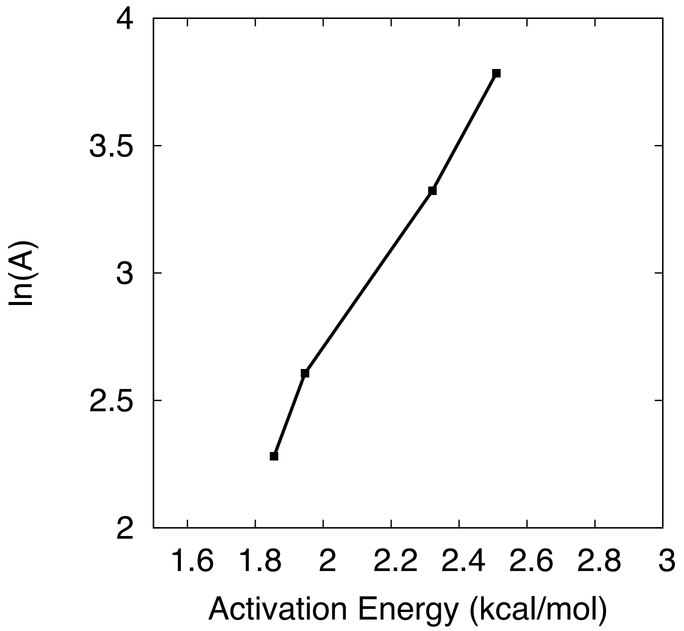

Figure 3-7: Ln(A) vs. Ea obtained from Arrhenius plots for the 4 HCl Concentrations studied here.

Appendix B: Potential of Mean Force as a Function of Concentration and Temperature

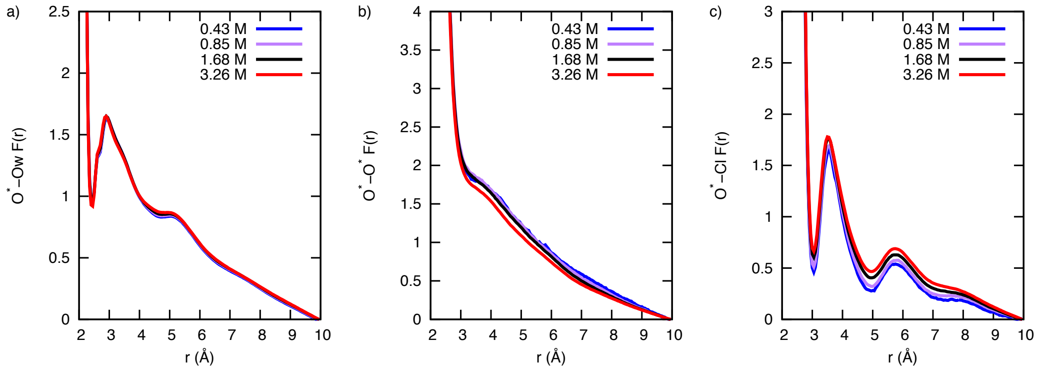

Figure 3-8: Potential of Mean Force for (a) O*-Ow, (b) O*-O*, and (c) O*-Cl at 300 K. These calculations are calculated using eq. 3.12 in the main text.

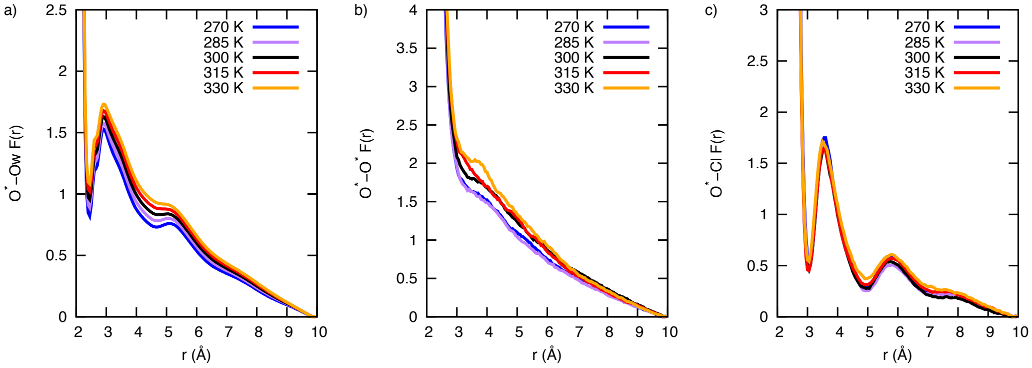

Figure 3-9: Potential of Mean Force for (a) O*-Ow, (b) O*-O*, and (c) O*-Cl for 0.43 M solution. These calculations are calculated using eq. 3.12 in the main text.

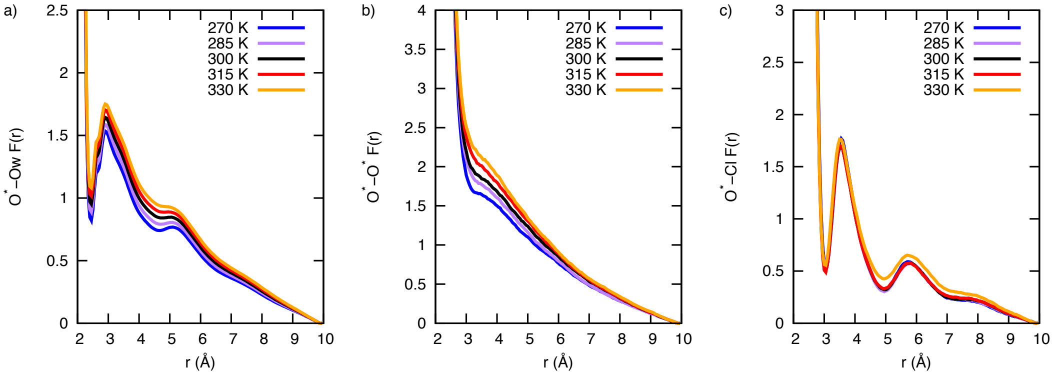

Figure 3-10: Potential of Mean Force for (a) O*-Ow, (b) O*-O*, and (c) O*-Cl for 0.85 M solution. These calculations are calculated using eq. 3.12 in the main text.

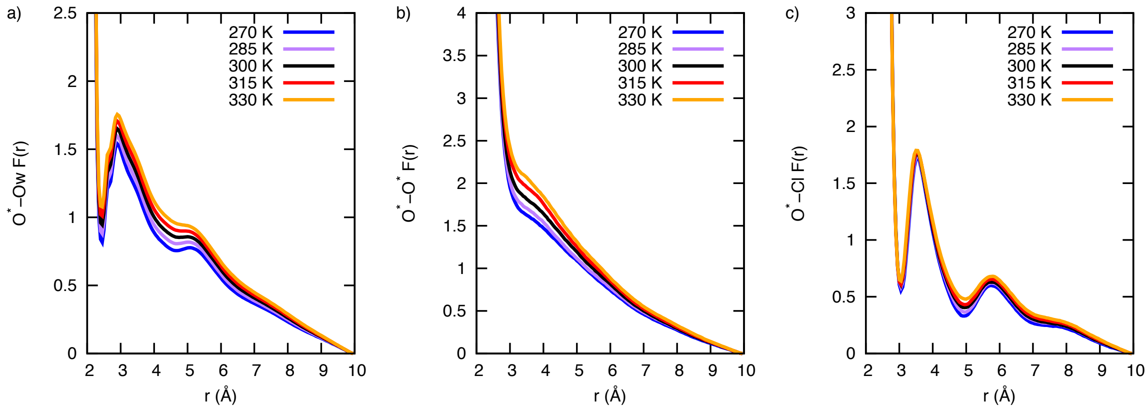

Figure 3-11: Potential of Mean Force for (a) O*-Ow, (b) O*-O*, and (c) O*-Cl for 1.68 M solution. These calculations are calculated using eq. 3.12 in the main text.

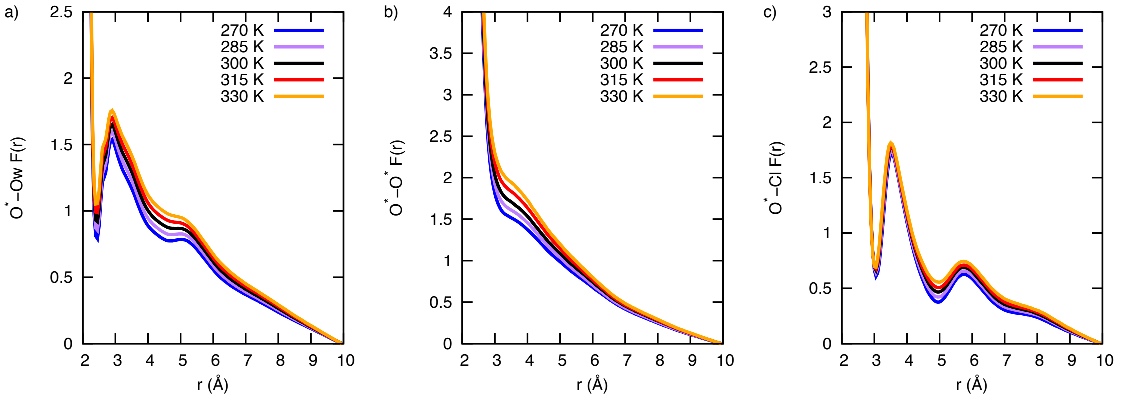

Figure 3-12: Potential of Mean Force for (a) O*-Ow, (b) O*-O*, and (c) O*-Cl for 3.44 M solution. These calculations are calculated using eq. 3.12 in the main text.

Chapter 4: Proton Transport in Perfluorosulfonic Acid Membranes Under External Electric fields

Abstract

It has been shown that electrolytic solutions separating ultrathin electrodes are known to exhibit enhanced mobility (Coulomb transport) due to the potential difference that arises between the electrodes. An enhanced understanding of Coulomb transport in bulk Nafion is crucial for applications in proton exchange membrane fuel cells. In this study we examined the effects of varied electric field strengths on bulk systems of the Nafion perfluorosulfonic acid (PFSA) membrane at various hydration levels and temperatures. Previous reactive molecular dynamics simulations of PFSA membranes have shown that the excess protons are shuttled through the hydrophilic pore via the assistance of the sulfonic pendent side chain, while also experiencing persistent caging effects of the hydrated excess proton in the water channel. Our results indicate that the PFSA proton hopping mechanism along sulfonate groups is present in systems under applied voltage, as shown via minimal perturbation between the side chain and the excess proton. Additionally, we observed that electric fields enhance transport properties and reduce the caging effects of the hydrated excess proton, which shows the presence of Coulomb transport in bulk Nafion PEM membranes.

I. Introduction

There is little doubt that mitigating the myriad effects of climate change will require a dramatic transformation of the global energy system, which in large part will be driven by the development and use of renewal energy sources for automotive and portable applications. One such approach involves the use of proton exchange membrane fuel cells (PEMFCs). Because PEMFCs rely on hydrogen gas as a fuel source and generate water as the only byproduct,[111] they represent a clean and efficient contribution to power generation for the twenty-first century. In an operating PEMFC, the functionality of the polymer membrane is critical in separating the cathode from the anode and shuttling protons produced by oxidizing hydrogen gas at the anode to the cathode. For many years the prevailing membrane for use in fuel cells has been the perfluorosulfonic acid (PFSA) membrane Nafion[12] due to its high proton conductivity and extreme stability. Upon hydration, the polymer membrane swells and creates a hydrophobic/hydrophilic phase separation, where the perfluoronated carbon backbone constitutes the hydrophobic region, and the water and sulfur pendant side chains form a hydrophilic region that facilitates proton transport.[12-13]

Molecular dynamics simulations are helpful for elucidating essential proton transport mechanisms in PFSA membranes. Simulation methods that model the hydrated excess proton in PFSA membranes must be able to account for normal vehicular diffusion and the bond rearrangement found in the Grotthus mechanism.[15, 65] Although many classical simulation studies have been used to investigate proton transport in PFSA membranes system (e.g. Ref [112-115]), they cannot account for the Grotthus Mechanism. Additionally, *ab initio* molecular dynamics (AIMD) simulations of PFSA,[116-119] although powerful, cannot establish the relevant time and length scale information needed to determine proton transport in PFSA systems. In contrast, the multistate empirical valence bond method[45-49] (MS-EVB) is capable of accessing this time and length scale information, and thus is effective for describing proton transport in PFSA systems.[6-7, 120-126]

Reactive MS-EVB simulations have confirmed that proton transport in PFSA membranes is assisted by the presence of sulfonate groups.[6-7] Specifically, repulsive interaction parameters between the hydronium and sulfonate groups result in only a negligible impact on the dynamics of the hydrated excess proton. This finding would appear to be counter-intuitive as it has also been documented that protons located further away from the interface and in more bulk-like regions of the hydrophilic pore would feature enhanced transport properties.[127-128] However, it was observed that an excess proton always resides within two solvation shells of a sulfonate group, and never found in bulk-like water, which accounts for the minimal change in dynamics. Prior research also indicates that the increased flexibility of the pendant side chains is correlated to larger proton diffusion.[6] These studies denote that protons shuttle through the hydrophilic pore by hopping from one sulfonate group to another due to the overlap in potential energy wells of the neighboring sulfonate groups. A follow-up study of these trajectories was done to understand the transport phenomena of water and hydrated excess proton; results confirmed that the excess proton exhibits sub-diffusive behavior during the proton transport, as well as caging effects due to the natural confinement of the water region from the polymer membrane.[125]

Simulation models of ultrathin electrochemical cells have shown improved electrolytic dynamics.[129-131] The nanometer-thin inter-electrode distance facilitates Coulomb transport of the electrolytes due to the overlap in the double layers of the electrodes and the minimal screening of the electric fields from the electrolyte. Improved electrolytic dynamics can also be directly correlated with power density. Additionally, these studies examined proton transport in ultrathin electrode systems, confirming improved dynamic properties. In fact, when researchers decomposed the mean squared displacement of the proton into its vehicular and hopping contributions, they found both mechanisms to be anti-correlated at low voltages, but which then became correlated at higher voltages.[130]

We know that the maximum theoretical voltage for a PEMFC should be ~1.23 V due to the oxidation of the hydrogen gas at the anode and the reduction of oxygen at the cathode (at 80%

efficiency of the fuel cell). However, only a few simulation studies have examined the effects of electric fields on PFSA membranes. AIMD studies have used electric fields to understand the electro-osmotic drag coefficient in lamellar-like Nafion,[116] indicating that electric fields enhance proton hopping properties in the polymer, while observing an osmotic drag coefficient close to 1.0. These results are in good agreement with experimental findings,[132] but not captured well in classical MD simulations suggesting an osmotic drag coefficient of ~8-20.[133] Experimental findings confirm the occurrence of morphological changes from the application of an electric field in poled Nafion membranes.[134] Later, coarse-grained (CG) simulations of low hydration PEM systems applied higher voltage levels (~10^9 V/m, which equals 0.1 V/Å) to examine structural changes in the polymer that revealed hexatic structuring.[135-136] Specifically, the hexatic structure in these CG simulations formed under an external electric field via the aggregation of side chains that created stable water channels.

Neither AIMD nor CG simulations have fully examined the dynamics of hydrated excess protons with respect to PFSA hopping mechanisms along sulfonate groups. Accordingly, the current work further studies the role of electric fields on proton transport in PFSA systems by applying various electric field magnitudes to a random morphology of Nafion. With available electric field studies documenting increased hopping and sulfonate aggregation, this study was designed to elucidate how electric fields influence the proton hopping mechanism and caging effects identified in prior reactive MD simulations of similar systems. We applied the multistate empirical valence bond (MS-EVB) method[45-49] since it is able to determine length and timescales, which is not possible using AIMD simulations, while capturing the bond rearrangements associated with the Grotthus mechanism.

II. Simulation Details

We investigated the effects of electric fields on the random morphology of Nafion PEM systems at hydration levels (λ) of both 10 and 15 at room temperature (300 K) and at PEMFC operating temperature (353 K). The random morphology was generated using the Monte Carlo algorithm of Knox and Voth[137] using 4 PFSA chains each with 10 sulfonate side chains corresponding to an empirical weight of 1100. Water molecules and hydroniums were placed in the box corresponding to $\lambda 10$ and $\lambda 15$. A single system for each hydration level was equilibrated with classical molecular dynamics, first by running in the constant NPT ensemble with a pressure of 1.0 atm and at an initial temperature of 10 K and a final temperature of 400 K for 6 ns, then for an additional 6 ns at 400 K. The system density was then determined by running constant NPT simulations at 300 K and 353 K for an additional 6 ns. The system was further equilibrated in a constant NVT simulation at its respective temperature for 6 ns using the Nose-Hoover thermostat with a 100 fs time constant. Five additional replicas of each hydration level and temperature where then generated by pulling configurations every 6 ns from the constant NVT ensemble at 500 K; these additional replicas were then equilibrated at the desired temperature for 12 ns.

We sought to determine systematically how electric fields at 0.00 V/Å, 0.01 V/Å, 0.02 V/Å, and 0.03 V/Å influence the structure of the Nafion PEM and the dynamics of proton transport. Each replica was equilibrated in the electric field by gradually increasing the voltage from 0.0 V/Å to its desired voltage for 6 ns, and then further equilibrated for an additional 6 ns. After this non-reactive equilibration, the system was equilibrated reactively for an additional 200 ps in the constant NVT ensemble with a time constant of 100.0 fs; production runs of these reactive simulations occurred in the constant NVT ensemble for 1 ns using a thermostat time constant of 1000.0 fs.

We used the DREIDING[138] force field to model the Nafion polymer, but with modifications implemented by Savage and coworkers[6, 126]. Standard Lorentz-Berthelot mixing rules were used for the Lennard-Jones (LJ) interactions, except for the LJ term between the oxygen of the sulfonate and the hydrogen of the hydronium, which was modeled with σ = 1.9667 Å and ε = 0.02739 kcal/mol to reproduce the free-energy difference between the 1st and 2nd sulfur-CEC solvation shell of our previous model (see Appendix A). Electric fields were applied in the z-direction such that the electric field force was equivalent to the electric field strength (E_Z) times the particle's charge (i.e., first equality in eq 4.1). Reactive simulations were conducted using the self-consistent iterative multistate empirical valence bond (SCI-MS-EVB) method[50] and incorporating MS-EVB 3.2[49] parameters for the hydronium and SPC/Fw[84] for the water. In SCI-MS-EVB simulations, each excess proton is delocalized amongst N water molecules whereby each water molecule in a given EVB complex has a probability of being covalently bonded to the excess proton (c_j^2). For these SCI-MS-EVB simulations, the force of the electric field for these molecules utilizes the state-averaged charge of each atom, as shown by the right equality in eq 4.1

$$\mathbf{F}_{\mathrm{i,z}}^{E} = q_i E_z = \sum_{j}^{N} c_j^2 q_j^i E_z \,, \tag{4.1}$$

where the sum is over all states of the EVB complex, c_j^2 is probability of state $|j\rangle$, and q_j^i is the charge of atom i in state $|j\rangle$.

III. Results

A. Structural Properties: Sulfur-CEC Association

The PFSA proton hopping mechanism involves the associations of the hydrated excess proton and the sulfonate group. We describe the excess proton using the center-of-excess charge (r_{CEC}), which is the state averaged center-of-charge for each reactive proton (eq 4.2).

$$r_{CEC} = \sum_i c_i^2 \, r_{COC} \tag{4.2}$$

We examined the structural properties of the sulfonate group and the CEC by employing the sulfur-CEC radial distribution function (RDF). Figure 4-1 illustrates the sulfur-CEC RDFs for the various voltages for the two hydration levels and temperatures. The RDFs confirm two dominant solvation shells centered around 4.2 Å and 5.5 Å. Interestingly, there was only a negligible effect on the sulfur-CEC interactions for the various applied voltages, with a slight increase in structuring observed in the first solvation shell in the case of the $\lambda 10$ at 353 K simulations at the highest voltage. We ascribe the lack of a marked sulfur-CEC association in our study, but which was recorded in prior AIMD simulations,[116] to the differing Nafion morphology, coupled with availability of increased statistical data using the SCI-MS-EVB method. On the other hand, we noted a stronger dependence on the hydration level and simulated temperature with respect to our sulfur-CEC RDF findings. Increasing the water content expands the hydrophilic channels, creating for a larger network for the excess proton to transport through (i.e., increased configurational entropy), and further reduces the sulfur-CEC RDF in the first and second solvation shell. Increasing the temperature serves to further increase the structuring in the first solvation shell of the sulfur-CEC RDF.

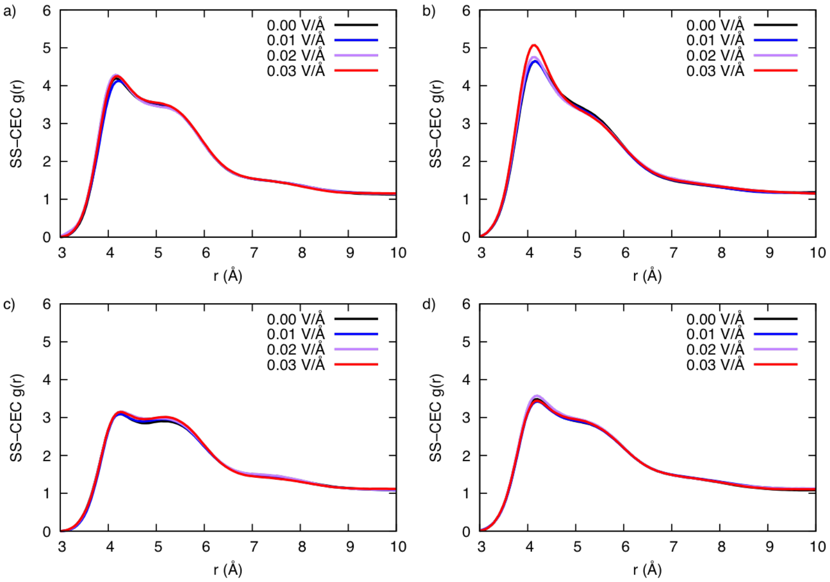

Figure 4-1: Sulfur-CEC radial distribution function for (a) $\lambda 10$ at 300 K, (b) $\lambda 10$ at 353 K, (c) $\lambda 15$ at 300 K, (d) $\lambda 15$ at 353 K. The black line corresponds to 0.00 V/Å, blue corresponds to 0.01 V/Å, purple corresponds to 0.02 V/Å, red corresponds to 0.03 V/Å.

We further investigated the interaction between the excess proton and the sulfonate groups by calculating the number of sulfonate groups associated with an excess proton. Specifically, we counted the number of sulfonate groups within the first and second solvation shells of the most probable hydronium ion to associate with the sulfonate group using the sulfur-O_H RDF (Appendix B, Figure 4-9) to distinguish the first and second solvation shells as sulfur atoms within 4.2 Å and 6.5 Å of the most likely hydronium-oxygen atom, respectively .

Figure 4-2 provides the probability distribution indicating the number of sulfonate groups associated with a hydrated proton. Similar to the sulfur-CEC RDFs, we confirmed that this probability is dependent on the hydration level and temperature, but is independent of the applied voltage. Within the first solvation shell (Figures 4-2a and 4-2b), the hydrated proton was observed to be largely un-associated with any sulfonate groups at both simulated temperatures. However, simulations at 353 K demonstrated a higher probability of being associated with a sulfonate group, as shown by the reduced probability of not being associated with any sulfonate groups. Increasing the water content further reduces the hydrated proton from being associated with a sulfonate group, which is in good agreement with the reduced sulfur-CEC RDFs in the $\lambda 15$ in comparison with the $\lambda 10$.

Within the second solvation shell the probability of the hydrated proton being associated with one or more sulfonate groups drastically increases. In the $\lambda 10$ simulations, an excess proton was found to be associated with one or more sulfonate groups 95% of the time, dropping to ~80% for the $\lambda 15$ simulations. The smaller hydrophilic pore in the $\lambda 10$ simulations increases the probability that the hydrated proton will associate with two sulfonate groups; moreover, the increased water content in the $\lambda 15$ simulations was found to expand the pore, thereby shifting the largest probability to one sulfonate group. The fact that the hydrated proton is almost always associated with one or more sulfonate groups strongly supports the PFSA proton hopping mechanism along the sulfonate groups, given that the diffusion of the hydrated proton rarely occurs in the bulklike region of the hydrophilic pore away from any sulfonate groups.[6] The minimal impact of applied voltage on the association between hydrated protons and sulfonate groups (Figures 4-1 and 4-2) indicates that PFSA hopping mechanism is not perturbed under an electric field.

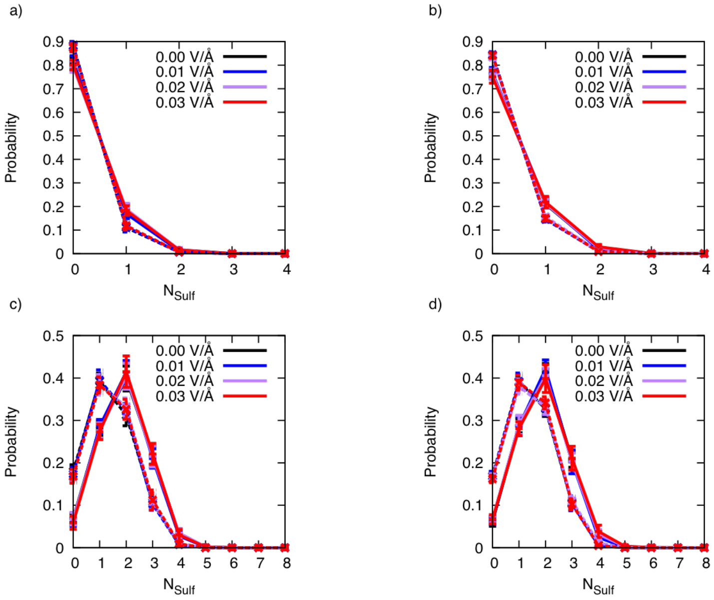

Figure 4-2: Probability distribution describing the number of sulfonate groups per hydrated proton. Figure 4-2a and b correspond to the first solvation shell defined at 4.2 Å, and Figures 4-2c and d correspond to the 2nd solvation shell defined at 6.5 Å. Figures 4-2a and c correspond to simulations at 300 K, and Figures 4-2b and d correspond to simulations at 353 K. Solid lines correspond to $\lambda 10$ and dashed lines correspond to $\lambda 15$. The black line corresponds to 0.00 V/Å, blue corresponds to 0.01 V/Å, purple corresponds to 0.02 V/Å, red corresponds to 0.03 V/Å.

B. Structural Properties: Sulfonate Side Chain Configurations

Given the minimal impact of an electric field on the structural properties of hydrated protons, we next examined how an electric field influenced the conformation of the pendant side chain by determining its extension and angular configurations in the hydrophilic pore. For each side chain pendent, we defined two vectors centered on the backbone carbons covalently bonded to the side chain. The first vector points to the sulfur atom, while the second vector points to the oxygen atom covalently bonded to the backbone carbon atom. We then defined the angular configuration as the angle between these two corresponding vectors; here, we use *d* to define the distance between the backbone carbon atom and the sulfur atom (see Figure 12a in Ref. [6]).

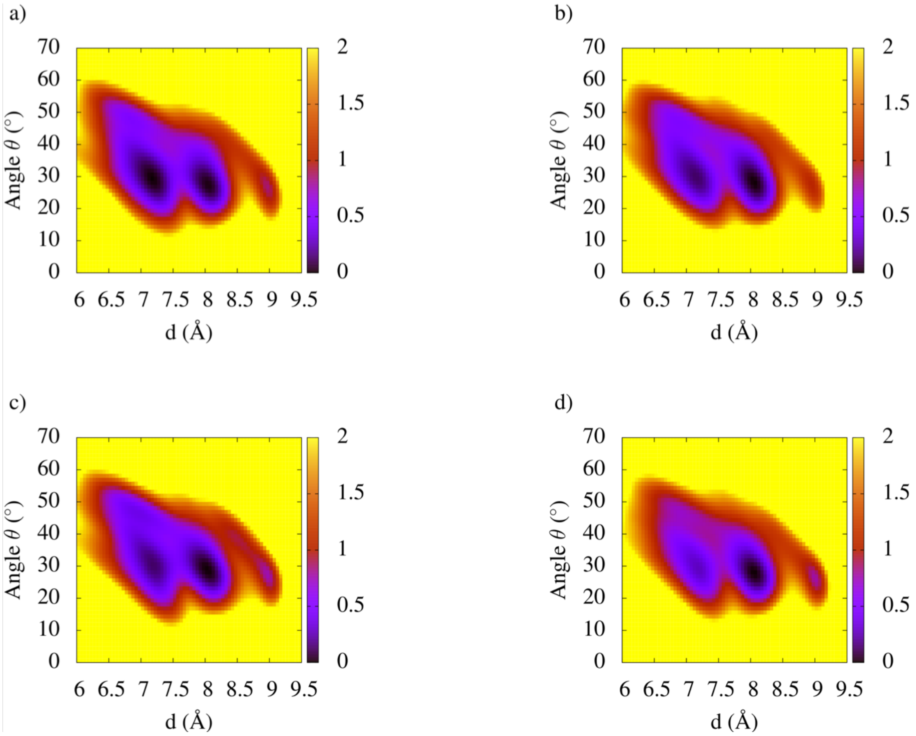

Figure 4-3: Potential of Mean Force (PMF) for the side chain configuration as a function of side chain length (d) and angle for λ15 at 353 K. Units are in kcal/mol.

Figure 4-3 depicts the two-dimensional potential of mean force for the side chains for λ15 at 353 K. In the absence of an electric field (Figure 4-3a), the side chain was identified in two dominant configurations: one around 7 Å and another at 8 Å; additionally, a less probable configuration at 9 Å was also observed. Note that the side chain for the 7 Å configuration took on a more bent configuration and samples the broadest possible angular configurations. When the side chain was extended to 8 Å, it extended further into the hydrophilic pore and was much more linear, as shown by the reduced angular configurations. Additionally, in the absence of an electric field we recorded very similar free-energy minimum values for the two configurations. In contrast, under an electric field the probability of observing side chains in the 7 Å confirmation diminished, while the probability for the presence of a free-energy well at 9 Å increased (Figures 4-3b-d). The change in PMF with the application of external voltage promotes the protrusion of sulfonate chains into the water network by aiding the side chains to assume a more linear configuration. Corresponding PMFs for other simulation setups can be found in Appendix B, Figures 4-10 through Figure 4-12.

C. Structural Properties: Sulfur-Sulfur Radial Distribution Function

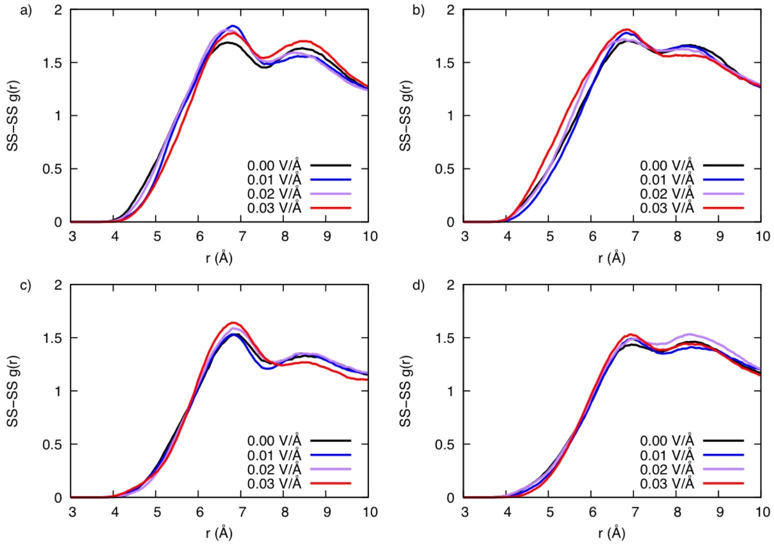

Figure 4-4: Sulfur-sulfur radial distribution function for (a) λ10 at 300 K, (b) λ10 at 353 K, (c) λ15 at 300 K, (d) λ15 at 353 K. The black line corresponds to 0.00 V/Å, blue corresponds to 0.01 V/Å, purple corresponds to 0.02 V/Å, red corresponds to 0.03 V/Å.

We further investigated side-chain structures by examining the sulfur-sulfur RDFs. As shown in Figure 4-4, we observe two peaks at ~6.4 Å and ~8.4 Å. As previously detailed,[6] the first peak is within one to two solvation shells of the excess proton, while the second peak is within the second to third solvation shell. As such, the excess proton experiences a uniform potential energy surface in the hydrophilic pore due to the close proximity of an excess proton with multiple sulfonate groups.[6] When an electric field was applied to the system, we observed a slight increase in sulfur-sulfur structuring, which could have resulted from the increased linear configuration in the side chains protruding into the water network (Figure 4-3); this phenomena has also been reported for united-atom simulations of ionomers under strong electric fields.[135-136] However, our results show that the sulfur-sulfur RDFs were significantly dependent on hydrational level and temperature, which is in agreement with the sulfur-CEC RDFs (Figure 4-1). Expanding the hydrophilic channel by increasing the water content works to reduce the structuring of the sulfonate groups. Additionally, the increased kinetic energy found in the 353 K simulation was found to increase the flexibility of the side chains in the hydrophilic pore, thereby enabling the first two peaks in the sulfur-sulfur RDFs to have increased overlap.

Overall, we verified that the application of an electric field only minimally impacted the structural properties of the hydrated proton and sulfonate groups. This finding strongly suggests that the PFSA proton hopping mechanism, whereby the proton diffuses through the water channel via the influence of pendant side chains, is still viable under an applied electric field. In light of this result, we further investigated the effects of an electric field on the dynamical properties of the hydrated excess proton.

D. Dynamical Properties: CEC Diffusion

The displacement of charged particles in an electric field arises from normal diffusion coupled with additional momentum originating from the electric field.[139] When the electric field is applied in the z-direction, as was the case for this study, we can write the displacement vector as

$$\boldsymbol{r}_{\mathrm{E}}(\mathrm{t}) = \boldsymbol{r}_{\mathrm{D}}(\mathrm{t}) + \boldsymbol{v}_z \mathrm{t}, \tag{4.3}$$

where $\boldsymbol{r}_{\mathrm{E}}(\mathrm{t})$ is the position vector in the presence of an external electric field, $\boldsymbol{r}_{\mathrm{D}}(\mathrm{t})$ is the position vector due to diffusion (i.e., the absence of external field), $\boldsymbol{v}_z$ is the drift velocity that results from the external fields in the z-direction, and t is the time. The resulting mean squared displacement (MSD) of eq 4.3 for the displacement in an electric field can be written as

$$\langle \boldsymbol{r}_{\mathrm{E}}(\mathrm{t})^2 \rangle = \langle \boldsymbol{r}_{\mathrm{D}}(\mathrm{t})^2 \rangle + \langle \boldsymbol{v}_z \rangle^2 t^2 \tag{4.4}$$

where the cross terms are zero because the mean displacement with no external field is zero. From eq 4.4 we note that the MSD of charged particles in the electric field is non-linear with time in the direction of the electric field, which corresponds to super-diffusive dynamical properties.

We tracked the dynamics of the excess proton by calculating the MSD of the CEC in the various Nafion simulations. Prior simulation results have shown that the dynamics of the CEC exhibit sub-diffusive properties in the hydrophilic pores of perfluorosulfonic acid membranes and strong caging effects in the time scales.[125] Accordingly, we sought to determine how the system would be impacted under an applied electric field. The MSD, $\langle \mathrm{r}^2 \rangle$, can be fitted as a function of time, t, according to eq 5.5., where d is the dimensionality of the MSD, which equals 3 for the isotropic MSD, 2 for the xy-direction, and 1 for the z-direction – and D_α is the diffusion coefficient.

$$\langle \mathrm{r}^2 \rangle = 2\mathrm{d}\mathrm{D}_\alpha \mathrm{t}^\alpha \tag{5.5}$$

By fitting eq. 5.5 in the long-time regime (500 ps - 1000 ps) to the MSD of the CEC, we can gain insight into the transport behavior of the excess proton in these simulations, where normal diffusion occurs when α equals 1, sub-diffusive when α is less than 1, and super-diffusive when α is greater than 1. Note that it is difficult to compare the diffusion coefficient (D_α) in these simulations as their units are in terms of α.

Figure 5-5 shows the mean squared displacement for the center of excess charge for the $\lambda 15$ at 353 K, in addition to the MSD in the z-direction (Figure 5-5b) and xy-direction (Figure 5-

5c). Corresponding MSDs for other simulation were found to be similar (Appendix B, Figures 4-13 through Figures 4-15). For simulations in which no external electric field was applied to the system, we found that the simulations demonstrated sub-diffusive behaviors corresponding to simulation temperature: simulations at 300 K had α values close to ~0.7, and simulations at 353 K had α values close to ~0.86 (see Appendix B, Tables 4-3 through 4-5). These values are similar to CEC diffusion results for other perfluorinated systems.[125] The application of an electric field reduces the sub-diffusive behavior of the hydrated proton and shifts the mechanism to super-diffusion under larger applied voltages (0.02 – 0.03 V/Å), which confirms the non-linear dependence of MSD with time (eq. 4.4).

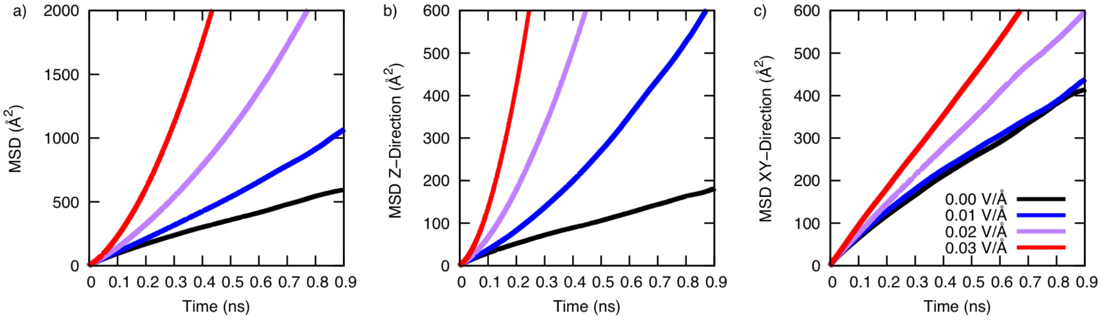

Figure 4-5: Mean squared displacement of the center of excess charge in λ=15 at 353 K (a) isotropic diffusion, (b) z-direction, and (c) xy-direction. Black corresponds to 0.00 V/Å, blue corresponds to 0.01 V/Å, purple corresponds to 0.02 V/Å, and red corresponds to 0.03 V/Å.

Table 4-1: Fits to equation 4.5 for isotropic MSD, MSD in z-direction, and MSD in xy-direction for λ15 at 353 K.

Voltage $\left(V/_{Å}\right)$	D_α $\left(Å^2/_{ps^\alpha}\right)$	α	D_α^Z $\left(Å^2/_{ps^\alpha}\right)$	α_Z	D_α^{XY} $\left(Å^2/_{ps^\alpha}\right)$	α_{XY}
0	0.28	0.86	0.22	0.88	0.32	0.85
0.01	0.06	1.19	0.02	1.45	0.34	0.85
0.02	0.01	1.51	0.01	1.70	0.22	0.96
0.03	0.02	1.62	0.03	1.71	0.14	1.07

We further examined the MSD by decomposing the isotropic MSD into its z- and xy-components (Figures 4-3b and 4-3c, respectively). In the decomposed MSD, we observed sub-diffusive proton transport behaviors for simulations with no applied electric field. In agreement with the isotropic MSD, we observed increased super-diffusive behavior in the direction of the applied electric field (z-direction). Interestingly, we also observed that diffusion behaviors normal to the electric field more closely approximated normal diffusion and super-diffusive behavior in simulations with 0.03 V/Å (see Table 4-1 and Appendix B, Table 4-3 through 4-5). We attribute the reduced sub-diffusive behavior normal to the applied electric field to the coupling between the proton transport and the polymer, since we have observed that electric fields minimally perturb the structural properties of a PFSA system.

E. Dynamical Properties: Sulfur Decomposed MSD

Additionally, we investigated the decomposition of the displacement vector for the excess proton based on its association with or without sulfonate groups (eq 4.6).

$$\Delta r(t) = \Delta r_{assoc}(t) + \Delta r_{free}(t) \tag{4.6}$$

The corresponding MSD of eq 4.6 can then be written as

$$\langle \Delta r(t)^2 \rangle = \langle \Delta r_{assoc}(t)^2 \rangle + \langle \Delta r_{free}(t)^2 \rangle + 2\langle \Delta r_{assoc}(t) \Delta r_{free}(t) \rangle, \tag{4.7}$$

where the first and second terms on the right-hand side correspond to the mean squared displacement of the CEC, either associated or free of a sulfonate group, respectively; the final term in the equation corresponds to the correlation between the two. Previous simulations have confirmed large diffusion effects associated with a sulfonate group, which suggested the importance of sulfonate groups in the PFSA hopping mechanism. In practice, the CEC displacement vector is parsed into 100 fs segments. If at the end of each 100 fs segment the CEC atom is found to be within the first solvation shell of any sulfur atom (4.5 Å), the displacement is then added to the associated vector; otherwise, the displacement is added to the free vector. The mean squared displacement of each vector is then calculated and the correlation is determined by algebraically manipulating eq. 4.7.

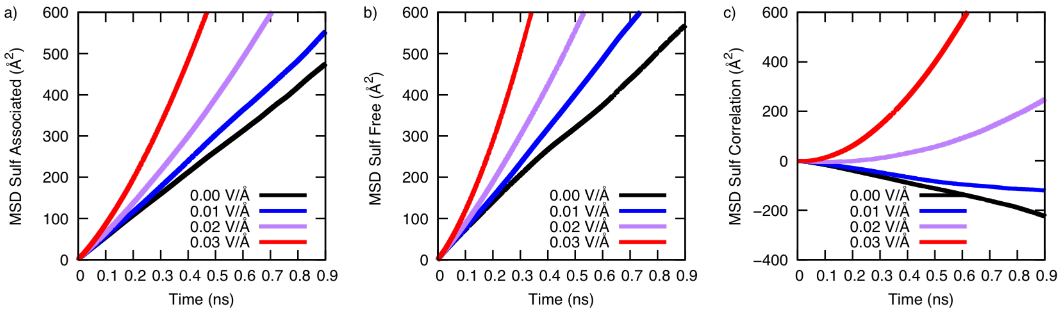

Figure 4-6: CEC MSD results as a function of (a) the presence of a sulfonate group and (b) absence of a sulfonate group, and (c) the correlation between the two diffusive behaviors.. Black corresponds to 0.00 V/Å, blue corresponds to 0.01 V/Å, purple corresponds to 0.02 V/Å, and red corresponds to 0.03 V/Å.

Table 4-2: Data fitted to eq. 4.5 for MSD associated with a sulfonate group, MSD free of a sulfonate group, and the correlation between the two for λ=15 at 353 K.

Voltage $\left(V/\text{Å}\right)$	$D_{\boldsymbol{\alpha}}^{Assoc}$ $\left(\text{Å}^2/\boldsymbol{ps^{\alpha}}\right)$	$\boldsymbol{\alpha}_{\text{Assoc}}$	$D_{\boldsymbol{\alpha}}^{Free}$ $\left(\text{Å}^2/\boldsymbol{ps^{\alpha}}\right)$	$\boldsymbol{\alpha}_{\text{Free}}$	$D_{\boldsymbol{\alpha}}^{Corr}$ $\left(\text{Å}^2/\boldsymbol{ps^{\alpha}}\right)$	$\boldsymbol{\alpha}_{\text{Corr}}$
0	0.09	1.00	0.09	1.02	-0.01	1.23
0.01	0.07	1.06	0.15	1.07	-0.37	0.59
0.02	0.03	1.23	0.02	1.36	$1.9\text{x}10^{-5}$	2.48
0.03	0.01	1.51	0.02	1.45	$5.8\text{x}10^{-4}$	1.88

Figure 4-6 provides CED MSD findings for the $\lambda15$ simulation at 353 K as a function of the presence (Figure 4-6a) or absence (Figure 4-6b) of a sulfonate group. (Note that the CEC is considered to be associated with a sulfonate group if it is within 4.5 Å of the sulfur atom.) Figure 4-6c illustrates the correlation between the two diffusive behaviors. Table 4-2 lists the data fitted to eq. 4.5. Note that corresponding figures (Figures 4-16 through 4-18) and fits (Tables 4-6 through 4-8) for other simulations can be found in Appendix B.

In agreement with earlier simulations, we found that the diffusion of excess proton associated with a sulfonate group is rather large and therefore cannot be discounted; in fact, it displayed a magnitude resembling the dynamics of a sulfonate-free group. Additionally, we noted that the correlation between the two processes at 0.00 V/Å was negative, meaning the two processes are anticorrelated and work against each other. When an electric field is applied, both the associated and free diffusion exhibit enhanced super-diffusive properties with the magnitude of the applied voltage, as evidenced by α. Interestingly, we observed that the correlation between the two diffusive mechanisms became less anticorrelated, which can be clearly seen in the correlation plot shown in Figure 4-6c. In the $\lambda15$ simulations at 353 K, we observed that the diffusion between the two mechanisms become positively correlated when higher voltages were applied, thus indicating that electric fields contribute to the total diffusion within the hydrophilic pore along the sulfonate groups and outside the first solvation shell.

F. Dynamical Properties: Examining the caging effects

We then analyzed the caging effects of the CEC within the hydrophilic pore using a published approach.[125] Specifically, we calculated the angle between two displacement vectors based on a given step size, Δt. For an angle of displacement at $t = t_0$, we constructed two displacement vectors defined as $r_1 = r(t_0 + \Delta t) - r(t_0)$ and $r_2 = r(t_0) - r(t_0 - \Delta t)$; we describe the angle between these vectors as $\cos(\theta)$. As a reminder, a $\cos(\theta)$ value of -1 corresponds to the CEC returning in the direction from which it originated, while a value of 1 corresponds to the CEC moving away from its initial position. By calculating the average for all initial positions and step sizes, we were able to determine the joint probability of this angle as a function of time in order to understand caging effects in the water channel.

The joint-probability distribution functions for $\lambda 15$ at 353 K is shown in Figure 4-7 for the corresponding external fields (0.00-0.03 V/Å). In a stochastic diffusion process, these plots should be uniform across all timescales and angles. However, the complex water network characterizing a Nafion PEM is able to confine the CEC when there is no applied voltage, as shown by the large probability at $\cos(\theta) = -1$ for all step sizes (Figure 4-7a), which is in agreement with previous PFSA findings.[125] As voltage is applied to the system, caging effects are found to have reduced timescales (<100 ps), resulting in more uniform distributions (Figure 4-7b) or a higher probability of the CEC moving away from its initial position, as shown in Figures 4-7c and 4-7d as large probabilities when $\cos(\theta) = 1$. This result suggests that an electric field will push the protons through the system via reduced caging effects. In light of unperturbed sulfur-CEC interactions and other structural properties, we propose that an electric field will assist in proton transfer from one potential energy well around a sulfonate groups to another.

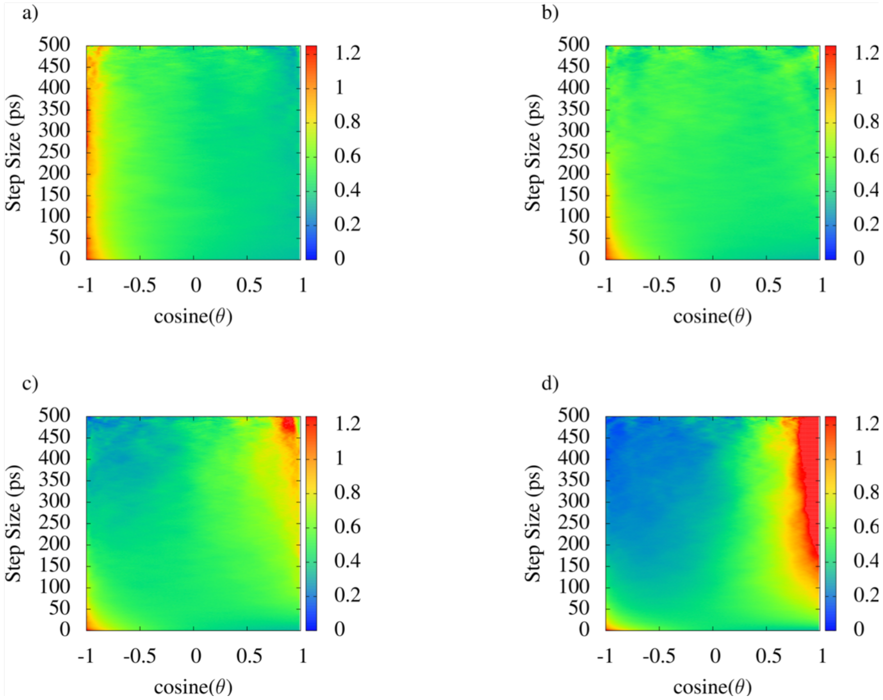

Figure 4-7: Joint probability distribution for the relative angle between two displacement vectors as a function of time step lengths for λ15 at 353 K. Each time-slice is normalized so that the integral of the distribution is set to 1.0. Note: cosine(180°) = -1, cosine(90°) = 0.0, and cosine(0°) = 1.

IV. Conclusion

This study utilized reactive molecular dynamics simulations to understand the influence of applied electric fields on Nafion PEM membranes at various hydration levels and temperatures. Overall, we found that electric fields exert only a minimal impact on the structural properties of the random morphology of Nafion, indicating that the proton hopping mechanism, which requires the facilitation of sulfonate groups in the hydrophilic pore, is still present. Instead, we confirmed that hydration level and simulation temperature have a more pronounced effect on the structure of Nafion. Moreover, we found that the effect of Coulomb transport on the hydrated protons in these membranes, observed through super-diffusive dynamics, did reduce caging effects in the hydrophilic pore. The results from this study also confirmed the presence of certain cooperative effects of electric fields on the polymeric system, principally extensions of the pendant side chains and enhanced diffusion normal to the applied electric field. In light of these results, we propose that electric fields enhance proton diffusion in hydrophilic pores by enabling protons to escape from the potential energy well of one sulfonate group into another.

A follow-on study involves placing the Nafion PEM in the electrochemical cell and using the image charge method to account for the polarizability of the electrodes.[129] However, it has been shown that PEM membranes in confined environments, such as the case in the catalyst layer of the PEMFC, exhibit reduced transport phenomenon.[140-143] Thus, future work not only involves modeling a full electrochemical cell with the Nafion PEM acting as the electrolyte, but also determining optimal empirical weights and hydration levels for the Nafion PEM that exhibit Coulomb transport arising from the potential difference of the electrodes.

Appendix A: Determination of Repulsive Term

The MS-EVB 3.0 model suffered from strong attractions between counterion pairs, which required the use of a repulsive term to weaken these interactions.[6, 102] In the MS-EVB 3.0 model, the H_H-Cl term was parameterized to match experimental RDFs,[102] which further influenced the choice of Lennard-Jones (LJ) parameters for the O_S-H_H term in PFSA membranes (see Supporting Information in Ref. [6]). This current work uses the MS-EVB 3.2 model, which forms weaker counterion pairings compared to our previous model.[49] For the PEM systems used in this work, we parameterized the O_S-H_H term to reproduce the free-energy barrier in the sulfur-CEC potential of mean force (PMF) of Nafion in our previous model.[126] We do this by replicating a similar combinatorics scheme shown in the SI for Ref. [6]). We generated four independent configurations of Nafion with a hydration level of 10 at the density level reported in Ref [126]. Each configuration was equilibrated in the constant NVT ensemble at 300 K using the SCI-MS-EVB 3.2 method. The LJ parameters examined were σ values of 1.6667 Å and 1.8167 Å with ε values of 0.01589, 0.02239, 0.02739, and 0.0316 kcal/mol.

In Figure 4-8, we show the sulfur-CEC PMF for these simulations run in the constant NVE ensemble for 1 ns using SCI-MS-EVB 3.2. Note that a σ value of 1.6667 Å is in better agreement with the free-energy barrier of MS-EVB 3.0 than a σ value of 1.8167 Å, which produces an excessive repulsive interaction. For the σ value of 1.6667 Å, we find that an ε value of 0.02739 kcal/mol best matches the free-energy barrier, although we note that all the epsilon values examined here are very close to the free-energy barrier. We ultimately chose σ = 1.9667 Å and ε = 0.02739 kcal/mol for the O_S-H_H LJ interaction as it most closely matched the barrier height of our previous model.

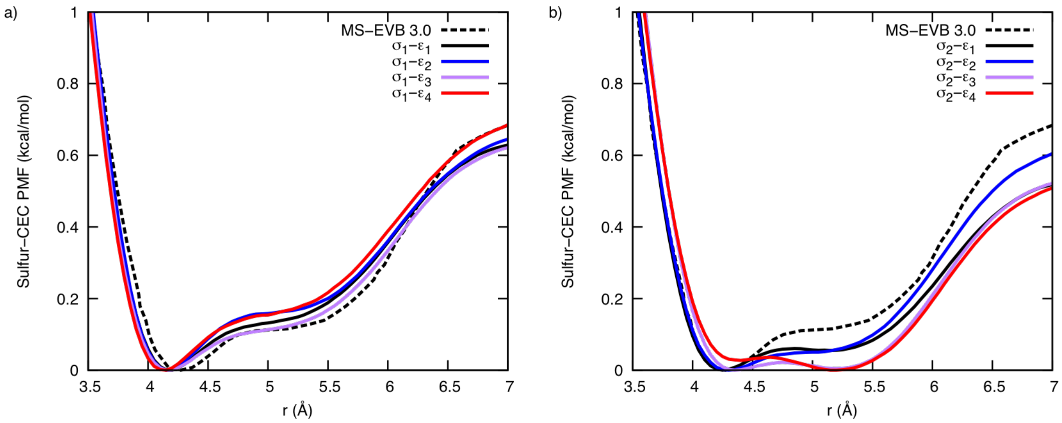

Figure 4-8: Sulfur-CEC potential of mean force (PMF) determined by inverting the sulfur-CEC RDF. σ_1 and σ_2 corresponds to a value of 1.6667 Å and 1.8167 Å, respectively. ε_1- ε_4 correspond to values of 0.01589, 0.02239, 0.02739, and 0.0316 kcal/mol, respectively.

Appendix B: Additional Structural Properties

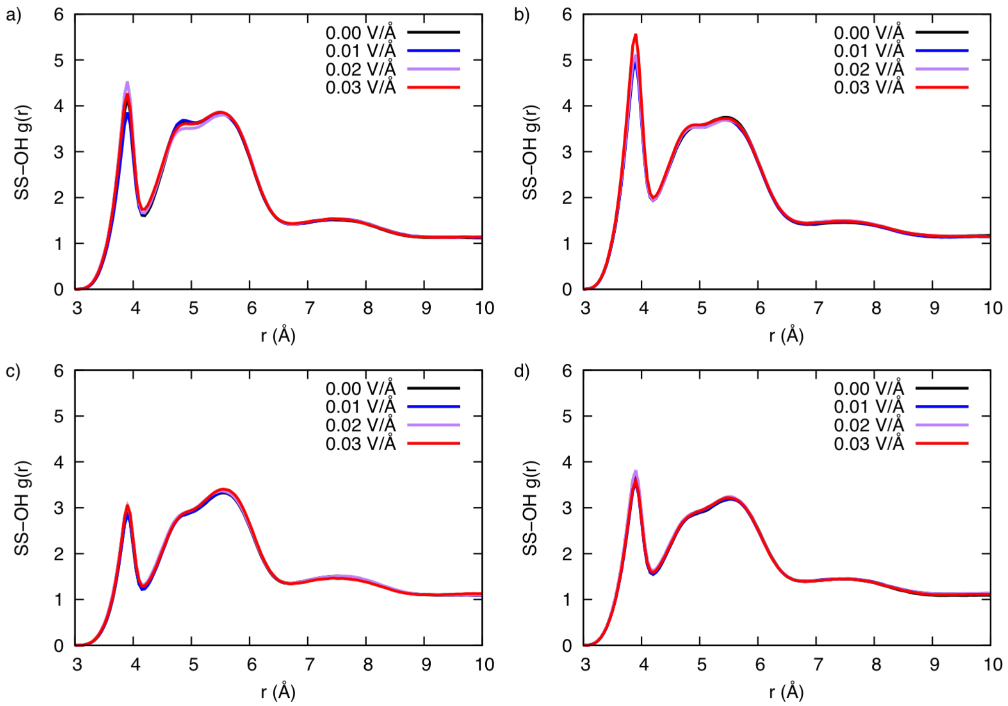

Figure 4-9: Sulfur-OH radial distribution for (a) λ10 at 300 K, (b) λ10 at 353 K, (c) λ15 at 300 K, (d) λ15 at 353 K. Black corresponds to 0.00 V/Å, blue corresponds to 0.01 V/Å, purple corresponds to 0.02 V/Å, and red corresponds to 0.03 V/Å.

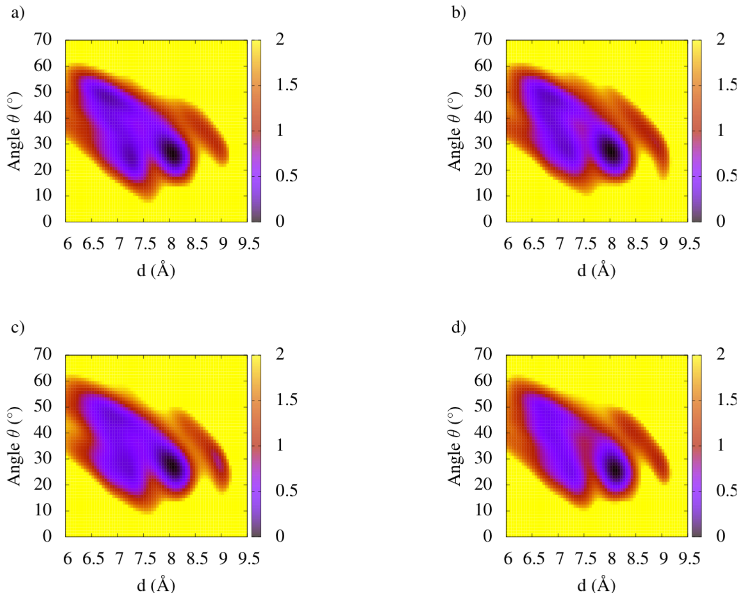

Figure 4-10: Potential of Mean Force (PMF) for the side chain configuration as a function of side chain length (d) and angle for λ10 at 300 K. Units are in kcal/mol.

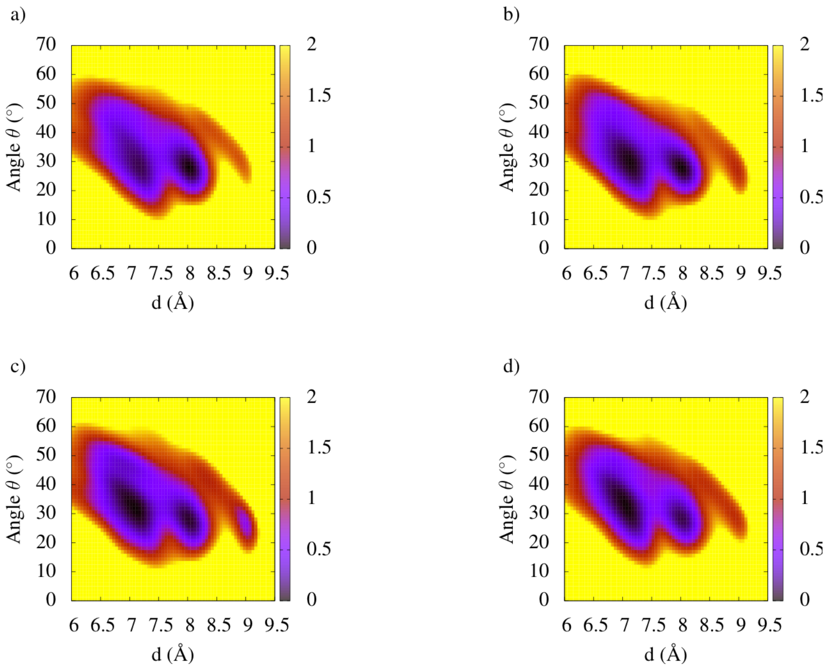

Figure 4-11: Potential of Mean Force (PMF) for the side chain configuration as a function of side chain length (d) and angle for λ10 at 353 K. Units are in kcal/mol.

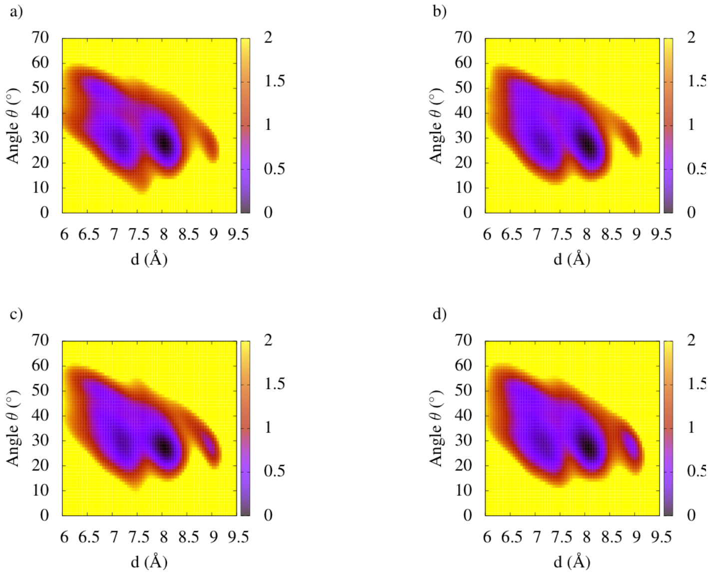

Figure 4-12: Potential of Mean Force (PMF) for the side chain configuration as a function of side chain length (d) and angle for λ15 at 300 K. Units are in kcal/mol.

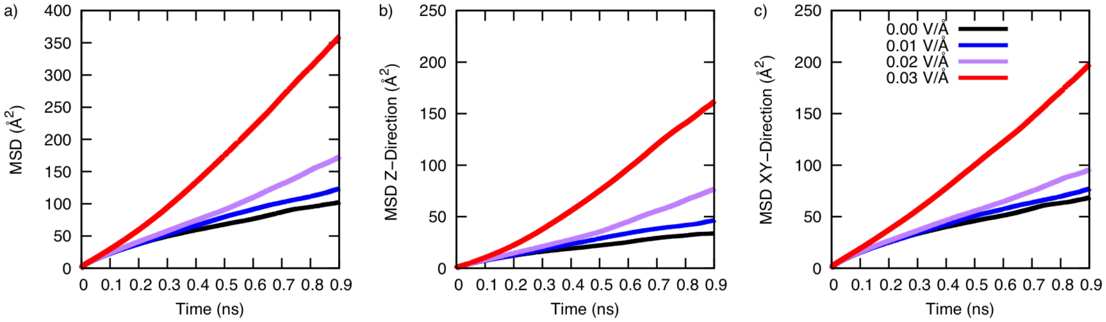

Figure 4-13: Mean squared displacement of the center of excess charge in λ10 at 300 K (a) isotropic diffusion, (b) z-direction, and (c) xy-direction. Black corresponds to 0.00 V/Å, blue corresponds to 0.01 V/Å, purple corresponds to 0.02 V/Å, and red corresponds to 0.03 V/Å.

Table 4-3: Fits to eq. 4.5 in main text for isotropic MSD, MSD in z-direction, and MSD in xy-direction for λ10 at 300 K.

Voltage $\left(V/_{Å}\right)$	D_α $\left(Å^2/_{ps^\alpha}\right)$	α	D_α^Z $\left(Å^2/_{ps^\alpha}\right)$	α_Z	D_α^{XY} $\left(Å^2/_{ps^\alpha}\right)$	α_{XY}
0	0.14	0.71	0.12	0.73	0.15	0.70
0.01	0.13	0.74	0.12	0.78	0.14	0.72
0.02	0.01	1.15	4.2×10^{-3}	1.34	0.03	1.00
0.03	0.02	1.21	0.02	1.25	0.02	1.17

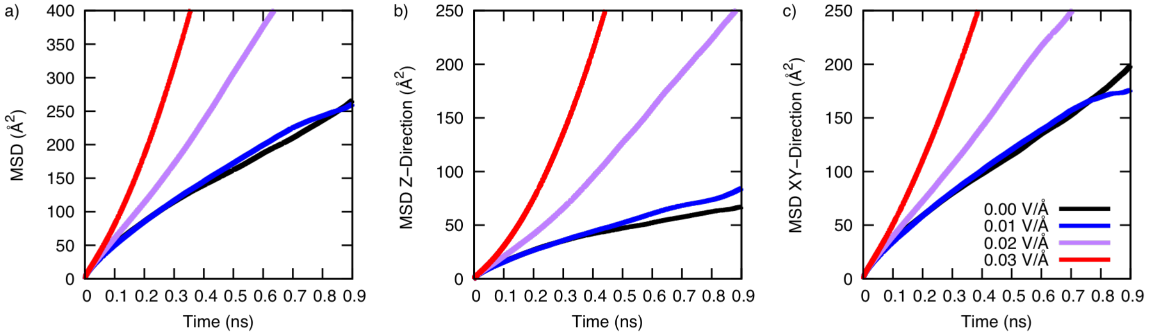

Figure 4-14: Mean squared displacement of the center of excess charge in λ10 at 353 K (a) isotropic diffusion, (b) z-direction, and (c) xy-direction. Black corresponds to 0.00 V/Å, blue corresponds to 0.01 V/Å, purple corresponds to 0.02 V/Å, and red corresponds to 0.03 V/Å.

Table 4-4: Fits to eq 4.5 in main text for isotropic MSD, MSD in z-direction, and MSD in xy-direction for λ10 at 353 K.

Voltage $\left({}^{V}/_{\text{Å}}\right)$	D_α $\left({}^{\text{Å}^2}/_{ps^\alpha}\right)$	α	D_α^Z $\left({}^{\text{Å}^2}/_{ps^\alpha}\right)$	α_Z	D_α^{XY} $\left({}^{\text{Å}^2}/_{ps^\alpha}\right)$	α_{XY}
0	0.12	0.87	0.65	0.58	0.06	0.98
0.01	0.43	0.68	0.18	0.80	0.63	0.63
0.02	0.05	1.12	0.04	1.18	0.06	1.07
0.03	0.01	1.51	0.01	1.62	0.01	1.40

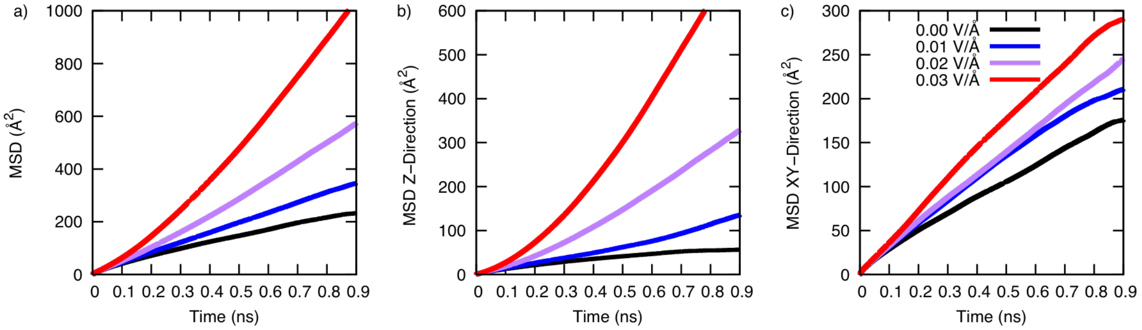

Figure 4-15: Mean squared displacement of the center of excess charge in λ15 at 300 K (a) isotropic diffusion, (b) Z-direction, and (c) XY-direction. Black corresponds to 0.00 V/Å, blue corresponds to 0.01 V/Å, purple corresponds to 0.02 V/Å, and red corresponds to 0.03 V/Å.

Table 4-5: Fits to eq 4.5 in main text for isotropic MSD, MSD in z-direction, and MSD in xy-direction for λ15 at 300 K.

Voltage $\left(V/_{\text{Å}}\right)$	D_α $\left(\text{Å}^2/_{ps^\alpha}\right)$	α	D_α^Z $\left(\text{Å}^2/_{ps^\alpha}\right)$	α_Z	D_α^{XY} $\left(\text{Å}^2/_{ps^\alpha}\right)$	α_{XY}
0	0.23	0.75	1.22	0.46	0.13	0.86
0.01	0.10	0.93	$5.0\text{x}10^{-3}$	1.40	0.54	0.67
0.02	0.04	1.16	0.02	1.36	0.12	0.91
0.03	0.02	1.34	0.01	1.57	0.26	0.83

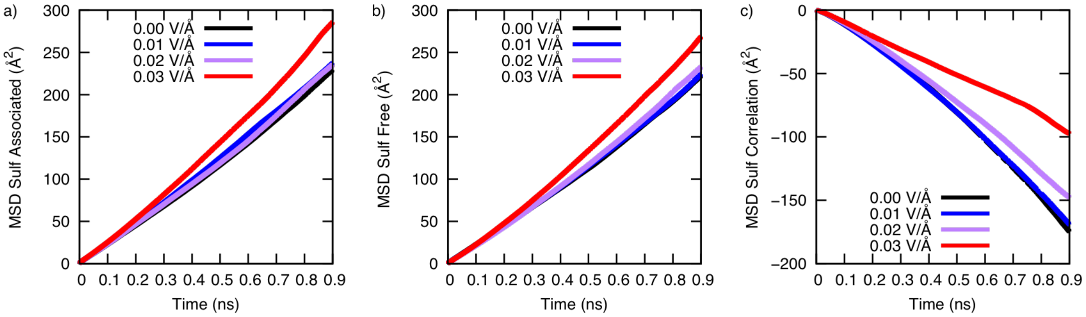

Figure 4-16: Mean squared displacement of the CEC λ10 at 300 K (a) associated with a sulfonate group, (b) free of a sulfonate group, and(c) shows the correlation between free and associated. Black corresponds to 0.00 V/Å, blue corresponds to 0.01 V/Å, purple corresponds to 0.02 V/Å, and red corresponds to 0.03 V/Å.

Table 4-6: Fits to eq. 4.5 in the main text for MSD associated with a sulfonate group, MSD free of a sulfonate group, and the correlation between the two for λ10 at 300 K.

Voltage $\left(V/\text{Å}\right)$	D_{α}^{Assoc} $\left(\text{Å}^2/ps^{\alpha}\right)$	α_{Assoc}	D_{α}^{Free} $\left(\text{Å}^2/ps^{\alpha}\right)$	α_{Free}	D_{α}^{Corr} $\left(\text{Å}^2/ps^{\alpha}\right)$	α_{Corr}
0	0.01	1.16	0.01	1.21	$-3.1\text{x}10^{-3}$	1.34
0.01	0.02	1.10	0.02	1.11	$-4.7\text{x}10^{-3}$	1.28
0.02	0.02	1.14	0.01	1.18	-0.01	1.17
0.03	0.01	1.19	0.01	1.19	-0.01	1.17

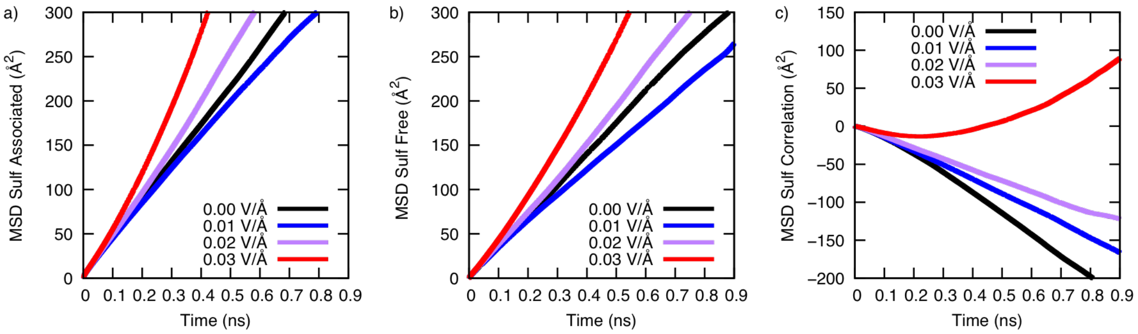

Figure 4-17: Mean squared displacement of the CEC λ10 at 353 K (a) associated with a sulfonate group, (b) free of a sulfonate group, and (c) shows the correlation between free and associate. Black corresponds to 0.00 V/Å, blue corresponds to 0.01 V/Å, purple corresponds to 0.02 V/Å, and red corresponds to 0.03 V/Å.

Table 4-7: Fits to Eq. 4.5 in the main text for MSD associated with a sulfonate group, MSD free of a sulfonate group, and the correlation between the two for λ10 at 353 K.

Voltage $\left({}^{V}/_{\text{Å}}\right)$	D_{α}^{Assoc} $\left({}^{\text{Å}^2}/_{ps^{\alpha}}\right)$	α_{Assoc}	D_{α}^{Free} $\left({}^{\text{Å}^2}/_{ps^{\alpha}}\right)$	α_{Free}	D_{α}^{Corr} $\left({}^{\text{Å}^2}/_{ps^{\alpha}}\right)$	α_{Corr}
0	0.03	1.13	0.10	0.92	-0.02	1.14
0.01	0.20	0.83	0.04	1.02	-0.01	1.11
0.02	0.07	1.04	0.03	1.10	-0.03	0.95
0.03	0.02	1.29	0.01	1.34	$6.9\text{x}10^{-10}$	3.50

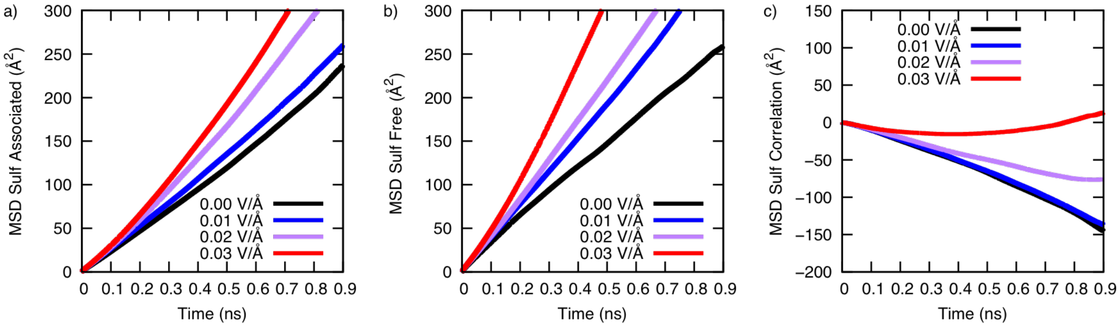

Figure 4-18: Mean squared displacement of the CEC λ15 at 300 K (a) associated with a sulfonate group, (b) free of a sulfonate group, and (c) shows the correlation between free and associate. Black corresponds to 0.00 V/Å, blue corresponds to 0.01 V/Å, purple corresponds to 0.02 V/Å, and red corresponds to 0.03 V/Å.

Table 4-8: Fits to eq. 4.5 in the main text for MSD associated with a sulfonate group, MSD free of a sulfonate group, and the correlation between the two for λ10 at 353 K.

Voltage $\left(V/\text{Å}\right)$	$D_{\boldsymbol{\alpha}}^{Assoc}$ $\left(\text{Å}^2/\boldsymbol{ps^{\alpha}}\right)$	$\boldsymbol{\alpha}_{\text{Assoc}}$	$D_{\boldsymbol{\alpha}}^{Free}$ $\left(\text{Å}^2/\boldsymbol{ps^{\alpha}}\right)$	$\boldsymbol{\alpha}_{\text{Free}}$	$D_{\boldsymbol{\alpha}}^{Corr}$ $\left(\text{Å}^2/\boldsymbol{ps^{\alpha}}\right)$	$\boldsymbol{\alpha}_{\text{Corr}}$
0	0.01	1.20	0.05	0.98	-2.1x10^{-3}	1.37
0.01	0.02	1.16	0.05	1.04	-3.2x10^{-3}	1.30
0.02	0.02	1.16	0.09	0.96	-0.11	0.71
0.03	0.02	1.23	0.04	1.17	1.4x10^{-8}	2.91

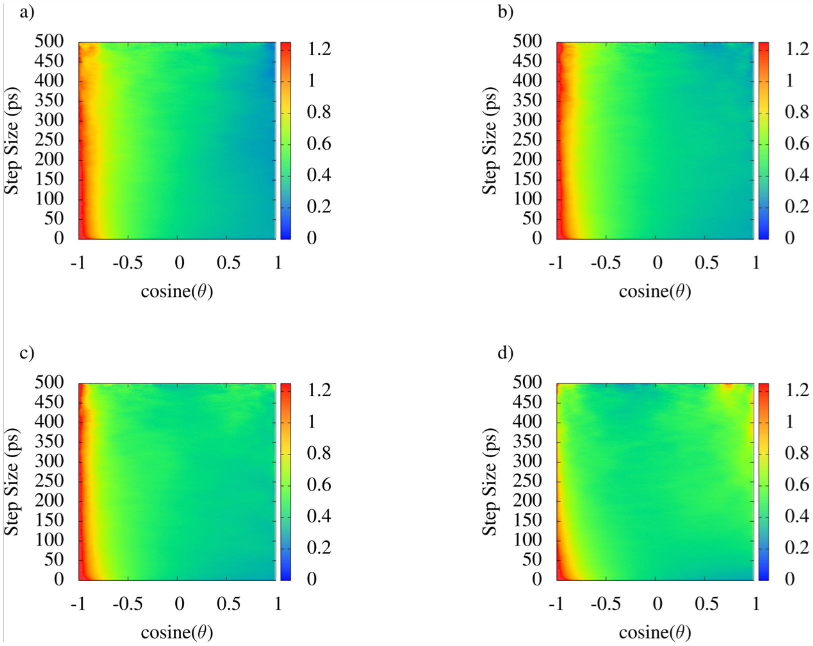

Figure 4-19: Joint probability distribution for the relative angle between two displacement vectors as a function of time step lengths for λ10 at 300 K. Each time-slice is normalized so that the integral of the distribution is set to 1.0. Note cosine(180°) = -1, cosine(90°) = 0.0, and cosine(0°) = 1.

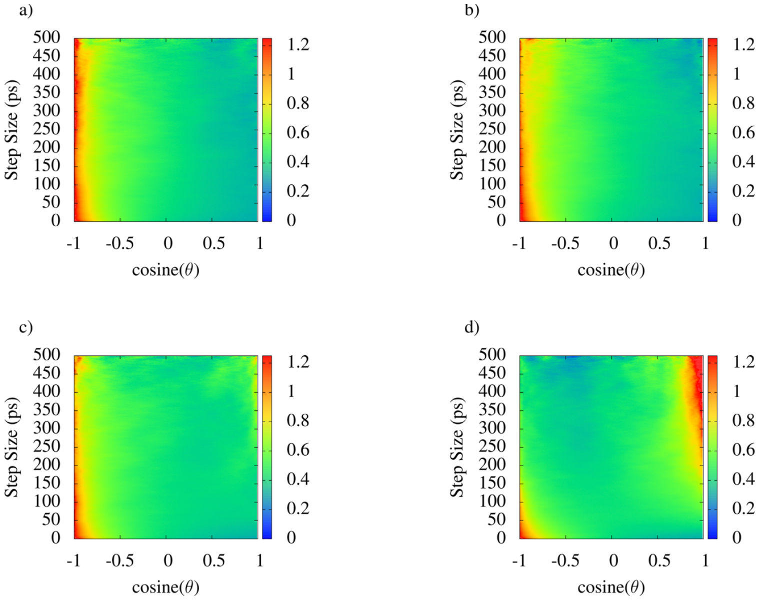

Figure 4-20: Joint probability distribution for the relative angle between two displacement vectors as a function of time step lengths for λ10 at 353 K. Each time-slice is normalized so that the integral of the distribution is set to 1.0. Note cosine(180°) = -1, cosine(90°) = 0.0, and cosine(0°) = 1.

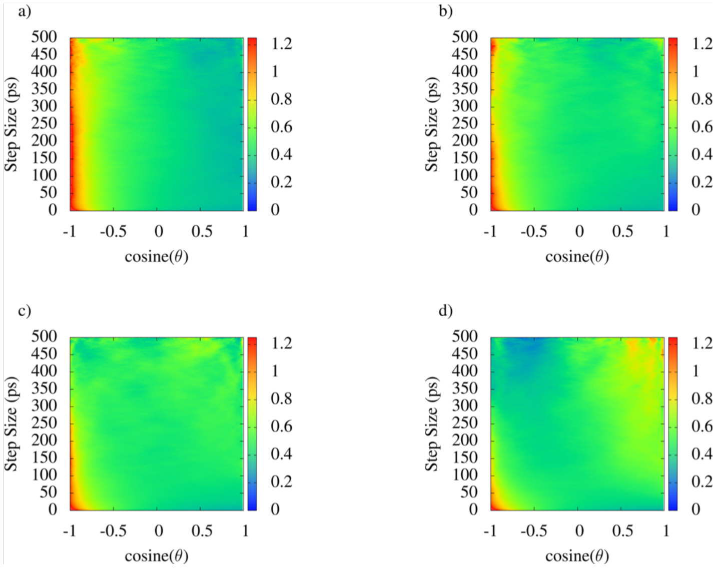

Figure 4-21: Joint probability distribution for the relative angle between two displacement vectors as a function of time step lengths for λ15 at 300 K. Each time-slice is normalized so that the integral of the distribution is set to 1.0. Note cosine(180°) = -1, cosine(90°) = 0.0, and cosine(0°) = 1.

Chapter 5: Minimal Experimental Bias on the Hydrogen Bond Greatly Improves Ab Initio Molecular Dynamics Simulations of Water

This chapter was reprinted with permission from *J. Chem. Theory Comput.* 2020, 16, 9, 5675–5684. Copyright 2020 American Chemical Society.

Abstract

Experiment Directed Simulations (EDS) is a method within a class of techniques seeking to improve molecular simulations by minimally biasing the system Hamiltonian to reproduce certain experimental observables. In a previous application of EDS to *ab initio* molecular dynamics (AIMD) simulation based on electronic density functional theory (DFT), the AIMD simulations of water were biased to reproduce its experimentally derived solvation structure. In particular, by solely biasing the O-O pair correlation function, other structural and dynamical properties that were not biased were improved. In this work, the hypothesis is tested that directly biasing the O-H pair correlation (and hence the H-O…H hydrogen bonding) will provide an even better improvement of DFT-based water properties in AIMD simulations. The logic behind this hypothesis is that for most electronic DFT descriptions of water the hydrogen bonding is known to be deficient due to anomalous charge transfer and over polarization in the DFT. Using recent advances to the EDS learning algorithm, we thus train a minimal bias on AIMD water that reproduces the O-H radial distribution function derived from the highly accurate MB-pol model of water. It is then confirmed that biasing the O-H pair correlation alone can lead to improved AIMD water properties, with structural and dynamical properties in even closer to experiment than the previous EDS-AIMD model.

I. Introduction

Ab initio molecular dynamics (AIMD) simulation[24] has become a popular tool to understand water (see, e.g., refs[36-38, 144]) and aqueous solutions/environments (see, e.g., refs[145-146]).

By using AIMD, as opposed to classical empirical water models, electronic structure calculations – primarily within the Kohn-Sham density functional theory (DFT) framework – can be used to solve for the electronic ground state. Electron densities can then respond to the surrounding electric field and thus account for polarization of the electron cloud, and forces can be calculated on-the-fly to propagate the dynamics of the nuclei. Furthermore, AIMD becomes particularly valuable for simulating systems while accounting for chemical reactivity, as it does not require specifying a defined bonding topology, and as such allows one to study dynamics of aqueous systems containing excess protons or hydroxide ions (see, e.g., refs[33, 51, 54, 62-63, 109]).

Accurately modeling the hydrogen bond between water molecules has proven challenging for AIMD water simulations that use generalized gradient approximations (GGA) such as PBE[25] or BLYP[26-27] as the exchange-correlation functional in the DFT.[32] GGA functionals result in over-polarization due to having a small energy gap between Kohn-Shan virtual orbitals and occupied orbitals,[28-29] and they also exhibit partial covalency (or charge-transfer) within the intermolecular interactions of water molecules.[30-32] These inaccuracies in modeling the hydrogen bond result in a water model that is overstructured at room temperature and diffusion coefficients that can be an order or orders of magnitude slower than found in experiment.[33-35]

It is common practice in the AIMD community to mitigate the deficiencies of GGA functionals by increasing the simulation temperature or by going beyond GGA functionals.[36-39] It has previously been shown for the PBE functional that simulation temperatures of 400 K are necessary to mimic room temperature structure and dynamics of water.[35, 147-148] It has been the case that increasing the temperature is not only an *ad hoc* remedy for the glassy behavior of GGA functionals, but additionally used to mimic nuclear quantum effects in GGA AIMD in an *ad hoc* fashion.[149] By contrast, going beyond simple GGA functions and using hybrid or meta-GGA functionals has been shown to improve the hydrogen bond properties and hence the water properties,[36, 39] but doing so significantly increases the computational cost by a factor of ~ 4 and ~ 20-50 in meta-GGA and hybrid functionals, respectively. It should also be noted that it is still commonplace to combine non-GGA functionals and increased simulation temperatures in AIMD as an *ad hoc* fix for nuclear quantum effects in room temperature water.[36-37]

One way to improve the accuracy of MD simulations (including AIMD) is to add a biasing potential to an observable of the system in order to improve agreement between that observable and one in target system. Pitera and Chodera showed using the method of Lagrange multipliers that there exists a linear bias on observables that minimizes the relative entropy of an ideal probability distribution for an observable to a target experimental one.[44] Using this idea, White and Voth developed the Experiment Directed Simulation (EDS) method as a means to parameterize these unknown linear terms in the Hamiltonian on-the-fly within a single MD simulation using a stochastic gradient descent algorithm.[41] Since then, there have been additional advances to EDS and similar methods,[150-151] and these have been recently reviewed by Amirkulova and White.[152] In related work, the Coarse-Grained Directed Simulation (CGDS) method was developed where coarse-grained observables in a molecular sub-system are biased based on data from coarse-grained simulations of a larger supramolecular complex.[42] In this work, the stochastic gradient descent algorithm of the original EDS method was unable to find coupling constants fast enough due to longer timescale and limited configurations of the CG observables that are otherwise available in isotropic systems such as water. In the CGDS paper, however, several variants of the learning algorithm were developed, where the stochastic gradient descent algorithm was replaced with a gradient descent using the covariance of all deviations of collective variables from target observables, and by a Levenberg-Marquadt minimization. In the studies presented here, we will take advantage of these more efficient methods which have better convergence properties.

In previous work,[43] we developed the idea that EDS could be applied to adjust the solvation structure of a relatively low cost DFT AIMD approach, rather than employing the previously mentioned alternatives of increasing the simulation temperature or going beyond GGA functionals. In that work[43] the solvation structure of BLYP and dispersion corrected BLYP water was biased to reproduce the experimental O-O radial distribution function (RDF). This EDS bias, henceforth known as "EDS-AIMD(OO)", was able to improve the targeted solvation structure of water without needing an increase of simulation temperature or computational cost. Importantly, other properties that were not biased also improved as a consequence of having a better O-O structure. For example, when adding an excess proton to the system, the EDS-AIMD(OO) approach improved the ratio of the hydrated excess proton to water diffusion coefficient and did not disrupt the other properties of the system. To confirm that employing EDS to a more accurate model would not adversely affect our results, the method was also tested on a dispersion corrected functional. It was found that, as expected, the linear bias learned from the gradient descent algorithm for the BLYP-D3 system was smaller than the EDS bias of normal BLYP due to the already better agreement with experiment for BYTP-D3, and all results for the biased EDS-BLYP-D3 model were equivalent or better.

The present work builds on this previous study, but this time by biasing the H-O...H hydrogen bond (intermolecular O-H coordination properties) as opposed to the oxygen coordination structure of water. We chose to pursue this approach due to the intuitive feeling that the having a correct description of hydrogen bonding in DFT water is the underlying deficiency leading to other poor properties, due to the over-polarization and anomalous charge transfer of GGA functionals. Correcting the hydrogen bond structure with EDS is more difficult than the O-O coordination, due to the anisotropic nature of hydrogen bonding, and the need to distinguish an O-H pair as either covalently bonded or hydrogen bonded. By biasing the hydrogen bond, however, we can more directly target the charge transfer and over-polarization found in GGA water simulations which, among other things, gives rise to its glassy behavior and slow diffusion. In this work, we thus bias BLYP and BLYP-D3 simulations to reproduce the O-H RDF of the highly and demonstrably accurate MB-pol water model,[153-156] which includes many-body interactions parameterized from high level CCSD(T) electronic structure calculations and many-body polarization effects. MB-pol accurately reproduces many properties of water and is gaining recognition as one of the most – if not the most – accurate water models available. By using the classical MB-pol O-H RDF as the refence in EDS-AIMD, we are therefore able to effectively include higher order correlations into the BLYP-level AIMD water simulations, while neglecting nuclear quantum effects. This enables us to bias BLYP and BLYP-D3 to achieve the best approximation to the (actual) Born-Oppenheimer potential energy surface for the classical nuclei and ensures that nuclear quantum effects could be subsequently accurately captured through, e.g., path-integral molecular dynamics simulation.

The remainder of this paper is organized as follows: In the Methods section, we first include a subsection that reviews the theory regarding the EDS method and how we apply it to bias the hydrogen bond. In the Determining EDS Coupling Constants subsection , we describe the details of the EDS algorithm as used, while in the Simulations Procedure subsection, we describe the simulation setup and details for the EDS learning algorithm and the production runs. In the Results and Discussion section, we then present the results and give further discussion. We lastly present conclusions and the outlook for the use of experimental-bias methods in AIMD.

II. Methods

A. Experiment Directed Simulation Method

EDS modifies the system Hamiltonian by adding a biasing potential that is parameterized to reproduce a target observable.[41] In the present case, the hydrogen bond is biased to reproduce the O-H radial distribution function (RDF) of the MB-pol water model at 298 K. As in the previous work, the RDF is corrected by biasing its statistical moments such as the coordination number (the zeroth moment). The bias on each moment is a function of three variables: a coupling constant, α_k, a function characterizing the pairwise distances between all hydrogen-oxygen pairs, $f_k(\vec{r}_{ij})$, and its target average value, $\hat{f}_k$. The EDS potential for each hydrogen atom is therefore:

$$V(r_i) = \sum_{k=0}^{M} \frac{\alpha_k}{\hat{f}_k} f_k(\vec{r}_{ij}) = \sum_{k=0}^{M} \frac{\alpha_k}{\hat{f}_k} \sum_{j=1}^{n_O} r_{ij}^{k} \left[1 - u(r_{ij} - r_0)\right], \tag{5.1}$$

where M represents the number of moments being biased, n_o is the number of oxygen atoms in the system, and we take $f_k(\vec{r}_{ij})$ to be a product of the O-H pairwise distance and mollified step function. The step function for biasing the hydrogen bond was chosen as:

$$1 - u(r_{ij} - r_0) = \begin{cases} \dfrac{1 - \left(\dfrac{r_{ij} - r_0}{w}\right)^{6}}{1 - \left(\dfrac{r_{ij} - r_0}{w}\right)^{12}}, & r_{ij} > r_0 \\ 1, & r_0 \geq r_{ij} > r_b \\ 0, & r_{ij} \leq r_b \end{cases} \tag{5.2}$$

where r_0 was set to 2.125 Å, w was set to 0.7, and r_b was set to 1.2 Å. This choice of step function was motivated by the desire to bias the hydrogen bond O-H interactions and not the covalent bond

O-H interactions. We set the EDS bias to be zero for all hydrogen-oxygen pairwise distance less than r_b = 1.2 Å, which is where the O-H RDF is zero. The r_0 was set to 2.125 Å to bias the trough between the first and second intermolecular peaks of the O-H RDFs peak as this gave final RDFs that best agreed with MB-pol. MB-pol's target values are its coordination numbers and moments determined by integrating MB-pols O-H RDF (Eq. 5.3).

$$\hat{f}_k = \rho \int_0^\infty dr\,[1 - u(r - r_0)] 4\pi r^{2+k} g_{OH}(r) \tag{5.3}$$

In Eq. 5.3, ρ is the number density, $1 - u(r - r_0)$ is the same mollified unit-step function as Eq. 5.2, and $g_{OH}(r)$ is the target O-H radial distribution function. Note that by k$^{\text{th}}$ moment we are specifically referring to the power in Eq. 3, and the zeroth moment corresponds to the coordination number.

B. Determining EDS Coupling Constants

The determination of EDS coupling constants to bias the hydrogen bond characterized by these AIMD potentials was nontrivial and required improvements to the EDS learning algorithm to improve the rate of convergence of EDS parameters and collective variables (CVs).[42] EDS learns the coupling constants during the progression of a simulation where the coupling constants at time segment $\tau + 1$ are updated similar to a stochastic gradient descent algorithm

$$\boldsymbol{\alpha}_{\tau+1} = \boldsymbol{\alpha}_\tau - \boldsymbol{\eta}_\tau \left(\Delta\boldsymbol{\alpha}_\tau \cdot \left(\frac{\partial \Delta\boldsymbol{\alpha}_\tau}{\partial \boldsymbol{\alpha}_\tau} \right) \right) = \boldsymbol{\alpha}_\tau - \boldsymbol{\eta}_\tau \boldsymbol{\delta}_\tau, \tag{5.4}$$

where $\boldsymbol{\eta}_\tau$ is the learning rate, $\boldsymbol{\delta}_\tau$ is the step size, and $\Delta_k\alpha_\tau = \langle f_k(\boldsymbol{r})_\tau \rangle - \widehat{f_k}$, and bold font represent vectors. Each time segment is set for a predefined period of simulation timesteps by the user, and should be about double the autocorrelation time of its corresponding collective variable.

Our current implementation of EDS uses the learning rate of White and Voth, and is calculated as

$$\eta_{\tau}^{k} = \frac{A_k}{\sqrt{\sum_{\mathrm{j}=1}^{\tau}\left(\delta_j^k\right)^2}}, \tag{5.5}$$

where A_k is the maximum value a coupling constant can change. The step size includes a derivative term that is proportional to the covariance of the collective variable error at time τ. With $f_i = \langle f_i(\boldsymbol{r})_\tau\rangle - \widehat{f_i}$:

$$\left(\frac{\partial \Delta \boldsymbol{\alpha}_\tau}{\partial \boldsymbol{\alpha}_\tau}\right)_{ij} = -\mathrm{Cov}_\tau\left(f_i, f_j\right) = -\langle f_i f_j\rangle + \langle f_i\rangle\langle f_j\rangle_{\mathrm{ij}} \equiv \bar{\bar{J}}_{ij} \tag{5.6}$$

In Ref. [42], the Levenberg-Marquardt (LM) algorithm was implemented, replacing the derivative term in eq 5.4 by:

$$\left(\frac{\partial \Delta \boldsymbol{\alpha}_\tau}{\partial \boldsymbol{\alpha}_\tau}\right) = \left[\bar{\bar{J}}^{\mathrm{T}}\bar{\bar{J}} + \lambda_\tau \mathrm{diag}\left(\bar{\bar{J}}^{\mathrm{T}}\bar{\bar{J}}\right)\right]^{-1}\bar{\bar{J}}^{\mathrm{T}} \tag{5.7}$$

where $\mathrm{diag}(\bar{\bar{J}}^{\mathrm{T}}\bar{\bar{J}})$ is a purely diagonal matrix with elements of $\bar{\bar{J}}^{\mathrm{T}}\bar{\bar{J}}$, and λ_τ is known as a mixing parameter which can tune the style of the step size. In this work, the LM algorithm is used to determine the coupling constants for EDS-BLYP and EDS-BLYP-D3 AIMD simulations.

Table 5-1: Algorithm Parameters and Simulations Settings. All Simulations used the LM algorithm with a mixing parameter of 0.1 with an EDS period of 25 fs.

System	Init Bias (Coordination, 2nd Moment, kcal/mol)	Target Values (Coordination 2nd Moment, Å^2)	A (k_BT)	EDS Sim Length (ps)
BLYP 1	(0,0)	(1.62, 3.86)	300	50
BLYP 2	(0,0	(1.62, 3.86)	300	90
BLYP 3	(0,0)	(1.62, 3.86)	100	40
BLYP-D3 1	(0,0)	(1.62, 3.86)	200	100
BLYP-D3 2	(0,0	(1.62, 3.86)	200	120
BLYP-D3 3	(0,0)	(1.62, 3.86)	100	25

C. Simulation Procedure

EDS was used to bias the coordination and 2nd moment of the O-H (hydrogen bond) RDF. EDS was applied to three independent trajectories of 128 water molecules in a cubic simulation box with box length set to 15.64 Å. All AIMD simulations were done with the quick-step module in CP2K[87] version 3.0 with a modified version of PLUMED2[157] based on version 2.5 available from the Voth Group GitHud (https://github.com/uchicago-voth) under the 'eds-virial-oh' branch using Goedecker-Teter-Hutter (GTH) pseudopotentials[89], a TZV2P basis set with a plane-wave cutoff of 400 Rydbergs, and with BLYP[26-27] exchange correlation functional or BLYP with D3 Grimme dispersion corrections,[85-86] with a timestep of 0.5 fs. Coupling constants were determined in the constant NVT ensemble using three Nosé-Hoover chains at 298 K and with a time constant of 3000 cm^{-1}. EDS simulations were run until the CVs were determined to be converged, see Table 5-1 for details. After this point, the coupling constants were fixed and simulations continued in the constant NVT simulations for 10-15 ps to equilibrate the system with the fixed coupling constant.

Finally, production EDS-AIMD runs in the constant NVE ensemble were performed for 80 ps and 40 ps for BLYP and BLYP-D3 simulations, respectively. As a comparison, single BLYP and BLYP-D3 AIMD simulations were run in the constant NVE ensemble for 80 ps and 40 ps, respectively. All dynamical and static properties were obtained from simulations in the constant NVE ensemble and averaged over all three trajectories. Except for the RDFs and unless otherwise noted, our analysis scripts were used to analyze a single MB-pol trajectory consisting of 256 water molecules in the constant NVE ensemble for 50 ps to compare with our results.

III. Results and Discussion

By examining Figure 5-1a, we can see that biasing the hydrogen bond with EDS can greatly improve the O-H RDF of BLYP. In fact, we see the first peak has nearly perfect agreement with the MB-pol reference, and the structural properties past the first peak come into closer agreement with MB-pol. Additionally, by biasing the hydrogen bond in BLYP water, we see greater improvements in the O-O RDF (Fig. 5-1b) and the H-H RDF (Fig. 5-1c). As shown in the O-H RDF, we see that the first peak in these other RDFs come into nearly perfect agreement with MB-pol, even though these other properties were not biased but they are still improved due to their strong correlations with the hydrogen bond. We note that the hydrogen bond EDS bias is targeting the close-range interactions between O-H pairs within a hydrogen bond. It should also be noted, however, that EDS greatly improves the structural properties past the first peak in all three RDFs (Fig. 1a-c), although not perfectly.

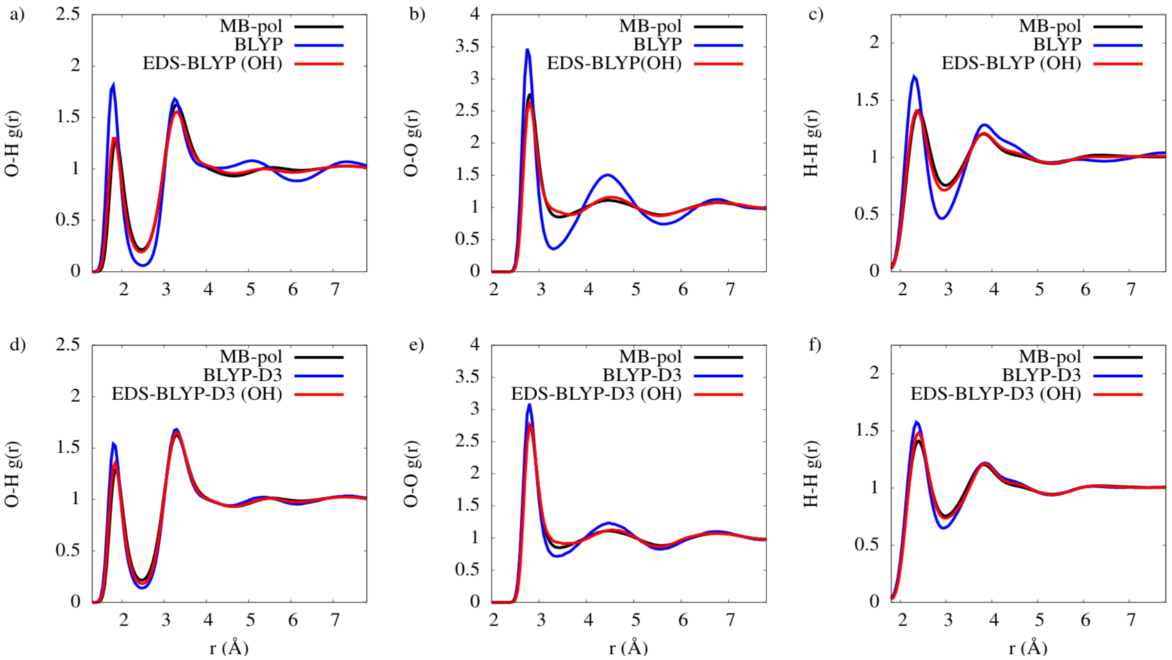

Figure 5-1: Radial distribution function for both BLYP (a-c) and BLYP-D3 simulations (d-f). In black we show the RDFs of the classical MB-pol water model, in blue is either the BLYP or BLYP-D3 RDFs for O-H (a and d), O-O (b and e), or H-H (c and f), and in red is the RDF that results from using EDS to bias the hydrogen bond in BLYP or BLYP-D3 simulations. These RDF are averages over three independent EDS trajectories.

An improvement is also seen in the structural properties of dispersion corrected BLYP (BLYP-D3) over uncorrected BLYP when we bias the hydrogen bond with EDS. Similar to biasing the hydrogen bond in BLYP water simulations, we see that biasing the hydrogen bond in BLYP-D3 water simulations leads to RDFs whose first peaks nearly perfectly reproduces the first peaks in MB-pol (Fig 5-1d-f). Again, we emphasize that only the hydrogen bond is biased in these EDS-AIMD simulations, and any improvements in other structural properties arise due to strong correlations with the hydrogen bond collective variable. The advantage of biasing BLYP-D3 over BLYP water simulations can be found in the second peaks of the O-H RDF and O-O RDF; where these second peaks reproduce MB-pol's structure. This indicates that EDS is not a substitute for dispersion corrected DFT but complements it.

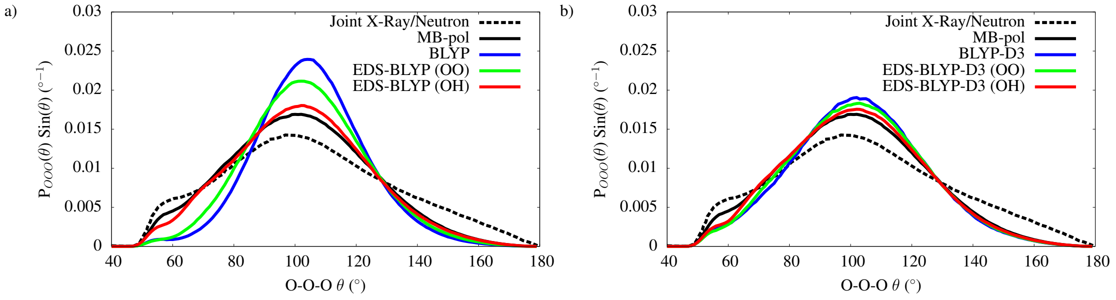

Figure 5-2: Oxygen-Oxygen-Oxygen triplet distribution function. (a) shows the distribution function from BLYP, EDS-BLYP (OO), and EDS-BLYP(OH). (b) shows the distribution function from BLYP-D3, EDS-BLYP-D3 (OO), and EDS-BLYP-D3 (OH). Solid black line shows the triplet distribution function of MB-pol in the NVE ensemble using 25,000 configurations of 256 water molecules, and dashed black line shows the Joint X-Ray Neutron distribution[158] traced from Ref. [36], blue line shows the unbiased BLYP or BLYP-D3, green line shows the distribution from using EDS to bias the solvation structure, and red line shows the distribution function from using EDS to bias the hydrogen bond. Each distribution was normalized such that integral of P(θ)*sin(θ) was set to 1.

We further examined the structural properties by calculating the oxygen-oxygen-oxygen (O-O-O) triplet probability function to characterize the tetrahedrality of the water structure. For a central oxygen atom, all 3-body oxygen angles were calculated for O-O pairwise distances less than 3.22 Å, which is the radial distance where the coordination number is ~ 4. We see that in both the BLYP (Fig. 5-2a) and BLYP-D3 (Fig. 5-2b) cases, the unbiased simulations have a large probability above 100°, which is typically attributed to a strong tetrahedral ordering. By using EDS to bias the simulations, we see a decrease in both the biased BLYP and BLYP-D3 plots that is very close to MB-pol, with the most prominent improvement arising from biasing the hydrogen bond (OH) instead of the solvation structure (OO). Also, the peak around 55° in Figure 5-2a is captured with the OH bias [EDS-BLYP(OH)] but the solvation structure bias [EDS-BLYP(OO)] is unable to capture it. However, MB-pol does an overall better job at reproducing the experimental peak around 55° as MB-pol is explicitly parameterized to reproduce 3-body interactions. Nevertheless, by biasing the hydrogen bond in BLYP and BLYP-D3 simulations, as opposed to biasing the solvation structure (the O-O RDF), we can obtain O-O-O triplet distribution that are in better agreement with MB-pol and experimental data, despite the fact that the O-O-O distribution was not biased directly. We note that nuclear quantum effects are not included in any of these EDS-AIMD or MB-pol results shown here, but they are of course present in the experimental data.

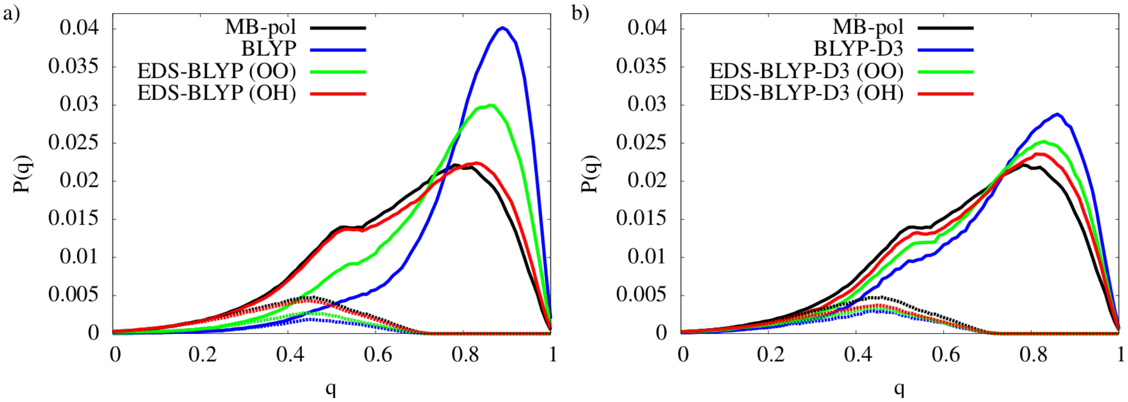

Figure 5-3: Tetrahedral order parameter probability distribution function. (a) shows the distribution function from BLYP, EDS-BLYP (OO), and EDS-BLYP(OH). (b) shows the distribution function from BLYP-D3, EDS-BLYP-D3 (OO), and EDS-BLYP-D3 (OH). Black line shows the triplet distribution function of MB-pol in the NVE ensemble using 25,000 configurations of 256 water molecules, blue line shows the unbiased BLYP or BLYP-D3, green line shows the distribution from using EDS to bias the solvation structure, and red line shows the distribution function from using EDS to bias the hydrogen bond. Solid lines correspond to the total distribution while dashed lines represent oxygen atoms that have one O-O-O angle less than 61°.

We also considered the solvation structure of oxygen atoms by calculating the tetrahedral order parameter[159] (q) distribution in the simulations. The tetrahedral order parameter is determined according to

$$q = 1 - \frac{3}{8}\sum_{i=1}^{3}\sum_{j=i+1}^{4}\left(\cos\theta_{ij} + \frac{1}{3}\right)^2 \tag{5.8}$$

where θ_{ij} is the O_i-O-O_j angle centered on a given oxygen, the sums are over the 4 closest oxygens around the given oxygen, and a value of 1 indicates a perfect tetrahedral structure.[159] The solid lines in Fig. 5-3a and 5-3b show the tetrahedral order parameter distribution for the BLYP and BLYP-D3 simulation methods, respectively. In similar fashion as the O-O-O distribution, we find that BLYP and BLYP-D3 simulations have a larger probability of tetrahedral structuring, but that the inclusion of both EDS-AIMD(OO) and EDS-AIMD(OH) bias weaken the interactions. Again, the EDS-AIMD(OH) bias does a better job than the EDS-AIMD(OO) bias to create a probability distribution that is in better agreement with MB-pol, and therefore likely with experiments. To understand the solvation structure of central oxygens that give rise to the peak around 55° in Figure 5-2, we further decomposed the tetrahedral order parameter distribution. The dashed lines in Fig. 5-3 correspond to oxygen atoms that have at least one O-O-O angle less than 61°. This distribution indicates that oxygens atoms with these small O-O-O angles have very low tetrahedrality and distorted hydrogen bond structures. We find that by using the EDS-AIMD(OH) we further weaken the hydrogen bonds beyond the EDS-AIMD(OO) bias to be in better agreement with MB-pol (see discussion below).

Table 5-2: Final Results for EDS-AIMD Simulations. For comparison, we show dynamical values for MB-pol, EDS-BLYP(OO), BLYP, and BLYP-D3 trajectories. MB-pol diffusion coefficients were taken from Ref. 157. EDS-BLYP(OO) diffusion coefficients were taken from Ref. [43]. ϑ_D is the standard deviation for diffusion constant. BLYP time constants show a mono-exponential decay even when fitting with a bi-exponential. $\tau_1$and $\tau_2$are time constants obtained via bi-exponential fits of the hydrogen bond ACF (Fig. 5-4).

Simulation	${}^{\alpha_0}/_{f_0}$ (kcal/mol)	${}^{\alpha_2}/_{f_2}$ (kcal/mol Å^2)	D (Å^2/ps)	ϑ_D (Å^2/ps)	τ_1 (ps)	τ_2 (ps)	Ave. Temp (K)
MB-pol	-	-	0.23	0.02	0.41	4.95	-
BLYP	-	-	0.01	0.01	-	20.22	317.32
EDS-BLYP(OO)	-	-	0.06	0.02	0.85	11.61	-
EDS-BLYP(OH) 1	387.80	-70.53	0.139	0.002	0.31	6.11	290.48
EDS-BLYP(OH) 2	421.52	-69.88	0.167	0.001	0.58	6.06	297.872
EDS-BLYP(OH) 3	299.57	-60.94	0.186	0.003	0.33	4.75	302.96
BLYP-D3	-	-	0.06	0.05	0.79	13.45	302.88
EDS-BLYP-D3(OH) 1	285.87	-36.93	0.152	0.008	0.12	5.38	298.82
EDS-BLYP-D3(OH) 2	237.26	-35.16	0.118	0.003	0.59	7.49	294.80
EDS-BLYP-D3(OH) 3	218.75	-31.59	0.146	0.002	0.32	6.40	293.06

Another goal in biasing the hydrogen bond in BLYP and BLYP-D3 AIMD water simulations was to see an improvement in the dynamics. The self-diffusion coefficient of BLYP water has been reported to be an order (or orders) of magnitude slower[33-35] than that found in experiment (0.23 Å^2/ps).[160] In the AIMD simulations reported here, the BLYP water oxygen self-diffusion coefficient was found to be 0.01 ± 0.01Å^2/ps, and with an improvement to 0.06 ± 0.05 Å^2/ps for the dispersion corrected BLYP-D3 water simulations. The unbiased BLYP-D3 water diffusion is the same as using EDS to bias the O-O solvation structure of BLYP water [EDS-

BLYP(OO)] at 0.06 ± 0.02 Å^2/ps.[43] (The diffusion coefficient of EDS-BLYP-D3(OO) water was not calculated in that work.) On the other hand, biasing the hydrogen bond (O-H RDF) in EDS-BLYP(OH) and EDS-BLYP-D3(OH) water improves the self-diffusion coefficient to be 0.164 ± 0.004 Å^2/ps, and 0.139 ± 0.009 Å^2/ps, respectively. This is much closer to experiment (0.23 Å^2/ps), and significantly larger than using the O-O RDF solvation structure for EDS bias.[43]

It has also been shown that dynamical properties in MD simulations with periodic boundary conditions can suffer from finite-size effects.[161] To address these effects on the diffusion coefficient of EDS-AIMD(OH) simulations, we extrapolated the diffusion coefficient to infinite dilution using this equation:

$$D(\infty) = D(L) + \frac{\xi k_B T}{6\pi\eta L}, \tag{5.9}$$

where k_B is Boltzmann's constant, T is the simulation temperature, $D(L)$ is the diffusion coefficient in a simulation box dimension, L, η is the viscosity experimental value,[162] and ξ is a constant value set to 2.837 297 for cubic simulation boxes. The size-corrected diffusion coefficient at infinite dilution is thus found to be 0.208 ± 0.005 Å^2/ps and 0.183 ± 0.009 Å^2/ps for EDS-BLYP(OH) and EDS-BLYP-D3(OH), respectively. (We note that the addition of nuclear quantum effects would likely increase the EDS-AIMD diffusion results even more, bringing them into even better, perhaps even nearly perfect, agreement with experiment.) One can also confirm that the increased diffusion is not a result of a spurious increase in simulation temperature (see Table 5-2).

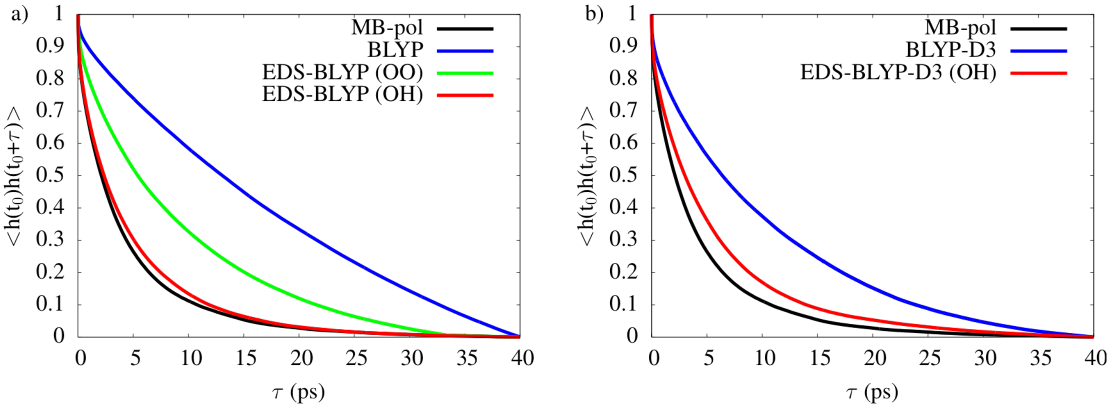

Figure 5-4: Hydrogen Bond autocorrelation function (ACF). (a) shows the ACF from MB-pol, BLYP, EDS-BLYP (OO), and EDS-BLYP(OH). (b) shows the ACF from MB-pol, BLYP-D3, and EDS-BLYP-D3(OH). Black line shows MB-pol, blue line shows the unbiased BLYP or BLYP-D3, green line shows EDS-AIMD(OO), and red line shows EDS-AIMD(OH). The hydrogen bond ACF comes from averaging over the first 40 ps of the simulation. The hydrogen bond ACF for EDS-BLYP-D3(OO) was not included due to the more limited statistical sampling in that prior work. Time constants from a bi- exponential fit of these curves can be found in Table 2.

The increased diffusion coefficient of EDS-BLYP(OH) and EDS-BLYP-D3(OH) over BLYP, dispersion corrected BLYP-D3, and even EDS-BLYP(OO) results from directly targeting the hydrogen bond with a bias in BLYP water. This physical improvement is further emphasized by the hydrogen bond autocorrelation function results in Figure 5-4 and the hydrogen bond 2D Potential of Mean Force (PMF) in Figure 5-5. The autocorrelation function is taken over all pairs and all times, and a hydrogen bond is defined as having an O-O distance of less than 3.5 Å and an H-O-O angle less than 30°, and the 2D PMF is calculated from

$$F(r,\theta) = -k_B T ln\big(P(\theta,r)\big) + C, \tag{5.10}$$

where C is a constant chosen to set the minimum of the free-energy to 0.0 kcal/mol. Biasing the hydrogen bond clearly does a better job at breaking hydrogen bond correlations than does simply biasing the O-O solvation structure; this behavior additionally contributes to the observed larger diffusion for the O-H EDS biased AIMD simulations over the O-O EDS biased ones (see Table 5-2). Additionally, by biasing the hydrogen bond, we see a broadening in the hydrogen bond PMF compared to unbiased simulations which further reduces the glassy behavior observed in AIMD simulations.

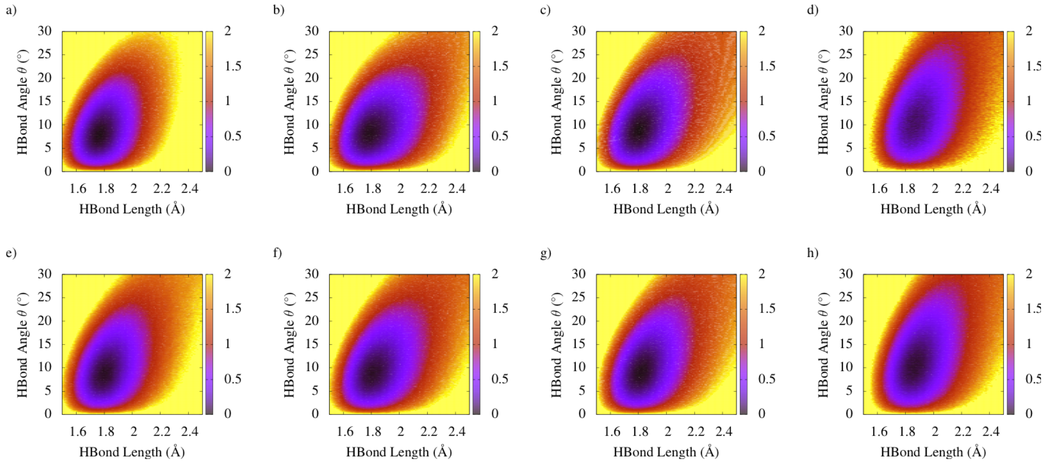

Figure 5-5: Hydrogen Bond Potential of Mean Force (PMF) using eq 5.10 for (a) BLYP, (b) EDS-BLYP(OO), (c) EDS-BLYP(OH), (d) MB-pol in NVT ensemble, (e) BLYP-D3, (f) EDS-BLYP-D3 (OO), (g) EDS-BLYP-D3(OH), and (h) MB-pol in the NVE ensemble. The PMF is in units of kcal/mol.

It is valuable and interesting to look at the form of the bias potential learned by the EDS algorithm in order to reproduce the first peak in the O-H RDF (in this case, the MB-pol target result). In our previous implementation of EDS to bias the O-O solvation structure in BLYP and BLYP-D3 water,[43] the EDS biasing potential added an effective repulsive force to the oxygen-oxygen pair interaction, with the EDS-BLYP-D3(OO) adding a smaller force magnitude than the EDS-BLYP(OO) since the former is closer to the target RDF result. In the present cases, since dispersion corrected BLYP-D3 water simulations more closely match the accurate reference MB-pol results, we expect the EDS potential and force for EDS-BLYP-D3(OH) to be a smaller overall in magnitude than for EDS-BLYP(OH).

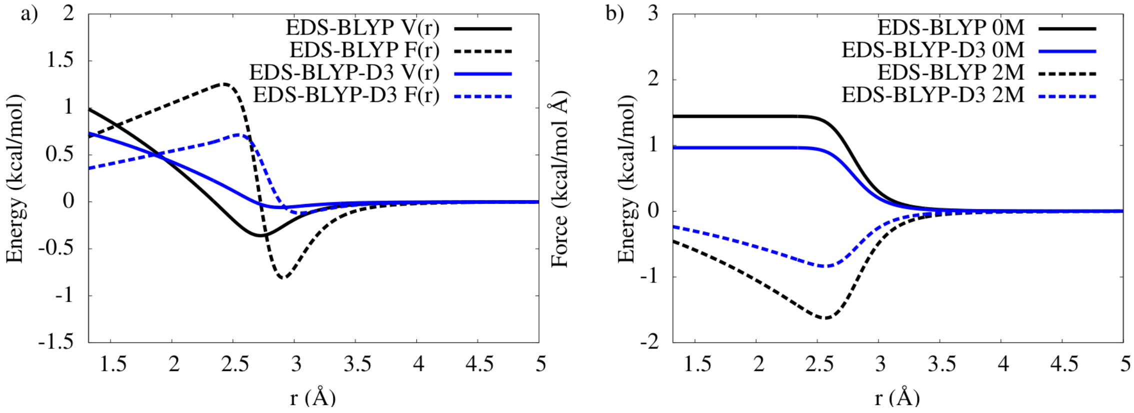

Figure 5-6: Potential energy and force plots for the EDS O-H bias. Black lines are for EDS-BLYP(OH) and blue lines are for EDS-BLYP-D3 OH) simulations. (a) The average potential energy and force for the EDS-BLYP (OH) and EDS-BLYP-D3 (OH). Solid lines indicate the EDS potential while the dashed lines indicate the EDS force. (b) The EDS bias as separated into its 0th and 2nd moment components. Solid lines are for the 0th moment contribution to the EDS potentials, and the dashed lines are for the 2nd moment contributions to the EDS potentials.

In Figure 5-6a we show the EDS potential (solid) and force (dashed) for EDS-BLYP(OH) and EDS-BLYP-D3(OH) simulations. The EDS bias in both cases has a repulsive “ramp” at short distances, which is followed by a potential energy well at larger distances. This indicates that using EDS to bias the hydrogen bond is not as simple as adding a repulsive bias between the pairs as was found when biasing the O-O solvation shell.[43] The EDS-BLYP potential has a sharper repulsive wall and deeper attractive well than the dispersion corrected EDS-BLYP-D3 case, which results in stronger repulsive and attractive force magnitudes. We also separated the EDS potentials into the 0th and 2nd moment contributions in Figure 5-6b. It is seen in both moments that the EDS-BLYP potential has larger magnitudes than EDS-BLYP-D3, which adds additional explanation for the differences in the EDS-BLYP and EDS-BLYP-D3 potentials in Fig. 5-6a.

IV. Conclusions

In this work, the Experiment Directed Simulation (EDS) method has been implemented to bias the O-H hydrogen bond in BLYP and BLYP-D3 AIMD water to reproduce a target O-H RDF of the highly accurate MB-pol model (taken as the “exact” result). The rationale for this EDS bias is that most GGA-level DFT functionals result in hydrogen bonds that are too strong and hence AIMD water at 298 K that is over structured and much too slowly diffusing. By biasing only the hydrogen bond correlations, we were able to improve other structural properties and provide a very significant improvement in the water self-diffusion coefficient. Biasing the hydrogen bond opposed to the O-O solvation structure directly targets the over-polarization and charge transfer present in GGA DFT to obtain a better AIMD water model, and produces superior dynamical properties as shown in the prior text and Supporting Information. We note that once the EDS bias is determined, this results in the addition of only a classical correction term and hence negligible change to the computational cost of the AIMD.

Future work will investigate the application of these EDS-AIMD(OH) simulations to more complex environments as the present work is limited to bulk water simulations at the experimental density. Specifically, GGA-level AIMD simulations in the constant NpT ensemble have been shown to underestimate the experimental water density,[163-164] and future work will investigate the predicted density of these EDS-AIMD(OH) models. Recent developments of the EDS algorithm have, for example, also included the virial pressure[152] in determining EDS coupling constants and should prove to be valuable in future work. Additionally, these EDS-AIMD(OH) simulations may require further modification for air-water interfaces,[165-166] as an order parameter dependent EDS bias such as local density[167] might be required to better apply the EDS bias to O-H pairs that have differing solvation structures at the air-water interface than in the bulk-like regions.

An overall advantage of AIMD is it can also account for chemical reactions. This becomes particularly useful for simulating the hydrated excess proton or hydroxide, which diffuses through the Grotthuss mechanism.[14-15, 168] In previous work,[43] we also implemented an EDS-AIMD O-O solvation structure bias to simulate AIMD water having an excess proton added to it, making the approximation that such a bias is still appropriate for the water solvent even once an excess proton is introduced into the system. It was found that such an approximation is quite accurate (and it is expected to be even more accurate for any system in which a solute or solutes are chemically more distinct from the water solvent). On the other hand, the same approximation cannot be simply implemented in the O-H EDS bias approach taken in this paper. This is because the EDS-AIMD hydrogen bond bias applies forces to all pairs of hydrogens and oxygens within the specified cutoff distances, but one would not want to apply this bias to any special hydrogens considered as part of a hydronium or hydroxide ion complex. Thus, in future work we plan to rigorously combine the EDS-AIMD hydrogen bond bias into a continuous potential for the hydrated excess proton (by combining EDS with a bond order analysis) in such a way that forces are applied to only select classes of hydrogens and oxygens. Such a result can also likely be generalized to other forms of chemical reactions in EDS-AIMD(OH) water in which the water participates in the chemistry. This research is currently in progress.

Appendix A: Discussion on the Choice of Biased Moments

We used EDS to bias the 0th and 2nd moment of the O-H RDF in AIMD simulations. In this discussion, we show that it is not necessary to bias the 1st moment in these simulations to reproduce the O-H RDF of MB-pol

In Figure 5-7 we show the 0th (biased), 1st (unbiased), and 2nd (biased) moments in the constant NVE ensemble of the various simulation methods used in this study. We first note that both the 0th moment and 2nd moment in the EDS simulations are much closer to the target value than the unbiased simulations Additionally, we find the 1st moment is much closer to the target value without a direct bias due to the strong correlations between the moments. This seems to suggest that directly biasing the 1st moment is not necessary to improve its distribution.

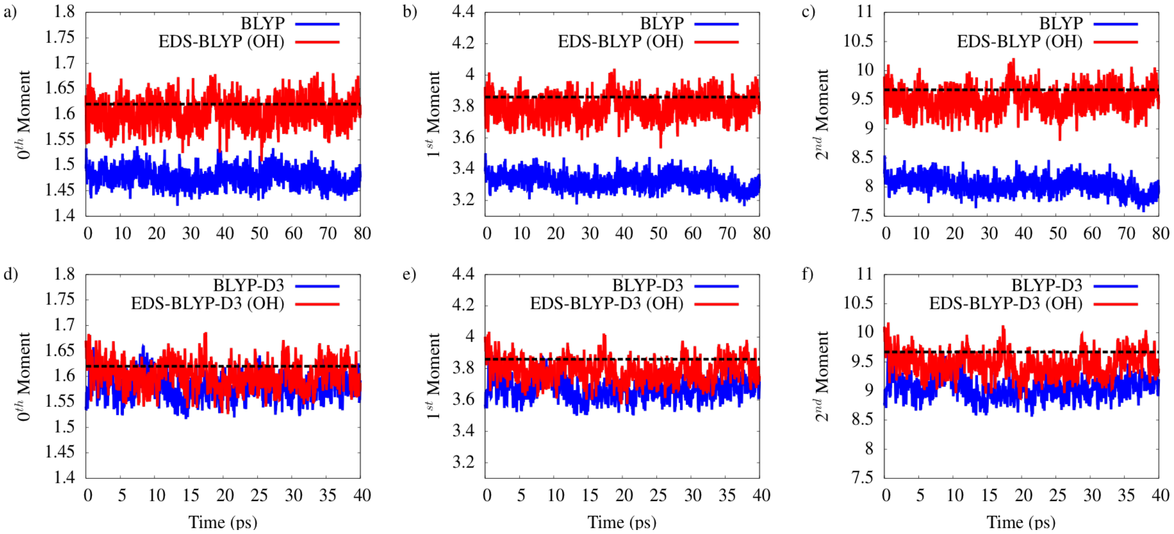

Figure 5-7: 0th, 1st, and 2nd moments of the O-H coordination number for BLYP (a-c) and BLYP-D3 (d-f) simulations in the NVE ensemble. We show the unbiased simulations in blue, the EDS biased simulation in red, and the target value for the collective variables with a dashed line. Only the 0th and 2nd moment were biased in the EDS simulations.

We also found that including the 1st moment into the EDS learning algorithm had a negligible effect on the resulting EDS potential energy. In Figure 5-8, we show the EDS-BLYP (OH) potential energy that results from biasing the 0th and 2nd moment, and the resulting EDS-BLYP (OH) potential after a 30 ps learning simulation where the 0th, 1st, and 2nd moments were biased. We see excellent agreement between the two potential energy functions except at short distances where there is very little O-H probability. Including the 1st moment only broadens the coupling constant values but does not affect the resulting EDS potential.

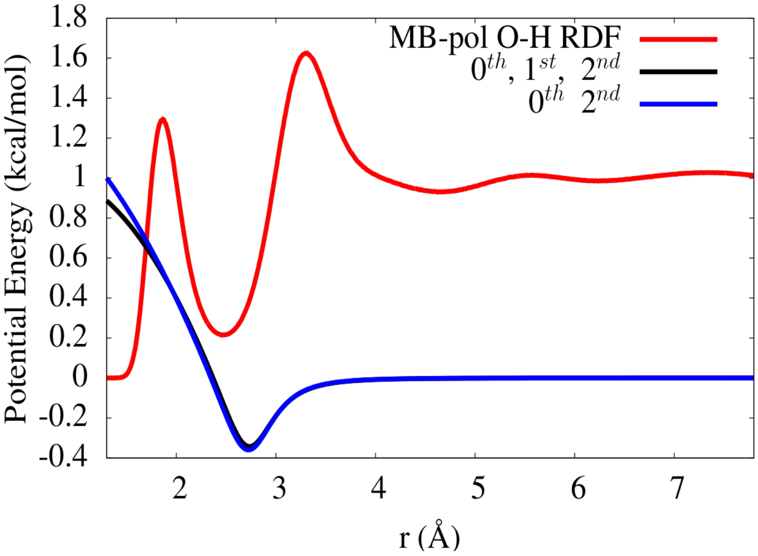

Figure 5-8: EDS potential energy resulting from biasing the 0th, 1st, and 2nd (black) and the 0th and 2nd (blue) moments. The MB-pol O-H RDF is present in red.

Appendix B: Calculation of the EDS Potential and Force

The EDS potential for a given pairwise distribution is defined in the main text as the product of the coupling constant (α_k/f_k) and the H-O pairwise function. (See Eq. 5-1). In practice, the PLUMED2 EDS module calculates the mean pairwise distribution over all O-H pairs and subtracts the target value from this mean value. The EDS bias is then the product of this difference and the coupling constant. Although this changes the potential, the forces remain unchanged due to the target values being a constant value. In the main text (Fig 5-4) and the Appendix B (Fig. 5-19), we chose to present the EDS potential between a single O-H pair using Eq. 5.10, where we have not subtracted the target value from the pairwise distribution, and have removed any dependence on the number of hydrogen bonds in the system. We show in Fig. 5-9 the corresponding EDS potential and force plots where the target value is subtracted from the pairwise function. EDS potential plots are the average over all three EDS simulations and the EDS force plots are calculated using finite difference of the potential.

$$V(r_{ij}) = \frac{\mathbf{1}}{n_{HBonds}} \sum_{k=0}^{M} \frac{\alpha_k}{\hat{f}_k} \cdot r_{ij}^{k}\left[1 - u(r_{ij} - r_0)\right], \tag{5.11}$$

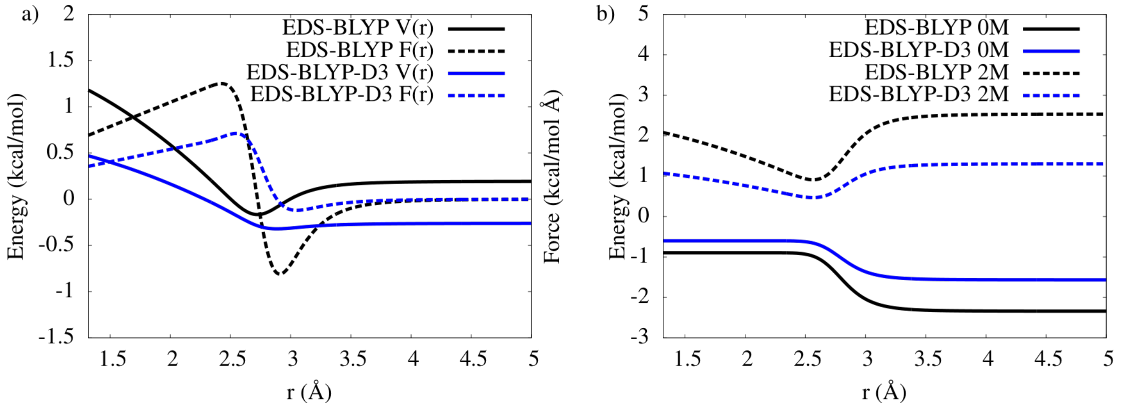

Figure 5-9: Potential energy and force plots for the EDS bias where the target value is subtracted from the pairwise distribution. Black lines are for EDS-BLYP (OH) and blue lines are for EDS-BLYP-D3 (OH). (a) shows that average potential energy and force for the EDS-BLYP (OH) and EDS-BLYP-D3 (OH). Solid lines indicate the EDS potential while the dashed lines indicate the EDS force. (b) The EDS bias is separated into its 0th and 2nd moment components. Solid lines are for the 0th moment of the EDS potential, and dashed lines are for the 2nd moment of the EDS potential.

Appendix C: Physical Properties not Described in the Main Test

Potential of Mean Force (PMF) for the O-H and O-O pair-wise distance calculated via equation 5.12. Here k_B is Boltzmann's constant, T is the temperature of 298 K, and $g(r)$ is the corresponding radial distribution function.

$$F(r) = -k_B T \ln(g(r)) \tag{5.12}$$

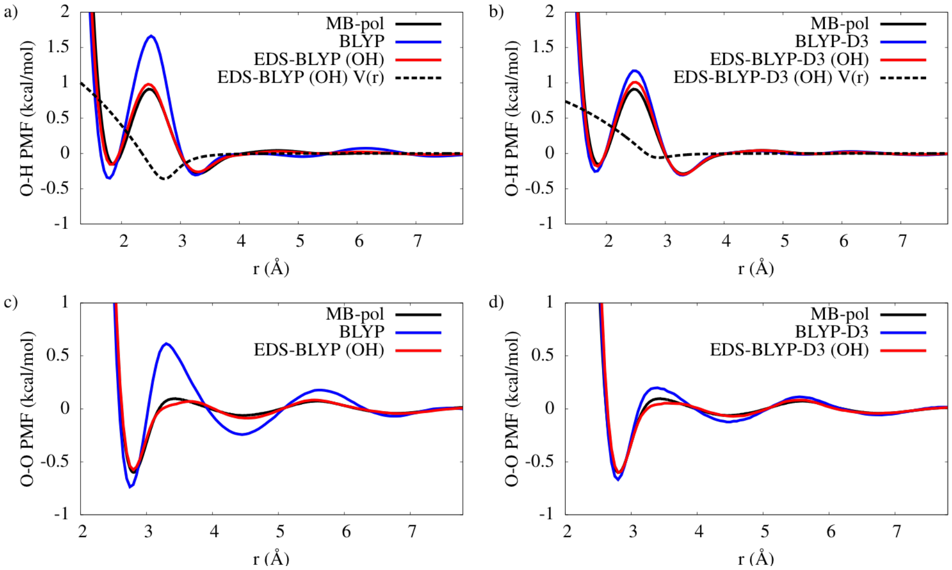

Figure 5-10: Potential of Mean Force (PMF) calculated from Equation 5.12. (a) and (b) show the PMF of the O-H pair distribution for BLYP and BLYP-D3 simulations, respectively. (c) and (d) show the PMF of the O-O pair distribution for BLYP and BLYP-D3 simulations, respectively. MB-pol is represented by a solid black line, blue corresponds to BLYP or BLYP-D3 AIMD, red line corresponds to the EDS corrected BLYP or BLYP-D3 AIMD simulations. (a) and (b) additionally show the hydrogen bond EDS bias in dashed black line. The mean EDS bias calculated using the coupling constants in Table 5-1 and Equation S1.

Chapter 6: Investigation of the Proton Transfer Mechanism and the Contribution to Diffusion with Ab Initio Molecular Dynamics

Abstract

We have performed a series of novel analyses on *ab initio* molecular dynamics (AIMD) simulations of an excess proton in water to quantify the relative occurrence of concerted hopping events and rattling events, and thus further elucidate the mechanism of proton transport in water. We compare both the effect of temperature and the introduction of an experimentally directed bias used to correct for the overstructuring in AIMD water. We find that in all simulations, concerted hopping events do occur, but that the majority of events are the product of proton rattling, where the excess proton will rattle between two or more waters. The results are consistent with the proposed special-pair dance model of proton transfer, wherein the acceptor water molecule will quickly change, but the donating water molecule remains constant for some time until finally a decisive hop occurs. To remove the misleading effect of rattling, we applied a filter to the trajectory such that hopping events that were followed by back hops to the original water are not counted. We found a steep reduction in the number of multiple hopping events when the filter was applied, suggesting that many multiple hopping events that occur in the unfiltered trajectory are the product of rattling. Comparing the continuous correlation function of the filtered and unfiltered trajectories, we find reasonable agreement with experimental values for the proton hopping time and Eigen-Zundel interconversion time, respectively.

I. Introduction

Proton transfer is an important chemical process fundamental to a number of systems within the fields of biology, chemistry, materials science, and engineering. Such systems include the proton pumping mechanisms within cellular membrane proteins[3, 11, 169-170] and proton exchange membranes (a common fuel cell material),[5, 124, 171] the efficient functionalities of which rely on rapid proton transport. Unlike other cations, the transport of a proton in aqueous media relies on two distinct mechanisms: vehicular transport and Grotthuss shuttling, i.e., proton hopping from hydronium ions to neighboring water molecules.[46, 52, 54, 66-67, 172-175] The ability of a proton to hop between neighboring waters allows the charge center to diffuse without substantial displacement of nuclear coordinates and greatly increases the proton self-diffusion constant.

In order to fully understand the mechanism of proton transport in experimental systems, a comprehensive and physically rigorous theoretical framework is necessary. Given the unique character of proton transport – i.e. involving bond rearrangement – any such description must necessarily incorporate proton transfer from hydronium ions to neighboring water molecules. Since bond breaking and formation is fundamentally a quantum mechanical process involving the rearrangement of electrons, it is natural to employ *ab initio* methods to investigate the proton hopping mechanism. Despite years of interest from many research groups, there is a still considerable debate regarding the nature of the proton transfer mechanism. The importance of multiple, concerted hops as a driver of efficient diffusion in particular has remained contentious.

Much of the debate is centered around the true nature of a solvated excess proton; that is, whether it is most accurately described as existing as an Eigen cation, $H_9O_4^+$,[176] or a Zundel cation, $H_5O_2^+$.[18] Dominance of single hopping involves the conversion of the Eigen cation into a transient Zundel cation and back, resulting in transfer of a proton from one H_3O^+ ion to another.[19, 173] Conversely, some early simulations suggested direct conversion of one Zundel ion into another, resulting in a double hop.[52, 69-71] Pioneering work by Parrinello and co-workers[54] suggested both the Eigen and Zundel are limiting structures, and the excess proton is actually in a state of flux between them. Nevertheless, this work found that proton transfer was dominated by single proton transfer events from one hydronium core to another.

Much of the debate around the proton hopping mechanism has focused on the importance of the first solvation shell of the hydronium ion. Early work suggested that due to the reduced coordination of a hydronium ion relative to that of a water molecule (three in hydronium vs. four in water),[51-52, 173] proton transfer is driven by cleavage of one of the hydrogen bonds (HB) donated to the proton acceptor and by the subsequent formation of an additional hydrogen bond to the proton donor. In fact, Tuckerman et al. found that in hopping events which resulted in charge displacement – i.e. neither rattling nor a special pair dance – involved the *concerted* cleavage and formation of these hydrogen bonds.[177] In this mechanism, the cleavage of a HB donated to the proton acceptor happens first, followed by formation of a HB donated to the donor (often within 50 fs); this particular order does not occur in every hopping instance. On the other hand, it has been shown that the average coordination of bulk water is around 3.9, whereas that of water in the first solvation shell of the hydrated proton is around 3.6.[47, 178] This suggests that cleavage of a HB donated to the acceptor water molecule is not the rate limiting step. Work by Voth et al. showed that by examining the O^*-H_w radial distribution function (where the asterisk denotes atoms belonging to hydronium ions), proton transfer was facilitated by the presence of a fourth water donating a hydrogen bond to the top of the oxygen atom of the hydronium ion.[33] Consistent with the results of Tuckerman, it was found that charge diffusion was enhanced in regions of the trajectory in which this water was present, resulting in burst and rest periods characteristic of AIMD.

In an analysis of multi-scale empirical valence bond (MS-EVB) trajectories, Voth, Agmon, and co-workers found the proton transport process involves even more steps than the formation and cleavage of two hydrogen bonds. It was found that the first solvation shell water nearest to the hydronium ion rapidly shifts; this is termed the special pair dance, and in this process, the hydronium is "choosing" which water to donate the proton to.[20] Additional work by Voth and Agmon suggests the collective motion of the first two solvation shells in determining which of the waters the proton is ultimately donated to.[19] This analysis involves comparing both the relative bond lengths of hydrogen bonds between first and second solvation shell waters, as well as formation and cleavage of bonds hydrogen bonds between these layers. Therefore, rather than be dictated by just a few atoms or molecules, the proton transfer process involves upwards of twenty waters. This, coupled with the sizable duration of the special pair, indicates that single hops should dominate proton hopping events, as the extensive solvation structure simply cannot react fast enough to accommodate multiple hops.

In a recent paper, however, Hassanali and co-workers argued that the formation of water wires is abundant in bulk water, resulting in periods with bursts of activity.[62] This has been observed in many AIMD studies, and the authors of Ref. [62] argue that proton transfer occurs in concerted hopping events over several waters, and is dominated by double hops. More recently, Wu and co-workers observed similar behavior.[63] The authors argued that AIMD simulations of an excess proton in water were overwhelmingly dominated by correlated double hopping events, leading to rapid diffusion.

The arguments in Ref. [63] that double hops dominate proton transfer contradicts many of the results seen previously. We have therefore re-evaluated a set of AIMD simulations in an attempt to further clarify the role of single hops and concerted double hops in proton transport. In this paper, we use several analyses to count and assess the abundance of multiple hopping events relative to the total number of events.

The organization of the paper is as follows: in Section II we briefly discuss the simulation details; in Section III we discuss the analysis methods employed, as well as the resulting data; and in Section IV we present a collective discussion of the results and provide our conclusion on the presence and important of multiple hops.

II. Simulation Details

The results presented below are based on duplicate sets of the four simulation setups: AIMD at 300 K, AIMD at 330 K, and EDS-AIMD (OO) at 300 K, and EDS-AIMD (OH) at 300 K. EDS-AIMD is an *ab initio* method where the simulation has been biased to match experimental data, hence the name EDS: experimentally directed simulation.[43] In EDS-AIMD (OO), a bias is applied such that the O_w-O_w RDF in a pure water system is reproduced; it has been found that this bias does not distort the solvation structure of a hydronium ion.[43, 179] In EDS-AIMD (OH),[180] a bias is applied such that the O_w-H_W RDF reproduces that of classical MB-pol water,[153-156] and forces were applied continuously between any O-H pairs;[181] details of this methodology will be presented in a following publication. Inclusion of AIMD simulations at 330 K was motivated by the fact that all the simulations in Ref. [63] were run at that temperature. Each of the calculations used the BLYP exchange-correlation functional,[182-183] with the Grimme dispersion correction.[184-185] Each simulation used a triple-zeta basis set to describe the valence electrons, and a Goedecker-Teter-Hutter pseudopotential. The simulations were equilibrated for at least 20 ps in the constant NVT ensemble using the particular AIMD method and temperature of the target simulation. Finally, duplicate production runs of the systems in the NVE ensemble were run for 80 ps. The timestep used for the simulations was 0.5 fs. All AIMD simulation were run using the CP2K software package, and the EDS-AIMD simulations used the EDS extension within PLUMED.

III. Results

A. Hopping

There are many ways in which one could count the number of single and multiple hopping events, and we thus present the hopping behavior of a hydrated proton in water using three counting methods as described below. In accordance with the work in Ref. [63], we have chosen the relevant time scale of 500 fs. To eliminate double counting, we scan the trajectory, looking to maximize the number of hops in a given block of length 500 fs. Again, in keeping with the work in Ref. [63], we tabulate the number of hops in segment lengths of 10 ps. We note that in each counting method, if the proton hops from water A to water B, then back to water A, this is not considered a hop.

In Method 1, we scan the trajectory for the largest number of hops within 500 fs, and if we find an *n* hopping event in that 500 fs range, we don't scan that region of the trajectory again. We essentially tile the trajectory with blocks 500 fs long in which there are the most number of many hopping events. That is, we scan for $n = 10$, $n = 9$, … , $n = 1$.

Method 2 is very similar to Method 1, but segment lengths of 500 fs are not required. For example, suppose that at the end of a 500 fs block, there were 3 hops. Now suppose that the third hop occurred at, say, 350 fs into that 500 fs block. Then the "tile" pertaining to the $n = 3$ event is just the first 350 fs. Thus, this region cannot contribute to any other hopping events, but the latter 150 fs is free to contribute to another hopping event.

Method 3 is a slight modification which highlights most favorably multiple hopping events. Again, consider a 500 fs block in which the final number of hops at the end of the block is $n = 3$. Now suppose that in this block, there was a point at which $n = 4$ before some subsequent back-hop, and say this hop which resulted in $n = 4$, albeit fleetingly, occurred 250 fs into the block. We now tile the first 250 fs with $n = 4$, and leave the remaining 250 fs open to contribute to other hopping events. We recognize that what seem like favorable multiple hopping events may be nullified by a subsequent back-hop, but Method 3 seeks to find the most favorable multiple hopping situation.

The results for the above analysis methods are shown in Fig. 6-1. One can argue the number of single hops in each of the analysis methods is overestimated as a result of the tiling technique used. For example, consider two tiles that are nearly adjacent, with a narrow portion of the trajectory separating the two. This small portion of the trajectory is naturally going to be limited in the number of hops it contains as a result of its limited size. We recognize this complicates the description of single hops, but as we disagree with the conclusion that multiple hops dominate, we set out to be as generous to multiple hopping events as possible.

The results show several interesting trends. First, as expected, there is an increase in the number of multiple hops as one moves from Method 1 to Method 2 to Method 3. This is clearly a result of a more generous tiling scheme, allowing for more multiple hopping events and more events with many hops. Another notable feature is the substantial increase in multiple hopping events when the temperature of AIMD simulations is increased from 300 K to 330 K. This is somewhat unsurprising as the free energy barrier for proton transfer of AIMD at 330 K is marginally lower than that of AIMD at 300 K (Appendix A, Fig. 6-9), and the increased thermal energy should further make the transition from one water to another easier. It is also interesting that EDS-AIMD, run at 300 K, produces an intermediate number of multiple hops. Again, given the slightly lower proton transfer barrier, one could expect a slightly larger number of hops.

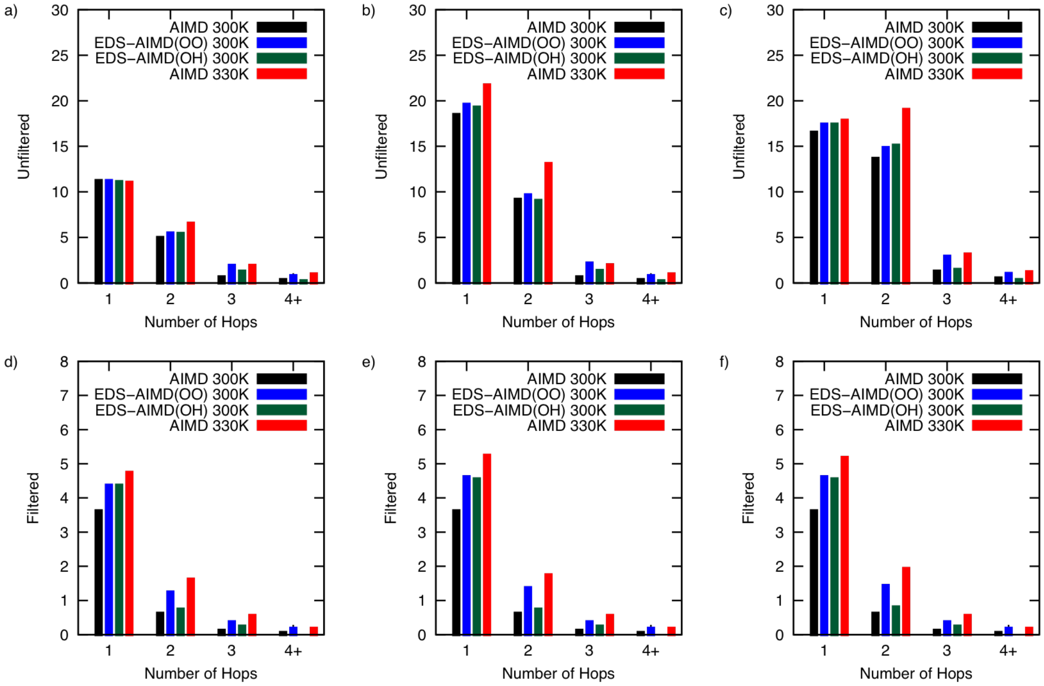

Figure 6-1: Number of occurrences of different hopping method for the unfiltered (a-c) and filtered (d-f) trajectories. The numbers reported are averages of 10 ps fragments of the trajectory.

AIMD water is known to be overstructured,[186-187] and this can result in rapid proton transfer, as neighboring waters are especially ready to receive an excess proton. On the other hand, it has been shown that cleavage of hydrogen bonds in the first and even second solvation shells of the Eigen complex directly impact the proton transport mechanism. Thus, overstructuring may prevent waters from adopting a configuration capable of receiving a transferred proton. Given that

EDS is designed explicitly to reduce the structure of water, and elevating the ionic temperature of a simulation from 300 to 330 K would naturally have such an effect, it is possible that the disruption of the water hydrogen bond network in fact makes back-transfer more difficult.

One of the obvious limitations of the above analysis is that it can be corrupted by back-hopping (i.e. situations in which a proton hops from water A to water B, and then back to water A). We note that back-hopping is quite common in AIMD simulations, and results in proton rattling between two waters. Consider an example in which the proton back-hops before immediately hopping forward. If we label the waters alphabetically in terms of forward hopping, this would look something like A → B → A → C, where A → B is the initial forward hop, B → A is the back hop, and then A → C is another forward hop (note that waters B and C are equivalent in the forward hopping chain). The above analysis could pick out the sequence B → A → C as a double hop, even though a back hop is required to make the double hop possible. Our analysis could also pick out hopping events that are immediately followed by a back hop, again overemphasizing high *n* events.

For the purpose of this analysis, we have applied a filter to the trajectory that mitigates the effect of rattling by smoothing out such events. If a proton hops from A to B, and then back to A, we consider the proton to have remained on A the entire duration. The only exception to this is if the proton remains on B for 500 fs or more, in which case we consider B to be a stable hydronium, rather than just a fleeting hydronium. To illustrate the effect of this filter, we show an example of the filtered and unfiltered forward hopping of an AIMD simulation at 300 K in Fig. 6-2 (the effect of the filter is the same for all the simulations, so we show just one example; analysis of all trajectories can be found in Appendix A, Fig. 6-10). Comparing the forward hopping of the filtered and unfiltered trajectories, we see the clear elimination of a vast proportion of hops, and within the context of concerted hopping, a majority of concerted hops are eliminated. Notice that even in the filtered trajectory there is some apparent rattling – our filter will only eliminate first order rattling; that is, if the proton hopping goes forward and back as in A → B → C → B → A – a term we will call the "slingshot" effect – the filter will only trim the trajectory of the hop to C, resulting in A → B → A.

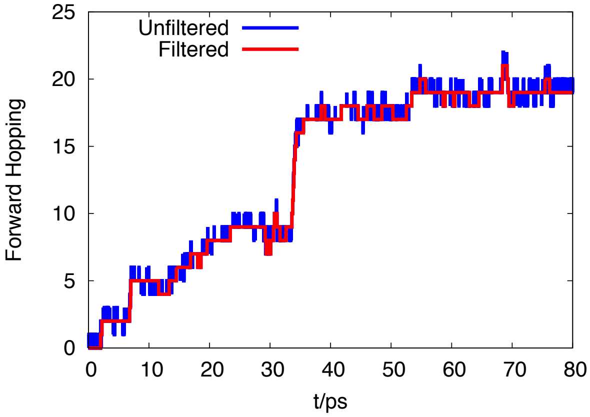

Figure 6-2: Forward hopping index as a function of time for the unfiltered (blue) and filtered (red) trajectories.

We ran the above hop counting techniques on the filtered trajectories, and found a dramatic reduction in the number of single and multiple hopping events in all three methods. This is unsurprising based on the fact that we have eliminated the "slingshot" effect mentioned above, and therefore trimmed the maximum number of effective hops. However, it is somewhat surprising how drastically the number of hops is reduced. Comparing the relative numbers of single hops to multiple hops again suggests the dominance in single hopping events. We again concede the possibility of overcounting single hops as a result of "bumping" against a tile. Nonetheless, if the prevalence of multiple hops seen in the unfiltered trajectory were genuinely concerted, and not some artifact of the slingshot effect, then we would expect to see most of the multiple hopping events maintained in the filtered trajectory. This is not the case, based both on the results of the analysis and simple visual inspection of the forward hopping plot shown in Fig. 6-2.

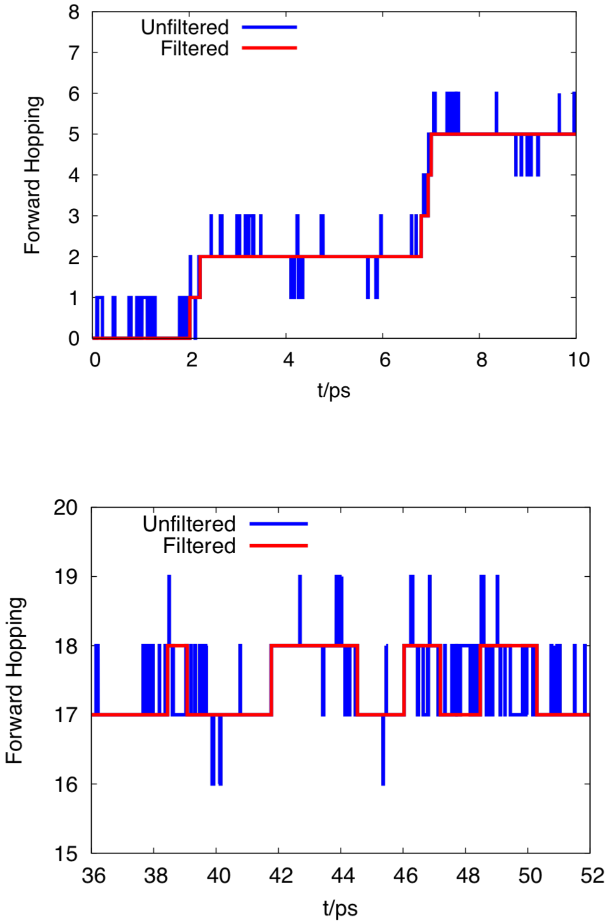

Figure 6-3: Segments of the filtered and unfiltered trajectories of AIMD at 300 K showing the effect of slingshotting.

As in the above analysis, we find that after applying the filter, there is still a strong temperature dependence on the number of concerted hops: AIMD simulations at 330 K have a much higher propensity for double hops (and higher order hopping events) than AIMD at 300 K. This suggests one must take caution when interpreting results of simulations at higher temperatures. We also see an intermediate number of double hops in the EDS-AIMD simulations between AIMD at 300 K and AIMD at 330 K.

Another striking feature of this data is that the majority of hopping events are single hopping events. That is, when one eliminates rattling and slingshotting, one eliminates what we argue had been mistakenly categorized as concerted hops. To illustrate this point, consider the zoomed in region of the AIMD forward hopping plot shown in Fig. 6-3, showing the forward hopping in the first 10 ps of the simulation. Consider the hopping event at around 2 ps. The filtered trajectory in red shows an unambiguous double hopping event. The unfiltered trajectory shows some rattling, a double hop, and then some more rattling. There is a point at which there is a net $n = 3$ event, but this is mitigated by a near-immediate back hop. It is clearly nonsensical to assign this to a triple hopping event, considering that the third hop is so quickly nullified. One advantage of using the filtered trajectory is that it allows easy visual inspection and verification. Our analysis also relates a reasonable number of hopping events relative to the forward hopping. In the example trajectory shown in Fig. 6-3, there are 1037 total hops, the net forward hopping is only 20. It therefore seems unreasonable to mistakenly consider the system to be undergoing constant concerted hopping.

We also calculated the forward hopping that occurs in the 0.5 ps immediately following a hopping event; that is, when a hopping event occurs, what is the net relative forward hopping 0.5 ps later. Of the 1037 total hopping occurrences, 43% of the hopping occurrences had the proton return to the same position in the forward hopping chain; 21% of the hopping occurrences had the proton one position forward; and 4% of the hopping occurrences the proton was two positions forward. Only 6% occurrences had the proton two or more positions forward after 0.5 ps. (The other occurrences are attributed to net negative forward hopping after a hopping event.) When we run the same analysis on the individual simulation with the fastest diffusion, AIMD at 330 K having proton self-diffusion constant of 2.07 Å^2/ps, we do find more forward hopping and concerted hopping, but not in such a way as to suggest the dominance of concerting hopping. In this particular run at 330 K, there were 1435 total hopping events; in 34% of those, the proton was at the same forward hopping position 0.5 ps later; in 26% the proton was one position ahead; in 11% the proton was two positions ahead; and in 14% the proton was two or more positions ahead. That is, the proton only moves forward in a concerted way around 14% of the time.

We will not discuss each individual hopping event in the trajectory shown in Fig. 6-3, but it is instructive to elaborate on another specific region in the trajectory. Consider the region of the forward hopping plot of the AIMD trajectory at 300 K between 36 and 52 ps. In the unfiltered trajectory (Fig. 6-3), there are a number of clear hopping events, and even a few hopping events that could be construed as double hops. However, it is clear, looking at the forward hopping of both the filtered and unfiltered trajectories, that essentially no forward hopping is occurring, and therefore it would be unreasonable to assign any of the action as a multiple hopping event. Indeed, incessant rattling is most prominent in AIMD simulations at 300 K, but such periods of apparent activity that are accompanied by no forward hopping do occur in simulations run with AIMD at 330 K and EDS at 300 K, though in AIMD at 330 K extensive periods of inactivity are rare.

To more directly compare with the analysis in Ref. [63], we have also implemented the following scheme for counting the number of hops. The number of hops in a concerted hopping event is incremented as the proton hops to a new water; if the proton back hops, the previous hop is nullified; a concerted hopping event is concluded if the proton remains on a water for 0.5 ps.

This protocol is taken from Ref. [63]. As can be seen from the unfiltered forward hopping plot in Fig. 6-2, the proton essentially never sits on a water for 0.5 ps (and we make no effort to analyze the unfiltered trajectory in this way). We therefore run our analysis on the filtered trajectory. We note that Ref. [63] makes no mention of filtering in the specific way that we do, but the authors do state they eliminate counting of rattling events by considering a proton that has returned to its original water within 0.5 ps not to have hopped. We reiterate that protons so infrequently stay on a single water for 0.5 ps, and that rattling precedes nearly every hopping event (though not exactly all), thus necessitating the use of the filtered trajectory.

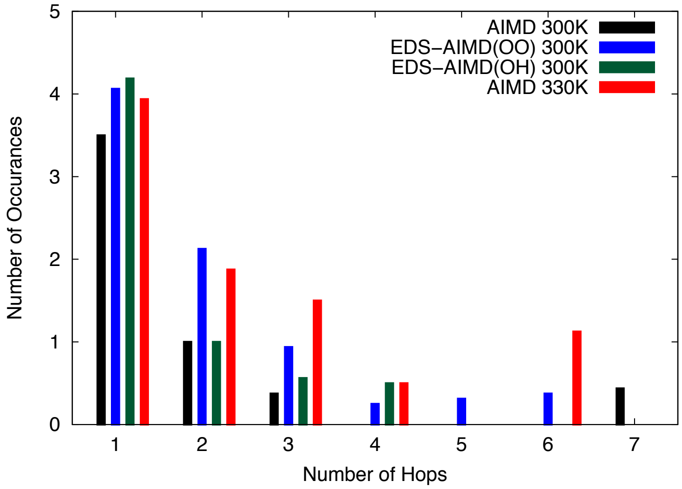

Figure 6-4: Analysis of hopping event using the method described in Ref [63]. Due to the fact that there are so few segments in which a proton stays on a single water for 0.5 ps, results shown are only for the filtered trajectory. Number of Occurrences are averaged over 10 ps segments of the trajectory.

To present our data as consistently with Ref. [63], we scale the number of n hopping events by n: if there are 10 double hops, we plot $2 \times 10 = 20$ (we note this is what was done in Ref. [63]).

The results of this analysis are shown in Fig. 6-4. By using the filtered trajectory, we again find a dramatic reduction in the number of multiple hops, and by imposing the condition that the proton must remain on the same water for 0.5 ps to conclude a single or multiple hopping event, there are simply fewer total events. We note that we did not plot *n* = 0 events, in which a proton sits on a single water for 0.5 ps; this is a result of filtering out rattling events, as such a scenario is virtually never the case in an unfiltered trajectory.

In accordance with the abundance of single hopping events is the relative lack of multiple hopping events in comparison to Ref. [63], despite having implemented a protocol very similar to what they report, though admittedly our filter may have disrupted an apples to apples comparison. Multiple hopping events are most significant in AIMD at 330 K, with the largest number of multiple hopping events coming in the form of double and triple hops. We do see a similar number of double hops in EDS-AIMD (OO) at 300 K, and an appreciable number of higher order multiple hops, but fewer than in AIMD at 330 K. We find few multiple hopping events in AIMD at 300 K, though interestingly there is one *n* = 7 hopping event. We note that AIMD with BLYP functional is excessively glassy, and simulations can vary greatly. In fact, one of our AIMD runs at 300 K shows very little forward hopping over the course of the simulation.

B. Correlation Functions

In order to further compare the hydronium lifetimes of the different simulation methods, as well as inspect the effect of eliminating rattling, we calculated the proton identity correlation function and the continuous proton identity correlation function of the filtered and unfiltered trajectories. We first present the proton identity correlation functions, shown in Fig. 6-5, where the proton identity correlation function is defined as,

$$c(t) = \frac{\langle h(t)h(0)\rangle}{\langle h\rangle}$$

where $h(t)$ is 1 if it is equal to $h(0)$, and 0 if it is not. Comparing the correlation functions of the four simulation methods, we see a more rapid decay in the hydronium ion in AIMD at 330 K than AIMD at 300 K. This is consistent with the behavior of more rapid hopping and a higher fraction of multiple hops (which take the excess proton farther away from $h(0)$). We find that EDS-AIMD (OO) and EDS-AIMD (OH) has a decay behavior more similar to AIMD at 330 K than at 300 K. The correlation functions of the filtered trajectories do not differ in spirit from those of the unfiltered trajectories (Appendix A, Fig. 6-11), but some of the details have been smoothed over.

The more drastic difference is in the so-called continuous proton correlation function, defined

$$C(t) = \frac{\langle H(t)H(0)\rangle}{\langle H\rangle}$$

where $H(t)$ is 1 as long as the hydronium identity has not changed from that of $H(0)$ and 0 once it has changed. Since rattling will drastically reduce the amount of time before the hydronium identity changes, there is a substantial change in the continuous proton correlation function when

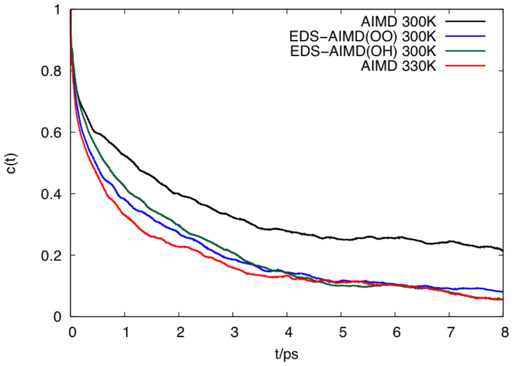

Figure 6-5: Proton correlation function of the four computational methods studied here.

one compares the unfiltered and filtered trajectories. First, we compare the continuous proton correlation function of the unfiltered trajectories, shown in Fig. 6-6. Integrating the correlation functions yield lifetimes of 184 fs for AIMD at 300 K, and 145 fs for EDS-AIMD (OO) at 300 K, 174 fs for EDS-AIMD (OH) at 300 K, 114 fs for AIMD at 330 K. These values are similar to those found by Tuckerman and co-workers.[177] In that paper, the authors note that this is similar to the experimental Eigen-Zundel interconversion time of around 100 fs. We again find EDS shows intermediate behavior between AIMD simulations at 300 K and at 330 K.

Calculating the continuous correlation function on the filtered trajectories of course yields very different results. Eliminating rattling removes fleeting hydronium states, and thus extends the apparent lifetime of a particular hydronium. Therefore, the decay of the correlation function is much longer, as shown in Fig. 6-6. We see similar trends as before, where AIMD at 330 K and EDS-AIMD at 300 K decay more rapidly than AIMD at 300 K. Integrating the continuous correlation functions of the filtered trajectories yields lifetimes of 1.69 ps, 1.09 ps, 1.45 ps, and 850 fs for AIMD at 300 K, EDS-AIMD (OO) at 300 K, EDS-AIMD (OH) at 300 K, and AIMD at 330 K, respectively. The authors of Ref. [177] argue this corresponds to the experimental hopping time of around 1.5 ps.[56, 173] We note that if this interpretation is correct, EDS-AIMD (OH) at 300 K yields results most in line with experiment.

Importantly, the similarity of the integrated lifetimes to well-defined experimentally measured timescales suggest the analysis method is sensible for separating short- and long-term proton transfer behavior. One would expect that the unfiltered trajectory, which is dominated by rattling events, should reflect the transition time from the Eigen complex to the Zundel complex. Likewise, upon elimination of rattling, the lifetimes should reflect the true hydronium lifetime –

that is, the amount of time before an excess proton truly moves on from one water to another. Given the relative numbers of total hops in the unfiltered and filtered trajectories, and the vast difference in the number of hops counted by our analyses from those in Ref. [63], we find it difficult to believe that a correlation function of their "filtered trajectory" would yield something close to what our data saw. Granted, we expect the number of total hops of their unfiltered trajectories to be similar to ours, but find their counting method to be contrary to what we see.

We acknowledge that one potential shortcoming of the analysis presented, in particular in the analysis of the filtered trajectory, is the overemphasis on forward hopping. Our analysis does count certain back-hops, but the smoothing of rattling events has the clear impact of decreasing multiple hops that include back-hops in favor of mostly counting hops that result in a clear, long-lasting proton transfer event. We argue that in order to assess the part of the proton transfer mechanism which actually results in dislocation of the proton and therefore accounts for the rapid diffusion, it makes sense to separate rattling events. Certainly, rattling is an essential part of the

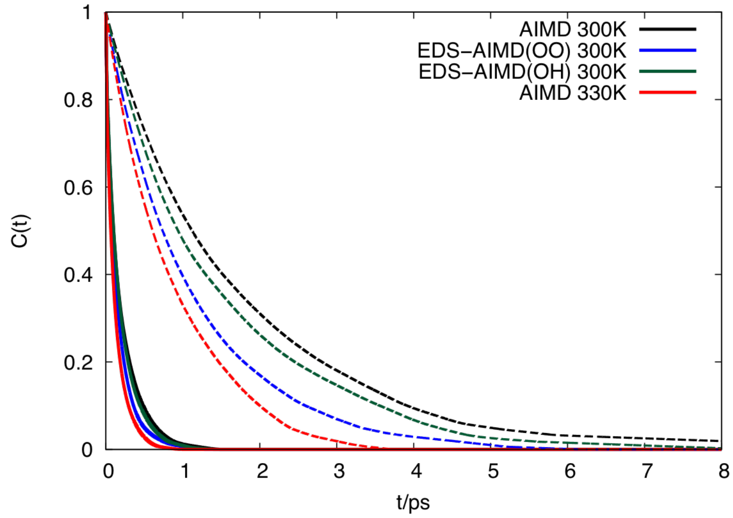

Figure 6-6: The continuous correlation function of the unfiltered (solid lines) and filtered (dashed lines) trajectories for the four methods.

proton transfer mechanism, and previous work has shown hydronium ion undergoes the so-called special pair dance before ultimately donating the proton.

One crucial feature of being able to pare down rattling events is that it should have no effect on concerted, multiple hopping events. However, simple visual inspection of the forward hopping plots, as well as comparing the number of multiple hopping events of the filtered and unfiltered events seem to support the notion of the special pair dance. In the unfiltered trajectories, we see the excess proton rapidly oscillating between waters. Not seen in the forward hopping plot, however, is that the identity of the waters often change, i.e. the following motion occurs: B ←→ A ←→ C. That is, water A is rapidly exchanging the proton with water B, then later exchanging the proton with water C. This is exactly the type of behavior described in Ref. [20]. Of course, we still see multiple hopping events, but if the true nature of the majority of these hops were concerted hops, we would expect to see a similar number in the unfiltered and filtered trajectories. As it turns out, there are very long periods of the trajectory where very little forward activity is occurring, in which the unfiltered trajectory shows constant hopping followed by subsequent back hopping, whereas the filtered trajectory shows no activity at all.

C. Multiple Hopping

In order to quantify the frequency of this type of event (B ←→ A ←→ C), we applied the analysis method in Ref. [188] to the simulation methods employed here; this allows us to quantify the hopping in association with some time scale. To do so, we define a function to quantify the number of water molecules to which the proton is associated over a given interval. In a given interval of length τ, the proton is assigned to the water on which it spends the most time during that interval. We then define the hopping function $h_n(\tau)$ as the number of occurrences the proton is associated with n waters over a timespan of n consecutive intervals of length τ. That is, if over a given interval τ, the proton is associated with one water and therefore no hopping happens, $h_1(\tau)$ is incremented; if two intervals are associated with two waters and thus in the case of single hopping, then $h_2(\tau)$ is incremented; if three waters are associated, then $h_3(\tau)$ counts the number of any form of concerted hopping involving three waters including both the forward hopping (A→B→C) and the A↔B↔C phenomenon. The analysis does not consider any hopping details and thus naturally eliminates the rattling and enables a direct focus on the proton hopping occurrences. We can quantify $h_n(\tau)$ for any number *n*, but for the sake of clarity, we have plotted the hopping function for $n = 1 - 3$, shown in Fig. 6-7.

The decay in $h_1(\tau)$ and $h_2(\tau)$ is a result of the decrease in the number of time segments in which the proton remains on either one or two waters, respectively, as the lengths of the time intervals are increased. We first investigate the effects on h_1 as τ is increased. As τ is increased, the proton is more likely to be associated with a greater number of different waters, and thus the $h_1(\tau)$ curves are all decreasing. Notice that EDS-AIMD (OO) and AIMD at 330 K decays faster than AIMD at 300 K with EDS-AIMD (OH) between AIMD at 300 K and 330K; this indicates more total hops in those methods. The plot for h_2 shows that a proton is slightly more likely to be

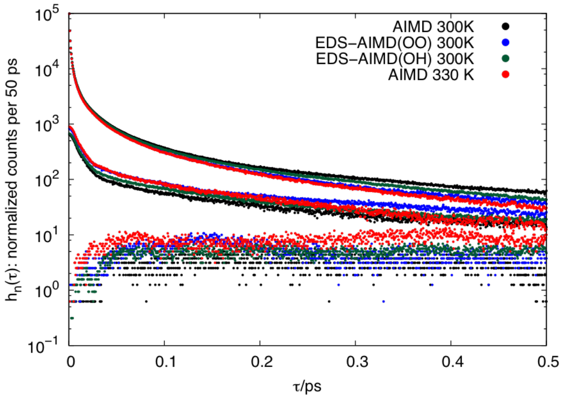

Figure 6-7: Concerted hopping on time scales between 0 and 0.5 ps.

associated with two waters in simulations run with AIMD at 330 K and EDS-AIMD (OO) followed by EDS-AIMD(OH) than in AIMD at 300 K. Consistent with the aforementioned trend that both AIMD at 330 K and EDS-AIMD have more concerting hopping than AIMD at 300 K, the contrast between the methods becomes more stark for h_3. At short times, EDS-AIMD (OO) and EDS-AIMD (OH) are similar to AIMD at 330 K, but for longer values of τ, the higher temperature simulation has more concerting hopping, with EDS-AIMD(OH) being the most in agreement with AIMD at 330 K at long times. AIMD at 300 K has fewer $n = 3$ events on all timescales.

D. Diffusion

Table 6-1: Diffusion Coefficients of hydrated excess proton and water from individual runs and their averages. All values are shown in units of Å^2/ps.

Simulation Method	Replica	D_{H^+}	$\langle D_{H^+} \rangle$	D_{H_2O}	$\langle D_{H_2O} \rangle$
AIMD (300K)	1	0.78	0.54 ± 0.25	0.054	0.027 ± 0.027
	2	0.29		0.00038	
EDS-AIMD (OO) (300K)	1	0.59	0.55 ± 0.04	0.13	0.13 ± 0.01
	2	0.51		0.14	
EDS-AIMD (OH) (300K)	1	1.02	0.78 ± 0.25	0.14	0.15 ± 0.01
	2	0.53		0.15	
AIMD (330K)	1	2.07	1.65 ± 0.42	0.17	0.16 ± 0.01
	2	1.23		0.15	

A principal utility of molecular dynamics is the ability to capture the dynamical properties of a system. Clearly, the dynamical property of greatest interest in a system involving hydrated protons is the proton self-diffusion constant. The proton self-diffusion constant for AIMD at 300

K is 0.54 ± 0.25 Å^2/ps; for EDS-AIMD (OO) at 300 K it is 0.55 ± 0.04 Å^2/ps; for EDS-AIMD (OH) at 300 K it is 0.78 ± 0.25 Å^2/ps, and for AIMD at 330 K it is 1.65 ± 0.42 Å^2/ps;. This is in comparison to the experimental self-diffusion constant of 0.94 Å^2/ps at 300 K. The results are summarized in Table 6-1, which includes the diffusion constants for the individual runs. We specify the self-diffusion constant for individual runs due to the fact that proton diffusion is so dependent on the solvation structure of an individual run. For example, compare the self-diffusion constants for the two independent runs of AIMD at 300 K: the calculated self-diffusion constants are 0.78 Å^2/ps and 0.29 Å^2/ps. That is, in one simulation, the proton dynamics very nearly match that of experiment, whereas in the second simulation, the proton diffuses very slowly. We find (in agreement with Ref. [63]) that the proton self-diffusion constant in AIMD at 330 K is higher than the experimental value at 300 K. This is a function of several factors, such as increased thermal energy and decreased proton transfer barrier.

In addition to proton self-diffusion, we also compare the self-diffusion constants of water. In AIMD at 300 K, the self-diffusion constant is 0.027 Å^2/ps; in EDS-AIMD (OO) at 300 K, it is 0.13 Å^2/ps; in EDS-AIMD (OH) at 300 K, it is 0.15 Å^2/ps, and in AIMD at 330 K it is 0.16 Å^2/ps. We note that AIMD at 300 K is well shy of the experimental value of 0.23 Å^2/ps.[160] However, there is a clear improvement upon application of the EDS bias, as the water self-diffusion constant increases an order of magnitude, with EDS-AIMD (OH) closer to experiment. This increase has to do with the reduced interactions and therefore reduced stickiness of the water molecules. Increasing the temperature to 330 K also has the pronounced effect of greatly increasing the water diffusion, but not sufficiently to bring it in alignment with experiment.

E. RDFs

We next examine the radial distribution functions (RDFs) of the hydrated proton, which provide a detailed description of the hydration structure of the excess proton. The RDF between hydronium oxygen and water oxygen (O*-O) is the most illustrative in describing the solvation structure of the excess proton, so we will examine it first. The data is presented in Fig. 6-8. First, notice that experimental data has a prominent first solvation shell peak centered at 2.45 Å having a height of 4.6. As one moves to longer distances, there is a distinct minimum (valley) at 2.9 Å, and a second solvation shell centered at 4.4 Å having a height of 1.15. None of the aspects perfectly reproduce each of these features exactly, but they do reproduce the general shape. In the four AIMD methods, the position of the first solvation shell peak is shifted to a slightly longer distance; we note all four methods have a first solvation shell peak center at 2.50 Å. AIMD at 300 K has the most pronounced peak, having very slightly greater than EDS-AIMD (OH) at 300 K, EDS-AIMD (OO) at 300 K, and AIMD at 330 K. The larger deviation from experiment comes in the size and position of the second solvation shell peaks. This peak is largely a function of water-water interactions, which are known to be too strong in AIMD, resulting in overstructuring. Interestingly, the second solvation shell in EDS-AIMD (OO) in nearly as overstructured as AIMD at 300 K, despite the fact that the O_w-O_w RDF is quite close to experiment, indicating there is some degree of interaction between the hydronium ion and waters in its second solvation shell. We note that EDS-AIMD (OO) was not specifically designed to model the hydronium-water interaction, and the improvement of the water-water solvation structure and water self-diffusion constant more than makes up for the modest effect of the hydrated proton. On the other hand, EDS-AIMD (OH) and AIMD at 330 K are the best in alignment with the second solvation shell of experiment.

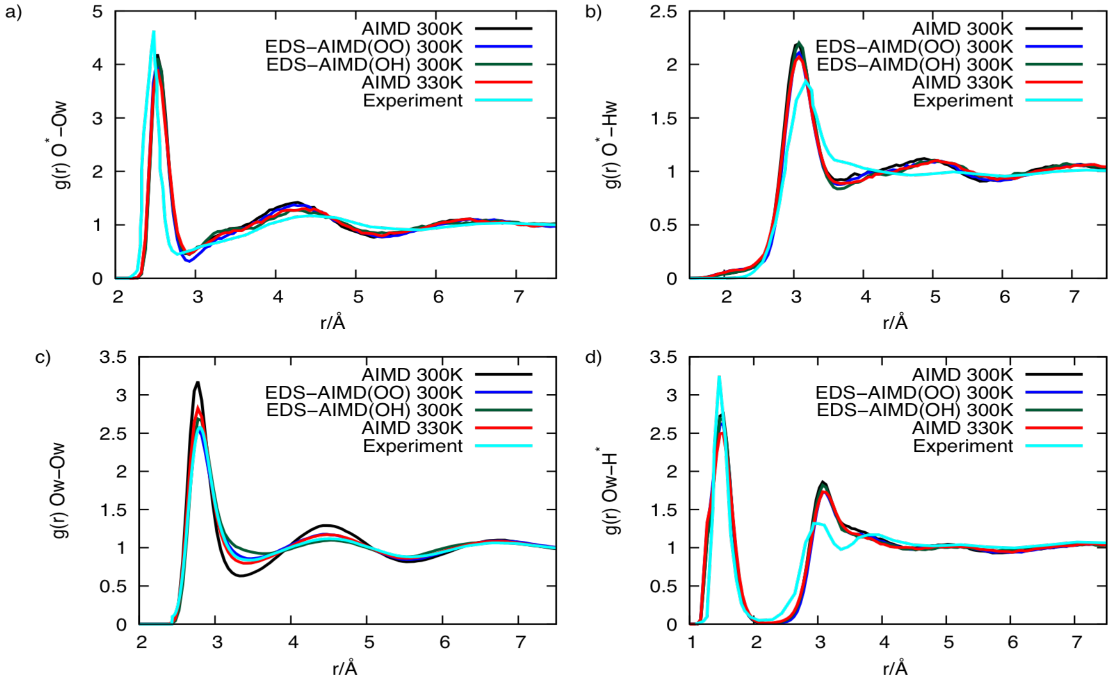

Figure 6-8: Radial distribution functions of the four methods studied in this paper in comparison with experiment.

We next compare the O*-H RDF for the four methods. At 300 K, both methods have at least a reasonably accurate first solvation peak center relative to experiment, though both slightly overestimate the peak height. The largest divergence from experiment occurs in the existence of a second solvation shell peak; experiment does not show this peak at all. That is, water hydrogens surrounding a hydronium ion have some structure within the first solvation shell, but none beyond that. Inclusion of quantum nuclear effects can mitigate that overstructuring by effectively "delocalizing" the relatively light hydrogen atoms, but that comes at a significant computational cost and would not be applicable to the types of systems the methods in this paper would ideally target.

Also note the existence of the so-called pre-solvation peak centered at around 2.0 Å. It has previously been argued that this peak is beneficial for proton transfer as it readies the hydronium to be able to donate the proton and become a water with 4-fold coordination.[188] In fact, previous work investigating proton transport in AIMD simulations has found that the proton self-diffusion constant is higher in the fragments of trajectories in which pre-solvation is prevalent; conversely, those with effectively no pre-solvation had a relatively stagnant excess proton that underwent few hops. (We remind the reader that AIMD water is notoriously glassy, and thus a given simulation can get "locked in" to a geometry with little to no presolvation.)

To illustrate a clear advantage of EDS-AIMD relative to stock AIMD, we present the O_w-O_w RDF in Fig. 6-8c. We see that the first solvation shell peak of AIMD at 300 K is centered correctly relative to experiment, but is quite a bit larger. Increasing the temperature of the AIMD simulation to 330 K reduces the size of this peak, but does not completely reduce its height to that of experiment. Similarly, AIMD at both temperatures (though much more severely at 300 K) has a too-deep well between the first and second solvation shell, and a second solvation shell peak that is more pronounced than experiment. EDS-AIMD (OO) at 300 K is specifically designed to reproduce the O_w-O_w RDF, and we see essentially perfect matching throughout. Additionally, EDS-AIMD (OH) at 300 K is slightly more structured than EDS-AIMD (OO) because it was parameterized to reproduce classical MB-pol O_w-H_w RDF, while EDS-AIMD (OO) was parameterized to reproduce the experimental RDF that incorporated nuclear quantum effects. This has interesting ramifications for the diffusion constant of water, but importantly, this highlights the advantage of using a more accurate method (EDS-AIMD) rather than simply elevating the temperature of the simulation.

IV. Conclusion

Our results lead us to the conclusion that while concerted proton hopping in water does occur, it is not the dominant mechanism. Rather, single proton hopping events occur in much greater numbers than double or higher order multiple hopping events. We have evaluated AIMD at both 300 K and 330 K, as well as experimentally biased EDS-AIMD at 300 K, and find dominance of single hopping events in all simulations. While multiple hopping events do occur, most are in fact the result of the proton rattling between several waters, and in most cases the proton ultimately returns to the original water. Thus, our current results are consistent with the previously reported mechanism described as a special pair dance.

In order to remove the misleading effect of rattling, we applied a filter to the trajectory, where we removed all hopping events which are followed directly by a back hop to the original water. This had a drastic effect on the total number of (apparent) hops, but more interestingly, this greatly reduced the number of multiple hops counted. One would expect that if a multiple hopping event were truly concerted, they would be retained despite the filtering. Filtering the trajectory has the effect of greatly reducing the number of slingshot events, i.e. where either a back hop is followed by a forward hop. We argue that double hops which are immediately followed by a nullifying back hop are not concerted, and therefore should not be included as a true double hop.

Calculation of the continuous correlation function on the filtered and unfiltered trajectories yield lifetimes similar to experimental values for the proton hopping time and the Eigen-Zundel interconversion time, respectively. In all simulations, AIMD at 330 K decays most rapidly, which is unsurprising given the elevated temperature facilitates hopping.

We find a strong dependence of the multiple hopping rates on temperature, which correlates to a strong dependence of the diffusion on temperature. We find that AIMD at 300 K has a proton self-diffusion constant of 0.54 ± 0.25 Å^2/ps, while AIMD at 330 K has a diffusion constant of 1.65 ± 0.42 Å^2/ps, about 75 % larger than experiment. This too-rapid diffusion at 330 K relative to experiment would only be further exacerbated by the inclusion of nuclear quantum and finite size effects. Thus, caution should be taken when analyzing simulations at elevated temperatures.

Appendix A: Additional Physical Properties

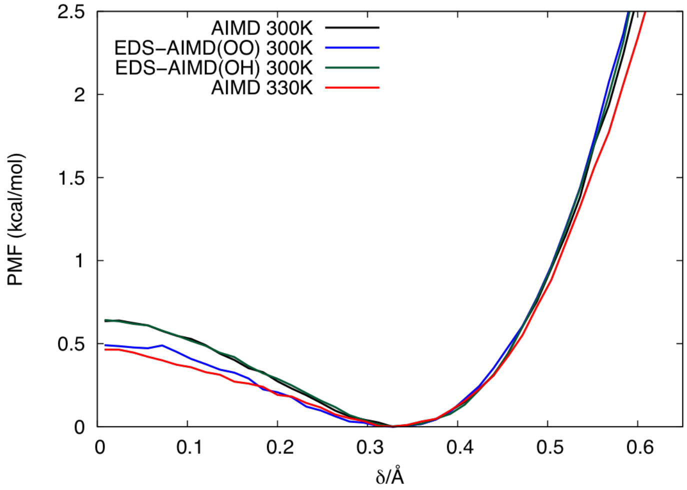

Figure 6-9: Potential of Mean Force for the delta reactive coordinate. In black is AIMD at 300 K, in blue is EDS-AIMD(OO) at 300 K, in green is EDS-AIMD(OH) at 300 K, and in red is AIMD at 330 K.

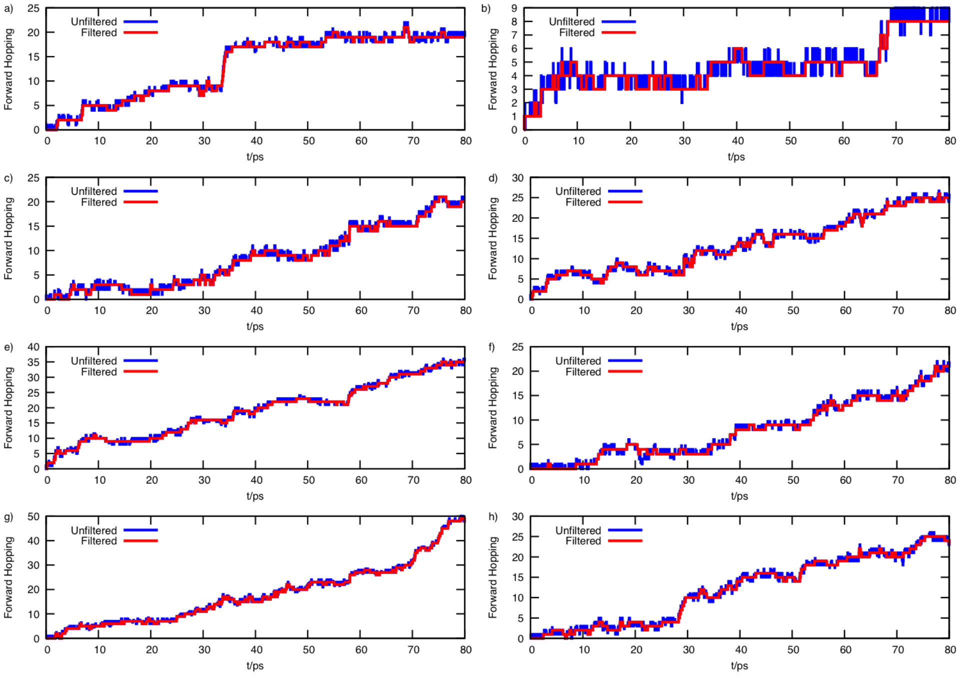

Figure 6-10: Forward hopping as a function of time for the various simulation methods utilized in this work. Fig a-b are AIMD at 300 K, Fig c-d are EDS-AIMD(OO), Fig e-f are EDS-AIMD(OH) at 300 K, and Fig. g-h are AIMD at 330 K at 300 K. In blue is the total forward hopping as a function, of time, and red is the filtered forward hopping.

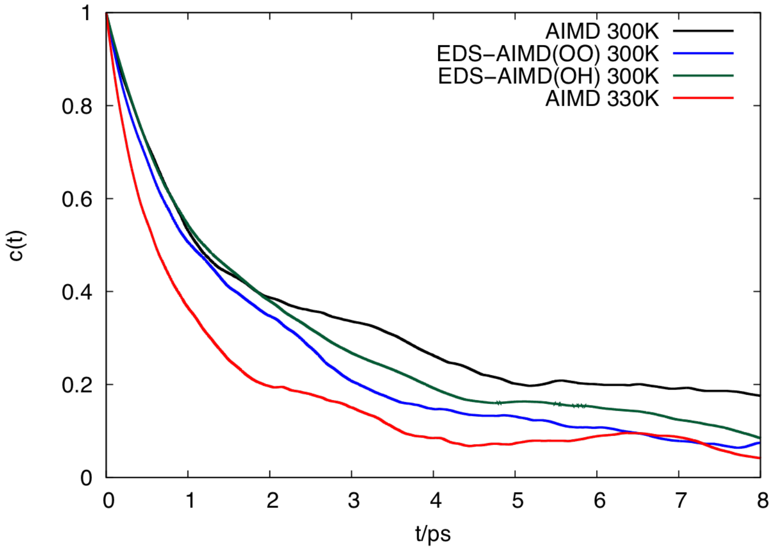

Figure 6-11: Proton correlation function of the four computational methods studied here using the filtering method described in the text.

Chapter 7: Conclusion

I. Summary of Thesis

This thesis presents work using reactive molecular dynamics simulation methods to understand proton transport in aqueous systems. Specifically, *ab initio* molecular dynamics (AIMD), experiment directed simulations of AIMD (EDS-AIMD), and the multistate empirical valence bond (MS-EVB) methods were used as they can model the dynamic bonding topology necessary to model the Grotthuss mechanism of the hydrated excess proton. These methods were used to correspond simulation findings with recent experimental results (Chapter 2 & Chapter 3), proton transport in Nafion membranes under external electric fields (Chapter 4), improve AIMD simulations using EDS to bias the hydrogen bond (Chapter 5), and further analyze the proton hopping behavior in AIMD simulations (Chapter 6).

The use of EDS-AIMD(OO) and MS-EVB simulations showed that the hydrated excess proton has a water molecule residing closer to the hydronium core forming a special-pair structure and these methods were used to understand the hydrated excess proton in light of recent two dimensional infrared spectroscopy experiments. Specifically, we correlated anisotropy trends of the special-pair dance and irreversible proton transport to time constants corresponding to 10-40 fs and ~1-2 ps, respectively, where the time constant of irreversible proton transport is in excellent agreement to the anisotropy of flanking water bends in a Zundel-like or special-pair configuration.[57, 59] This work further showed via time evolution of normal modes that the dynamics of the hydrated excess proton are essential to fully understanding the hydrated proton's solvation. This work was further extended by using the self-consistent iterative (SCI-)MS-EVB method to understand the dynamics, structure, and thermodynamics of the hydrated proton as a function of concentration and temperature. This work provided atomistic detail to trends found in recent two dimensional infrared spectroscopy that showed that reorientation time constants increase with chloride concentration while exhibiting a decrease in activation energy.[59] It was argued both experimentally and theoretically that this is due to chlorides creating entropic barriers to proton transport.

The SCI-MS-EVB method was than further applied to understand proton transport in hydrated Nafion membranes for applications in proton exchange membrane fuel cells (PEMFC). This work investigated how various electric field magnitudes influence proton transport in Nafion membranes with hydration levels 10 and 15 at 300 K and 353 K. Previous reactive simulations[6] have shown that the proton transports in the water channel via association with sulfonate groups, and it was shown that electric fields have a negligible effect on this mechanism. Additionally, it was found that electric fields enhance the dynamics of the hydrated excess proton and reducing caging effects of the proton.

This thesis additionally present applications of the EDS method to improve AIMD simulations of water. It is shown that EDS can be used to bias the hydrogen bond in AIMD water to reproduce the O-H RDF of MB-pol, and by biasing the O-H RDF in water, we observed improved structural and dynamical properties in unbiased quantities. These improvements are even greater than our previous application of EDS in AIMD simulation that biased the solvation structure.[43] This simulation method was then used to model the hydrated excess proton, in addition to EDS-AIMD(OO), AIMD at 300 K, and AIMD at 330 K, to further analyze the proton transport mechanism. Recent AIMD simulations[63] have proposed double hops are the dominate hopping mechanism in water, which seemed contradictory to previous simulation results. Our findings show that single proton hops dominate in all simulation methods, but that simulations with a higher temperature have more multiple hopping events and larger proton diffusion coefficients than simulations at 300 K. The presence of single hopping events is in agreement with the Eigen-Zundel-Eigen mechanism previously proposed in simulation.

II. Future Work

The anisotropy decays presented in this thesis use a simple special-pair unit vector to describe the various reorientations for the hydrated excess proton, and only implicitly accounts for the hydrogen bonds breaking between water molecules to assist in proton transport. Remarkably, this special-pair unit vector was used to show trends in anisotropy time constants and activation energies for proton transport. However, amplitudes in these anisotropy fits do not match with experiments, and have not addressed the polarization trends found in experiments. Future work must therefore find a unit vector and/or collective variable that can capture the proper degrees of freedom to characterize proton transport, while corresponding to experimental findings. Such collective variables must account for the electronic delocalization of the hydrated excess proton, the nuclear delocalization that requires nuclear quantum effects in molecular simulations, and the delocalization of vibrational modes across multiple water molecules. This future work additionally must account for the dynamics of the hydrated excess proton complex, especially since the dynamics is what further distinguish Zundel-like configurations from the distorted Eigen cation, and it is also encouraging that the proton community is moving in this direction, see discussion in Ref [23].

It has also been shown that EDS is a resourceful tool to bias molecular simulations to improve AIMD models of water and hydrated excess proton. EDS-AIMD simulations presented here have been limited to bulk environments in constant volume simulations. AIMD simulations have been known to underestimate the density of water in the constant NpT ensemble[163-164] and future work should investigate the density of the EDS-AIMD simulations and might require recent advancements to the EDS learning algorithm.[152] The EDS-AIMD(OO) model of the hydrated excess proton has been used to generate multiscale reactive molecular dynamics (MS-RMD) models[189] using relative entropy minimization,[179, 190] and future work can include using EDS-AIMD(OH) proton model as a reference for future MS-RMD models.

Bibliography

1. Brown, T. L. L., H. E. Jr; Bursten, B. E.; Murphy, C. J.; Woodward, P. M. *Chemistry: The Central Science* 12 ed.; Pearson Prentice Hall: Upper Saddle River, NJ, 2009.

2. Zumdahl, S. S. Z., S. A *Chemistry*; Brooks Cole: Belmont, CA, 2014.

3. Cukierman, S. Et tu, Grotthuss! and other unfinished stories. *Biochim. Biophys. Acta, Bioenerg.* **2006,** *1757*, 876-885.

4. Bernal, J. D.; Fowler, R. H. A Theory of Water and Ionic Solution, with Particular Reference to Hydrogen and Hydroxyl Ions. *J. Chem. Phys.* **1933,** *1*, 515-548.

5. Kreuer, K.-D.; Paddison, S. J.; Spohr, E.; Schuster, M. Transport in Proton Conductors for Fuel-Cell Applications: Simulations, Elementary Reactions, and Phenomenology. *Chem. Rev.* **2004,** *104*, 4637-4678.

6. Savage, J.; Tse, Y.-L. S.; Voth, G. A. Proton Transport Mechanism of Perfluorosulfonic Acid Membranes. *J. Phys. Chem. C.* **2014,** *118*, 17436-17445.

7. Arntsen, C.; Savage, J.; Tse, Y. L. S.; Voth, G. A. Simulation of Proton Transport in Proton Exchange Membranes with Reactive Molecular Dynamics. *Fuel Cells.* **2016,** *16*, 695-703.

8. Kaila, V. R. I.; Verkhovsky, M. I.; Wikström, M. Proton-Coupled Electron Transfer in Cytochrome Oxidase. *Chem. Rev.* **2010,** *110*, 7062-7081.

9. Wraight, C. A. Chance and design—Proton transfer in water, channels and bioenergetic proteins. *Biochim. Biophys. Acta, Bioenerg.* **2006,** *1757*, 886-912.

10. Decoursey, T. E. Voltage-Gated Proton Channels and Other Proton Transfer Pathways. *Physiol. Rev.* **2003,** *83*, 475-579.

11. Swanson, J. M. J.; Maupin, C. M.; Chen, H.; Petersen, M. K.; Xu, J.; Wu, Y.; Voth, G. A. Proton Solvation and Transport in Aqueous and Biomolecular Systems: Insights from Computer Simulations. *J. Phys. Chem. B.* **2007,** *111*, 4300-4314.

12. Mauritz, K. A.; Moore, R. B. State of Understanding of Nafion. *Chem. Rev.* **2004,** *104*, 4535-4586.

13. Gebel, G. Structural evolution of water swollen perfluorosulfonated ionomers from dry membrane to solution. *Polymer.* **2000,** *41*, 5829-5838.

14. Grotthus, C. J. T. V. Sur la décomposition de l'eau et des corps qu'elle tient en dissolution à l'aide de l'électricité galvanique. *Ann. Chim.* **1806,** *58*, 54–73.

15. Agmon, N. The Grotthuss mechanism. *Chem. Phys. Lett.* **1995,** *244*, 456-462.

16. Swanson, J. M. J.; Simons, J. Role of Charge Transfer in the Structure and Dynamics of the Hydrated Proton. *J. Phys. Chem. B.* **2009,** *113*, 5149-5161.

17. Eigen, M. Proton Transfer, Acid-Base Catalysis, and Enzymatic Hydrolysis. Part I: ELEMENTARY PROCESSES. *Angew. Chem. Int. Ed. Engl.* **1964,** *3*, 1-19.

18. Zundel, G.; Metzger, H., Energiebänder der tunnelnden Überschuß-Protonen in flüssigen Säuren. Eine IR-spektroskopische Untersuchung der Natur der Gruppierungen H5O2+. In *Z. Phys. Chem.*, 1968; Vol. 58, p 225.

19. Lapid, H.; Agmon, N.; Petersen, M. K.; Voth, G. A. A bond-order analysis of the mechanism for hydrated proton mobility in liquid water. *J. Chem. Phys.* **2004,** *122*, 014506.

20. Markovitch, O.; Chen, H.; Izvekov, S.; Paesani, F.; Voth, G. A.; Agmon, N. Special Pair Dance and Partner Selection: Elementary Steps in Proton Transport in Liquid Water. *J. Phys. Chem. B.* **2008,** *112*, 9456-9466.

21. Fournier, J. A.; Carpenter, W. B.; Lewis, N. H. C.; Tokmakoff, A. Broadband 2D IR spectroscopy reveals dominant asymmetric H5O2+ proton hydration structures in acid solutions. *Nat. Chem.* **2018,** *10*, 932-937.

22. Yu, Q.; Carpenter, W. B.; Lewis, N. H. C.; Tokmakoff, A.; Bowman, J. M. High-Level VSCF/VCI Calculations Decode the Vibrational Spectrum of the Aqueous Proton. *J. Phys. Chem. B.* **2019,** *123*, 7214-7224.

23. Carpenter, W. B.; Yu, Q.; Hack, J. H.; Dereka, B.; Bowman, J. M.; Tokmakoff, A. Decoding the 2D IR spectrum of the aqueous proton with high-level VSCF/VCI calculations. *J. Chem. Phys.* **2020,** *153*, 124506.

24. Car, R.; Parrinello, M. Unified Approach for Molecular Dynamics and Density-Functional Theory. *Phys. Rev. Lett.* **1985,** *55*, 2471-2474.

25. Perdew, J. P.; Burke, K.; Ernzerhof, M. Generalized Gradient Approximation Made Simple. *Phys. Rev. Lett.* **1996,** *77*, 3865-3868.

26. Becke, A. D. Density-functional exchange-energy approximation with correct asymptotic behavior. *Phys. Rev. A.* **1988,** *38*, 3098-3100.

27. Lee, C.; Yang, W.; Parr, R. G. Development of the Colle-Salvetti correlation-energy formula into a functional of the electron density. *Phys. Rev. B.* **1988,** *37*, 785-789.

28. Tozer, D. J.; Handy, N. C. The development of new exchange-correlation functionals. *J. Chem. Phys.* **1998,** *108*, 2545-2555.

29. Tozer, D. J.; Handy, N. C. Improving virtual Kohn–Sham orbitals and eigenvalues: Application to excitation energies and static polarizabilities. *J. Chem. Phys.* **1998,** *109*, 10180-10189.

30. Ruiz, E.; Salahub, D. R.; Vela, A. Charge-Transfer Complexes: Stringent Tests for Widely Used Density Functionals. *J. Phys. Chem.* **1996,** *100*, 12265-12276.

31. Becke, A. D.; Dale, S. G.; Johnson, E. R. Communication: Correct charge transfer in CT complexes from the Becke'05 density functional. *J. Chem. Phys.* **2018,** *148*, 211101.

32. Gillan, M. J.; Alfè, D.; Michaelides, A. Perspective: How good is DFT for water? *J. Chem. Phys.* **2016,** *144*, 130901.

33. Tse, Y.-L. S.; Knight, C.; Voth, G. A. An analysis of hydrated proton diffusion in ab initio molecular dynamics. *J. Chem. Phys.* **2015,** *142*, 014104.

34. Todorova, T.; Seitsonen, A. P.; Hutter, J.; Kuo, I. F. W.; Mundy, C. J. Molecular Dynamics Simulation of Liquid Water: Hybrid Density Functionals. *J. Phys. Chem. B.* **2006,** *110*, 3685-3691.

35. Grossman, J. C.; Schwegler, E.; Draeger, E. W.; Gygi, F.; Galli, G. Towards an assessment of the accuracy of density functional theory for first principles simulations of water. *J. Chem. Phys.* **2003,** *120*, 300-311.

36. DiStasio, R. A.; Santra, B.; Li, Z.; Wu, X.; Car, R. The individual and collective effects of exact exchange and dispersion interactions on the ab initio structure of liquid water. *J. Chem. Phys.* **2014,** *141*, 084502.

37. Chen, M.; Ko, H.-Y.; Remsing, R. C.; Calegari Andrade, M. F.; Santra, B.; Sun, Z.; Selloni, A.; Car, R.; Klein, M. L.; Perdew, J. P.; Wu, X. Ab initio theory and modeling of water. *Proceedings of the National Academy of Sciences.* **2017,** *114*, 10846.

38. Ruiz Pestana, L.; Marsalek, O.; Markland, T. E.; Head-Gordon, T. The Quest for Accurate Liquid Water Properties from First Principles. *J. Phys. Chem. Lett.* **2018,** *9*, 5009-5016.

39. Zhang, C.; Donadio, D.; Gygi, F.; Galli, G. First Principles Simulations of the Infrared Spectrum of Liquid Water Using Hybrid Density Functionals. *J. Chem. Theory Comput.* **2011,** *7*, 1443-1449.

40. Dannenhoffer-Lafage, T.; White, A. D.; Voth, G. A. A Direct Method for Incorporating Experimental Data into Multiscale Coarse-Grained Models. *J. Chem. Theory Comput.* **2016,** *12*, 2144-2153.

41. White, A. D.; Voth, G. A. Efficient and Minimal Method to Bias Molecular Simulations with Experimental Data. *J. Chem. Theory Comput.* **2014,** *10*, 3023-3030.

42. Hocky, G. M.; Dannenhoffer-Lafage, T.; Voth, G. A. Coarse-Grained Directed Simulation. *J. Chem. Theory Comput.* **2017,** *13*, 4593-4603.

43. White, A. D.; Knight, C.; Hocky, G. M.; Voth, G. A. Communication: Improved ab initio molecular dynamics by minimally biasing with experimental data. *J. Chem. Phys.* **2017,** *146*, 041102.

44. Pitera, J. W.; Chodera, J. D. On the Use of Experimental Observations to Bias Simulated Ensembles. *J. Chem. Theory Comput.* **2012,** *8*, 3445-3451.

45. Schmitt, U. W.; Voth, G. A. Multistate Empirical Valence Bond Model for Proton Transport in Water. *J. Phys. Chem. B.* **1998,** *102*, 5547-5551.

46. Schmitt, U. W.; Voth, G. A. The computer simulation of proton transport in water. *J. Chem. Phys.* **1999,** *111*, 9361-9381.

47. Day, T. J. F.; Soudackov, A. V.; Čuma, M.; Schmitt, U. W.; Voth, G. A. A second generation multistate empirical valence bond model for proton transport in aqueous systems. *J. Chem. Phys.* **2002,** *117*, 5839-5849.

48. Wu, Y.; Chen, H.; Wang, F.; Paesani, F.; Voth, G. A. An Improved Multistate Empirical Valence Bond Model for Aqueous Proton Solvation and Transport. *J. Phys. Chem. B.* **2008,** *112*, 467-482.

49. Biswas, R.; Tse, Y.-L. S.; Tokmakoff, A.; Voth, G. A. Role of Presolvation and Anharmonicity in Aqueous Phase Hydrated Proton Solvation and Transport. *J. Phys. Chem. B.* **2016,** *120*, 1793-1804.

50. Wang, F.; Voth, G. A. A linear-scaling self-consistent generalization of the multistate empirical valence bond method for multiple excess protons in aqueous systems. *J. Chem. Phys.* **2005,** *122*, 144105.

51. Tuckerman, M.; Laasonen, K.; Sprik, M.; Parrinello, M. Ab Initio Molecular Dynamics Simulation of the Solvation and Transport of H3O+ and OH- Ions in Water. *J. Phys. Chem.* **1995,** *99*, 5749-5752.

52. Tuckerman, M.; Laasonen, K.; Sprik, M.; Parrinello, M. Ab initio molecular dynamics simulation of the solvation and transport of hydronium and hydroxyl ions in water. *J. Chem. Phys.* **1995,** *103*, 150-161.

53. Agmon, N. Proton Solvation and Proton Mobility. *Isr. J. Chem.* **1999,** *39*, 493-502.

54. Marx, D.; Tuckerman, M. E.; Hutter, J.; Parrinello, M. The nature of the hydrated excess proton in water. *Nature.* **1999,** *397*, 601-604.

55. Agmon, N. Hydrogen bonds, water rotation and proton mobility. *J. Chim. Phys.* **1996,** *93*, 1714-1736.

56. Meiboom, S. Nuclear Magnetic Resonance Study of the Proton Transfer in Water. *J. Chem. Phys.* **1961,** *34*, 375-388.

57. Carpenter, W. B.; Fournier, J. A.; Lewis, N. H. C.; Tokmakoff, A. Picosecond Proton Transfer Kinetics in Water Revealed with Ultrafast IR Spectroscopy. *J. Phys. Chem. B.* **2018,** *122*, 2792-2802.

58. Thämer, M.; De Marco, L.; Ramasesha, K.; Mandal, A.; Tokmakoff, A. Ultrafast 2D IR spectroscopy of the excess proton in liquid water. *Science.* **2015,** *350*, 78.

59. Carpenter, W. B.; Lewis, N. H. C.; Fournier, J. A.; Tokmakoff, A. Entropic barriers in the kinetics of aqueous proton transfer. *J. Chem. Phys.* **2019,** *151*, 034501.

60. Dahms, F.; Fingerhut, B. P.; Nibbering, E. T. J.; Pines, E.; Elsaesser, T. Large-amplitude transfer motion of hydrated excess protons mapped by ultrafast 2D IR spectroscopy. *Science.* **2017,** *357*, 491.

61. Kundu, A.; Dahms, F.; Fingerhut, B. P.; Nibbering, E. T. J.; Pines, E.; Elsaesser, T. Hydrated Excess Protons in Acetonitrile/Water Mixtures: Solvation Species and Ultrafast Proton Motions. *J. Phys. Chem. Lett.* **2019,** *10*, 2287-2294.

62. Hassanali, A.; Giberti, F.; Cuny, J.; Kühne, T. D.; Parrinello, M. Proton transfer through the water gossamer. *Proceedings of the National Academy of Sciences.* **2013,** *110*, 13723.

63. Chen, M.; Zheng, L.; Santra, B.; Ko, H.-Y.; DiStasio Jr, R. A.; Klein, M. L.; Car, R.; Wu, X. Hydroxide diffuses slower than hydronium in water because its solvated structure inhibits correlated proton transfer. *Nat. Chem.* **2018,** *10*, 413-419.

64. CRC handbook of chemistry and physics. **1977**.

65. Grotthuss, C. J. D. v. *Ann. Chim.* **1806,** *LVIII*, 54.

66. Lobaugh, J.; Voth, G. A. The quantum dynamics of an excess proton in water. *J. Chem. Phys.* **1996,** *104*, 2056-2069.

67. Marx, D. Proton Transfer 200 Years after von Grotthuss: Insights from Ab Initio Simulations. *Chem. Phys. Chem.* **2006,** *7*, 1848-1870.

68. Knight, C.; Voth, G. A. The Curious Case of the Hydrated Proton. *Acc. Chem. Res.* **2012,** *45*, 101-109.

69. Vuilleumier, R.; Borgis, D. Quantum Dynamics of an Excess Proton in Water Using an Extended Empirical Valence-Bond Hamiltonian. *J. Phys. Chem. B.* **1998,** *102*, 4261-4264.

70. Vuilleumier, R.; Borgis, D. An Extended Empirical Valence Bond Model for Describing Proton Mobility in Water. *Isr. J. Chem.* **1999,** *39*, 457-467.

71. Kornyshev, A. A.; Kuznetsov, A. M.; Spohr, E.; Ulstrup, J. Kinetics of Proton Transport in Water. *J. Phys. Chem. B.* **2003,** *107*, 3351-3366.

72. Asmis, K. R.; Pivonka, N. L.; Santambrogio, G.; Brümmer, M.; Kaposta, C.; Neumark, D. M.; Wöste, L. Gas-Phase Infrared Spectrum of the Protonated Water Dimer. *Science.* **2003,** *299*, 1375.

73. Heine, N.; Fagiani, M. R.; Rossi, M.; Wende, T.; Berden, G.; Blum, V.; Asmis, K. R. Isomer-Selective Detection of Hydrogen-Bond Vibrations in the Protonated Water Hexamer. *J. Am. Chem. Soc.* **2013,** *135*, 8266-8273.

74. Headrick, J. M.; Diken, E. G.; Walters, R. S.; Hammer, N. I.; Christie, R. A.; Cui, J.; Myshakin, E. M.; Duncan, M. A.; Johnson, M. A.; Jordan, K. D. Spectral Signatures of Hydrated Proton Vibrations in Water Clusters. *Science.* **2005,** *308*, 1765.

75. Heine, N.; Fagiani, M. R.; Asmis, K. R. Disentangling the Contribution of Multiple Isomers to the Infrared Spectrum of the Protonated Water Heptamer. *J. Phys. Chem. Lett.* **2015,** *6*, 2298-2304.

76. Giberti, F.; Hassanali, A. A.; Ceriotti, M.; Parrinello, M. The Role of Quantum Effects on Structural and Electronic Fluctuations in Neat and Charged Water. *J. Phys. Chem. B.* **2014,** *118*, 13226-13235.

77. Biswas, R.; Carpenter, W.; Fournier, J. A.; Voth, G. A.; Tokmakoff, A. IR spectral assignments for the hydrated excess proton in liquid water. *J. Chem. Phys.* **2017,** *146*, 154507.

78. Daly, C. A.; Streacker, L. M.; Sun, Y.; Pattenaude, S. R.; Hassanali, A. A.; Petersen, P. B.; Corcelli, S. A.; Ben-Amotz, D. Decomposition of the Experimental Raman and Infrared Spectra of Acidic Water into Proton, Special Pair, and Counterion Contributions. *J. Phys. Chem. Lett.* **2017,** *8*, 5246-5252.

79. Kulig, W.; Agmon, N. A ‘clusters-in-liquid’ method for calculating infrared spectra identifies the proton-transfer mode in acidic aqueous solutions. *Nat. Chem.* **2012,** *5*, 29.

80. Park, K.; Lin, W.; Paesani, F. A Refined MS-EVB Model for Proton Transport in Aqueous Environments. *J. Phys. Chem. B.* **2012,** *116*, 343-352.

81. Biswas, R.; Tse, Y.-L. S.; Tokmakoff, A.; Voth, G. A. Role of Presolvation and Anharmonicity in Aqueous Phase Hydrated Proton Solvation and Transport. *The Journal of Physical Chemistry B.* **2016,** *120*, 1793-1804.

82. Biswas, R.; Carpenter, W.; Voth, G. A.; Tokmakoff, A. Molecular modeling and assignment of IR spectra of the hydrated excess proton in isotopically dilute water. *J. Chem. Phys.* **2016,** *145*, 154504.

83. Plimpton, S. Fast Parallel Algorithms for Short-Range Molecular Dynamics. *J. Comput. Phys.* **1995,** *117*, 1-19.

84. Wu, Y.; Tepper, H. L.; Voth, G. A. Flexible simple point-charge water model with improved liquid-state properties. *J. Chem. Phys.* **2006,** *124*, 024503.

85. Grimme, S. Accurate description of van der Waals complexes by density functional theory including empirical corrections. *J. Comput. Chem.* **2004,** *25*, 1463-1473.

86. Grimme, S.; Antony, J.; Ehrlich, S.; Krieg, H. A consistent and accurate ab initio parametrization of density functional dispersion correction (DFT-D) for the 94 elements H-Pu. *J. Chem. Phys.* **2010,** *132*, 154104.

87. VandeVondele, J.; Krack, M.; Mohamed, F.; Parrinello, M.; Chassaing, T.; Hutter, J. Quickstep: Fast and accurate density functional calculations using a mixed Gaussian and plane waves approach. *Comput. Phys. Commun.* **2005,** *167*, 103-128.

88. Bonomi, M.; Branduardi, D.; Bussi, G.; Camilloni, C.; Provasi, D.; Raiteri, P.; Donadio, D.; Marinelli, F.; Pietrucci, F.; Broglia, R. A.; Parrinello, M. PLUMED: A portable plugin for free-energy calculations with molecular dynamics. *Comput. Phys. Commun.* **2009,** *180*, 1961-1972.

89. Goedecker, S.; Teter, M.; Hutter, J. Separable dual-space Gaussian pseudopotentials. *Phys. Rev. B.* **1996,** *54*, 1703-1710.

90. Buchner, M.; Ladanyi, B. M.; Stratt, R. M. The short-time dynamics of molecular liquids. Instantaneous-normal-mode theory. *J. Chem. Phys.* **1992,** *97*, 8522-8535.

91. Keyes, T. Instantaneous Normal Mode Approach to Liquid State Dynamics. *J. Phys. Chem. A.* **1997,** *101*, 2921-2930.

92. Becke, A. D. Density-functional thermochemistry. III. The role of exact exchange. *J. Chem. Phys.* **1993,** *98*, 5648-5652.

93. M. J. Frisch, G. W. T., H. B. Schlegel, G. E. Scuseria, M. A. Robb, J. R. Cheeseman, G. Scalmani, V. Barone, G. A. Petersson, H. Nakatsuji, X. Li, M. Caricato, A. Marenich, J. Bloino, B. G. Janesko, R. Gomperts, B. Mennucci, H. P. Hratchian, J. V. Ortiz, A. F. Izmaylov, J. L. Sonnenberg, D. Williams-Young, F. Ding, F. Lipparini, F. Egidi, J. Goings, B. Peng, A. Petrone,

T. Henderson, D. Ranasinghe, V. G. Zakrzewski, J. Gao, N. Rega, G. Zheng, W. Liang, M. Hada, M. Ehara, K. Toyota, R. Fukuda, J. Hasegawa, M. Ishida, T. Nakajima, Y. Honda, O. Kitao, H. Nakai, T. Vreven, K. Throssell, J. A. Montgomery, Jr., J. E. Peralta, F. Ogliaro, M. Bearpark, J. J. Heyd, E. Brothers, K. N. Kudin, V. N. Staroverov, T. Keith, R. Kobayashi, J. Normand, K. Raghavachari, A. Rendell, J. C. Burant, S. S. Iyengar, J. Tomasi, M. Cossi, J. M. Millam, M. Klene, C. Adamo, R. Cammi, J. W. Ochterski, R. L. Martin, K. Morokuma, O. Farkas, J. B. Foresman, and D. J. Fox GAUSSIAN 09, Revision D.01. 2009.

94. Roy, S.; Schenter, G. K.; Napoli, J. A.; Baer, M. D.; Markland, T. E.; Mundy, C. J. Resolving Heterogeneous Dynamics of Excess Protons in Aqueous Solution with Rate Theory. *J. Phys. Chem. B.* **2020,** *124*, 5665-5675.

95. Laage, D.; Stirnemann, G.; Sterpone, F.; Rey, R.; Hynes, J. T. Reorientation and Allied Dynamics in Water and Aqueous Solutions. *Annu. Rev. Phys. Chem.* **2011,** *62*, 395-416.

96. Agmon, N.; Bakker, H. J.; Campen, R. K.; Henchman, R. H.; Pohl, P.; Roke, S.; Thämer, M.; Hassanali, A. Protons and Hydroxide Ions in Aqueous Systems. *Chem. Rev.* **2016,** *116*, 7642-7672.

97. Grotthuss, C. J. D. v. Sur la decomposition de l'eau et des corps qu'elle tient en dissolution a l'aide de l'electricite galvanique. *Ann. Chim.* **1806,** *LVIII*, 54.

98. Marx, D. Proton Transfer 200 Years after von Grotthuss: Insights from Ab Initio Simulations. *Chem. Phys. Chem.* **2006,** *7*, 1848-1870.

99. Napoli, J. A.; Marsalek, O.; Markland, T. E. Decoding the spectroscopic features and time scales of aqueous proton defects. *J. Chem. Phys.* **2018,** *148*, 222833.

100. Chandra, A.; Tuckerman, M. E.; Marx, D. Connecting Solvation Shell Structure to Proton Transport Kinetics in Hydrogen--Bonded Networks via Population Correlation Functions. *Phys. Rev. Lett.* **2007,** *99*, 145901.

101. Wang, F.; Izvekov, S.; Voth, G. A. Unusual "Amphiphilic" Association of Hydrated Protons in Strong Acid Solution. *J. Am. Chem. Soc.* **2008,** *130*, 3120-3126.

102. Xu, J.; Izvekov, S.; Voth, G. A. Structure and Dynamics of Concentrated Hydrochloric Acid Solutions. *J. Phys. Chem. B.* **2010,** *114*, 9555-9562.

103. Robinson, R. A. The dissociation constant of hydrochloric acid. *Trans. Faraday Soc.* **1936,** *32*, 743-744.

104. Dang, L. X. Mechanism and Thermodynamics of Ion Selectivity in Aqueous Solutions of 18-Crown-6 Ether: A Molecular Dynamics Study. *J. Am. Chem. Soc.* **1995,** *117*, 6954-6960.

105. Das, A. K.; Urban, L.; Leven, I.; Loipersberger, M.; Aldossary, A.; Head-Gordon, M.; Head-Gordon, T. Development of an Advanced Force Field for Water Using Variational Energy Decomposition Analysis. *J. Chem. Theory Comput.* **2019,** *15*, 5001-5013.

106. Liu, C.; Piquemal, J.-P.; Ren, P. Implementation of Geometry-Dependent Charge Flux into the Polarizable AMOEBA+ Potential. *J. Phys. Chem. Lett.* **2020,** *11*, 419-426.

107. Lambros, E.; Paesani, F. How good are polarizable and flexible models for water: Insights from a many-body perspective. *J. Chem. Phys.* **2020,** *153*, 060901.

108. Li, Z.; Li, C.; Wang, Z.; Voth, G. A. What Coordinate Best Describes the Affinity of the Hydrated Excess Proton for the Air–Water Interface? *J. Phys. Chem. B.* **2020,** *124*, 5039-5046.

109. Baer, M. D.; Fulton, J. L.; Balasubramanian, M.; Schenter, G. K.; Mundy, C. J. Persistent Ion Pairing in Aqueous Hydrochloric Acid. *J. Phys. Chem. B.* **2014,** *118*, 7211-7220.

110. Chandler, D. Ch. 7: Classical Fluids. In *Introduction to Modern Statistical Mechanics.* ; Oxford University Press: New York, 1987.

111. Hamrock, S. J.; Yandrasits, M. A. Proton Exchange Membranes for Fuel Cell Applications. *Journal of Macromolecular Science, Part C.* **2006,** *46*, 219-244.

112. Jang, S. S.; Molinero, V.; Çağın, T.; Goddard, W. A. Nanophase-Segregation and Transport in Nafion 117 from Molecular Dynamics Simulations: Effect of Monomeric Sequence. *J. Phys. Chem. B.* **2004,** *108*, 3149-3157.

113. Venkatnathan, A.; Devanathan, R.; Dupuis, M. Atomistic Simulations of Hydrated Nafion and Temperature Effects on Hydronium Ion Mobility. *J. Phys. Chem. B.* **2007,** *111*, 7234-7244.

114. Park, C. H.; Lee, C. H.; Sohn, J.-Y.; Park, H. B.; Guiver, M. D.; Lee, Y. M. Phase Separation and Water Channel Formation in Sulfonated Block Copolyimide. *J. Phys. Chem. B.* **2010,** *114*, 12036-12045.

115. Devanathan, R.; Dupuis, M. Insight from molecular modelling: does the polymer side chain length matter for transport properties of perfluorosulfonic acid membranes? *Physical Chemistry Chemical Physics.* **2012,** *14*, 11281-11295.

116. Choe, Y.-K.; Tsuchida, E.; Ikeshoji, T.; Yamakawa, S.; Hyodo, S.-a. Nature of Water Transport and Electro-Osmosis in Nafion: Insights from First-Principles Molecular Dynamics Simulations under an Electric Field. *J. Phys. Chem. B.* **2008,** *112*, 11586-11594.

117. Choe, Y.-K.; Tsuchida, E.; Ikeshoji, T.; Yamakawa, S.; Hyodo, S.-a. Nature of proton dynamics in a polymer electrolyte membrane, nafion: a first-principles molecular dynamics study. *Physical Chemistry Chemical Physics.* **2009,** *11*, 3892-3899.

118. Idupulapati, N.; Devanathan, R.; Dupuis, M. Ab Initio Study of Hydration and Proton Dissociation in Ionomer Membranes. *J. Phys. Chem. A.* **2010,** *114*, 6904-6912.

119. Devanathan, R.; Idupulapati, N.; Baer, M. D.; Mundy, C. J.; Dupuis, M. Ab Initio Molecular Dynamics Simulation of Proton Hopping in a Model Polymer Membrane. *J. Phys. Chem. B.* **2013,** *117*, 16522-16529.

120. Petersen, M. K.; Wang, F.; Blake, N. P.; Metiu, H.; Voth, G. A. Excess Proton Solvation and Delocalization in a Hydrophilic Pocket of the Proton Conducting Polymer Membrane Nafion. *J. Phys. Chem. B.* **2005,** *109*, 3727-3730.

121. Petersen, M. K.; Voth, G. A. Characterization of the Solvation and Transport of the Hydrated Proton in the Perfluorosulfonic Acid Membrane Nafion. *J. Phys. Chem. B.* **2006,** *110*, 18594-18600.

122. Feng, S.; Voth, G. A. Proton Solvation and Transport in Hydrated Nafion. *J. Phys. Chem. B.* **2011,** *115*, 5903-5912.

123. Feng, S.; Savage, J.; Voth, G. A. Effects of Polymer Morphology on Proton Solvation and Transport in Proton-Exchange Membranes. *J. Phys. Chem. C.* **2012,** *116*, 19104-19116.

124. Tse, Y.-L. S.; Herring, A. M.; Kim, K.; Voth, G. A. Molecular Dynamics Simulations of Proton Transport in 3M and Nafion Perfluorosulfonic Acid Membranes. *J. Phys. Chem. C.* **2013,** *117*, 8079-8091.

125. Savage, J.; Voth, G. A. Persistent Subdiffusive Proton Transport in Perfluorosulfonic Acid Membranes. *J. Phys. Chem. Lett.* **2014,** *5*, 3037-3042.

126. Savage, J.; Voth, G. A. Proton Solvation and Transport in Realistic Proton Exchange Membrane Morphologies. *J. Phys. Chem. C.* **2016,** *120*, 3176-3186.

127. Karo, J.; Aabloo, A.; Thomas, J. O.; Brandell, D. Molecular Dynamics Modeling of Proton Transport in Nafion and Hyflon Nanostructures. *J. Phys. Chem. B.* **2010,** *114*, 6056-6064.

128. Liu, S.; Savage, J.; Voth, G. A. Mesoscale Study of Proton Transport in Proton Exchange Membranes: Role of Morphology. *J. Phys. Chem. C.* **2015,** *119*, 1753-1762.

129. Petersen, M. K.; Kumar, R.; White, H. S.; Voth, G. A. A Computationally Efficient Treatment of Polarizable Electrochemical Cells Held at a Constant Potential. *J. Phys. Chem. C.* **2012,** *116*, 4903-4912.

130. Cao, Z.; Kumar, R.; Peng, Y.; Voth, G. A. Proton Transport under External Applied Voltage. *J. Phys. Chem. B.* **2014,** *118*, 8090-8098.

131. Cao, Z.; Peng, Y.; Voth, G. A. Ion Transport through Ultrathin Electrolyte under Applied Voltages. *J. Phys. Chem. B.* **2015,** *119*, 7516-7521.

132. Zawodzinski, T. A.; Davey, J.; Valerio, J.; Gottesfeld, S. The water content dependence of electro-osmotic drag in proton-conducting polymer electrolytes. *Electrochim. Acta.* **1995,** *40*, 297-302.

133. Din, X.-D.; Michaelides, E. E. Transport processes of water and protons through micropores. *AlChE J.* **1998,** *44*, 35-47.

134. Lin, H.-L.; Yu, T. L.; Han, F.-H. A Method for Improving Ionic Conductivity of Nafion Membranes and its Application to PEMFC. *Journal of Polymer Research.* **2006,** *13*, 379-385.

135. Allahyarov, E.; Taylor, P. L. Predicted electric-field-induced hexatic structure in an ionomer membrane. *Physical Review E.* **2009,** *80*, 020801.

136. Allahyarov, E.; Taylor, P. L.; Löwen, H. Simulation study of field-induced morphological changes in a proton-conducting ionomer. *Physical Review E.* **2010,** *81*, 031805.

137. Knox, C. K.; Voth, G. A. Probing Selected Morphological Models of Hydrated Nafion Using Large-Scale Molecular Dynamics Simulations. *J. Phys. Chem. B.* **2010,** *114*, 3205-3218.

138. Mayo, S. L.; Olafson, B. D.; Goddard, W. A. DREIDING: a generic force field for molecular simulations. *J. Phys. Chem.* **1990,** *94*, 8897-8909.

139. Murad, S. The role of external electric fields in enhancing ion mobility, drift velocity, and drift–diffusion rates in aqueous electrolyte solutions. *J. Chem. Phys.* **2011,** *134*, 114504.

140. Siroma, Z.; Ioroi, T.; Fujiwara, N.; Yasuda, K. Proton conductivity along interface in thin cast film of Nafion®. *Electrochem. Commun.* **2002,** *4*, 143-145.

141. Siroma, Z.; Kakitsubo, R.; Fujiwara, N.; Ioroi, T.; Yamazaki, S.-i.; Yasuda, K. Depression of proton conductivity in recast Nafion® film measured on flat substrate. *J. Power Sources.* **2009,** *189*, 994-998.

142. Eastman, S. A.; Kim, S.; Page, K. A.; Rowe, B. W.; Kang, S.; Soles, C. L.; Yager, K. G. Effect of Confinement on Structure, Water Solubility, and Water Transport in Nafion Thin Films. *Macromolecules.* **2012,** *45*, 7920-7930.

143. Weber, A. Z.; Kusoglu, A. Unexplained transport resistances for low-loaded fuel-cell catalyst layers. *Journal of Materials Chemistry A.* **2014,** *2*, 17207-17211.

144. Gaiduk, A. P.; Gustafson, J.; Gygi, F.; Galli, G. First-Principles Simulations of Liquid Water Using a Dielectric-Dependent Hybrid Functional. *J. Phys. Chem. Lett.* **2018,** *9*, 3068-3073.

145. Gaiduk, A. P.; Zhang, C.; Gygi, F.; Galli, G. Structural and electronic properties of aqueous NaCl solutions from ab initio molecular dynamics simulations with hybrid density functionals. *Chem. Phys. Lett.* **2014,** *604*, 89-96.

146. Gaiduk, A. P.; Galli, G. Local and Global Effects of Dissolved Sodium Chloride on the Structure of Water. *J. Phys. Chem. Lett.* **2017,** *8*, 1496-1502.

147. Schwegler, E.; Grossman, J. C.; Gygi, F.; Galli, G. Towards an assessment of the accuracy of density functional theory for first principles simulations of water. II. *J. Chem. Phys.* **2004,** *121*, 5400-5409.

148. Gaiduk, A. P.; Gygi, F.; Galli, G. Density and Compressibility of Liquid Water and Ice from First-Principles Simulations with Hybrid Functionals. *J. Phys. Chem. Lett.* **2015,** *6*, 2902-2908.

149. Morrone, J. A.; Car, R. Nuclear Quantum Effects in Water. *Phys. Rev. Lett.* **2008,** *101*, 017801.

150. Cesari, A.; Gil-Ley, A.; Bussi, G. Combining Simulations and Solution Experiments as a Paradigm for RNA Force Field Refinement. *J. Chem. Theory Comput.* **2016,** *12*, 6192-6200.

151. Cesari, A.; Reißer, S.; Bussi, G. Using the Maximum Entropy Principle to Combine Simulations and Solution Experiments. *Computation.* **2018,** *6*, 5.

152. Amirkulova, D. B.; White, A. D. Recent advances in maximum entropy biasing techniques for molecular dynamics. *Molecular Simulation.* **2019,** *45*, 1285-1294.

153. Babin, V.; Leforestier, C.; Paesani, F. Development of a "First Principles" Water Potential with Flexible Monomers: Dimer Potential Energy Surface, VRT Spectrum, and Second Virial Coefficient. *J. Chem. Theory Comput.* **2013,** *9*, 5395-5403.

154. Babin, V.; Medders, G. R.; Paesani, F. Development of a "First Principles" Water Potential with Flexible Monomers. II: Trimer Potential Energy Surface, Third Virial Coefficient, and Small Clusters. *J. Chem. Theory Comput.* **2014,** *10*, 1599-1607.

155. Medders, G. R.; Babin, V.; Paesani, F. Development of a "First-Principles" Water Potential with Flexible Monomers. III. Liquid Phase Properties. *J. Chem. Theory Comput.* **2014,** *10*, 2906-2910.

156. Reddy, S. K.; Straight, S. C.; Bajaj, P.; Huy Pham, C.; Riera, M.; Moberg, D. R.; Morales, M. A.; Knight, C.; Götz, A. W.; Paesani, F. On the accuracy of the MB-pol many-body potential for water: Interaction energies, vibrational frequencies, and classical thermodynamic and dynamical properties from clusters to liquid water and ice. *J. Chem. Phys.* **2016,** *145*, 194504.

157. Bonomi, M.; Bussi, G.; Camilloni, C.; Tribello, G. A.; Banáš, P.; Barducci, A.; Bernetti, M.; Bolhuis, P. G.; Bottaro, S.; Branduardi, D.; Capelli, R.; Carloni, P.; Ceriotti, M.; Cesari, A.; Chen, H.; Chen, W.; Colizzi, F.; De, S.; De La Pierre, M.; Donadio, D.; Drobot, V.; Ensing, B.; Ferguson, A. L.; Filizola, M.; Fraser, J. S.; Fu, H.; Gasparotto, P.; Gervasio, F. L.; Giberti, F.; Gil-Ley, A.; Giorgino, T.; Heller, G. T.; Hocky, G. M.; Iannuzzi, M.; Invernizzi, M.; Jelfs, K. E.; Jussupow, A.; Kirilin, E.; Laio, A.; Limongelli, V.; Lindorff-Larsen, K.; Löhr, T.; Marinelli, F.; Martin-Samos, L.; Masetti, M.; Meyer, R.; Michaelides, A.; Molteni, C.; Morishita, T.; Nava, M.; Paissoni, C.; Papaleo, E.; Parrinello, M.; Pfaendtner, J.; Piaggi, P.; Piccini, G.; Pietropaolo, A.; Pietrucci, F.; Pipolo, S.; Provasi, D.; Quigley, D.; Raiteri, P.; Raniolo, S.; Rydzewski, J.; Salvalaglio, M.; Sosso, G. C.; Spiwok, V.; Šponer, J.; Swenson, D. W. H.; Tiwary, P.; Valsson, O.; Vendruscolo, M.; Voth, G. A.; White, A.; The, P. c. Promoting transparency and reproducibility in enhanced molecular simulations. *Nat. Methods.* **2019,** *16*, 670-673.

158. Soper, A. K.; Benmore, C. J. Quantum Differences between Heavy and Light Water. *Phys. Rev. Lett.* **2008,** *101*, 065502.

159. Errington, J. R.; Debenedetti, P. G. Relationship between structural order and the anomalies of liquid water. *Nature.* **2001,** *409*, 318-321.

160. Krynicki, K.; Green, C. D.; Sawyer, D. W. Pressure and temperature dependence of self-diffusion in water. *Faraday Discussions of the Chemical Society.* **1978,** *66*, 199-208.

161. Yeh, I.-C.; Hummer, G. System-Size Dependence of Diffusion Coefficients and Viscosities from Molecular Dynamics Simulations with Periodic Boundary Conditions. *J. Phys. Chem. B.* **2004,** *108*, 15873-15879.

162. Holmes, M. J.; Parker, N. G.; Povey, M. J. W. Temperature dependence of bulk viscosity in water using acoustic spectroscopy. *J. Phys.: Conf. Ser.* **2011,** *269*, 012011.

163. Schmidt, J.; VandeVondele, J.; Kuo, I. F. W.; Sebastiani, D.; Siepmann, J. I.; Hutter, J.; Mundy, C. J. Isobaric−Isothermal Molecular Dynamics Simulations Utilizing Density Functional Theory: An Assessment of the Structure and Density of Water at Near-Ambient Conditions. *J. Phys. Chem. B.* **2009,** *113*, 11959-11964.

164. Ma, Z.; Zhang, Y.; Tuckerman, M. E. Ab initio molecular dynamics study of water at constant pressure using converged basis sets and empirical dispersion corrections. *J. Chem. Phys.* **2012,** *137*, 044506.

165. Jungwirth, P.; Tobias, D. J. Specific Ion Effects at the Air/Water Interface. *Chem. Rev.* **2006,** *106*, 1259-1281.

166. Baer, M. D.; Kuo, I. F. W.; Tobias, D. J.; Mundy, C. J. Toward a Unified Picture of the Water Self-Ions at the Air–Water Interface: A Density Functional Theory Perspective. *J. Phys. Chem. B.* **2014,** *118*, 8364-8372.

167. Wagner, J. W.; Dannenhoffer-Lafage, T.; Jin, J.; Voth, G. A. Extending the range and physical accuracy of coarse-grained models: Order parameter dependent interactions. *J. Chem. Phys.* **2017,** *147*, 044113.

168. Cukierman, S. Et tu, Grotthuss! and other unfinished stories. *Biochim. Biophys. Acta.* **2006,** *1757*, 876-885.

169. Wraight, C. A. Chance and design--proton transfer in water, channels and bioenergetic proteins. *Biochim. Biophys. Acta.* **2006,** *1757*, 886-912.

170. Decoursey, T. E. Voltage-gated proton channels and other proton transfer pathways. *Physiol. Rev.* **2003,** *83*, 475-579.

171. Jorn, R.; Savage, J.; Voth, G. A. Proton Conduction in Exchange Membranes across Multiple Length Scales. *Acc. Chem. Res.* **2012,** *45*, 2002-2010.

172. von Grotthuss, C. J. T. *Sur la décomposition de l'eau et des corps qu'elle tient en dissolution à l'aide de l'électricité galvanique*; Ann. Chim. , 1806.

173. Agmon, N. The Grotthuss mechanism. *Chem. Phys. Lett.* **1995,** *244*, 456-462.

174. Tuckerman, M. E.; Marx, D.; Parrinello, M. The nature and transport mechanism of hydrated hydroxide ions in aqueous solution. *Nature.* **2002,** *417*, 925.

175. Voth, G. A. Computer Simulation of Proton Solvation and Transport in Aqueous and Biomolecular Systems. *Acc. Chem. Res.* **2006,** *39*, 143-150.

176. Eigen, M. Proton Transfer, Acid-Base Catalysis, and Enzymatic Hydrolysis. Part I: ELEMENTARY PROCESSES. *Angew. Chem., Int. Ed. Engl.* **1964,** *3*, 1-19.

177. Berkelbach, T. C.; Lee, H.-S.; Tuckerman, M. E. Concerted Hydrogen-Bond Dynamics in the Transport Mechanism of the Hydrated Proton: A First-Principles Molecular Dynamics Study. *Phys. Rev. Lett.* **2009,** *103*, 238302.

178. Zahn, D.; Brickmann, J. Quantum–Classical Simulation of Proton Migration in Water. *Isr. J. Chem.* **1999,** *39*, 469-482.

179. Chen, C.; Arntsen, C.; Voth, G. A. Development of reactive force fields using ab initio molecular dynamics simulation minimally biased to experimental data. *Journal of Chemical Physics.* **2017,** *147*, 161719.

180. Calio, P. B.; Hocky, G. M.; Voth, G. A. Minimal Experimental Bias on the Hydrogen Bond Greatly Improves Ab Initio Molecular Dynamics Simulations of Water. *J. Chem. Theory Comput.* **2020**.

181. Li, C.; Swanson, J. M. J. Understanding and Tracking the Excess Proton in Ab Initio Simulations; Insights from IR Spectra. *J. Phys. Chem. B.* **2020**.

182. Becke, A. D. Density-functional exchange-energy approximation with correct asymptotic behavior. *Phys. Rev. A Gen. Phys.* **1988,** *38*, 3098-3100.

183. Lee, C.; Yang, W.; Parr, R. G. Development of the Colle-Salvetti correlation-energy formula into a functional of the electron density. *Phys. Rev. B.* **1988,** *37*, 785-789.

184. Grimme, S. Accurate description of van der Waals complexes by density functional theory including empirical corrections. *J. Comput. Chem.* **2004,** *25*, 1463-73.

185. Grimme, S.; Antony, J.; Ehrlich, S.; Krieg, H. A consistent and accurate ab initio parametrization of density functional dispersion correction (DFT-D) for the 94 elements H-Pu. *J. Chem. Phys.* **2010,** *132*, 154104.

186. Cisneros, G. A.; Wikfeldt, K. T.; Ojamae, L.; Lu, J.; Xu, Y.; Torabifard, H.; Bartok, A. P.; Csanyi, G.; Molinero, V.; Paesani, F. Modeling Molecular Interactions in Water: From Pairwise to Many-Body Potential Energy Functions. *Chem. Rev.* **2016,** *116*, 7501-28.

187. Gillan, M. J.; Alfe, D.; Michaelides, A. Perspective: How good is DFT for water? *J. Chem. Phys.* **2016,** *144*, 130901.

188. Tse, Y. L.; Knight, C.; Voth, G. A. An analysis of hydrated proton diffusion in ab initio molecular dynamics. *J. Chem. Phys.* **2015,** *142*, 014104.

189. Knight, C.; Lindberg, G. E.; Voth, G. A. Multiscale reactive molecular dynamics. *J. Chem. Phys.* **2012,** *137*, 22A525.

190. Arntsen, C.; Chen, C.; Voth, G. A. Reactive molecular dynamics models from ab initio molecular dynamics data using relative entropy minimization. *Chem. Phys. Lett.* **2017,** *683*, 573-578.